

INFORMATION TO USERS

This dissertation was produced from a microfilm copy of the original document. While the most advanced technological means to photograph and reproduce this document have been used, the quality is heavily dependent upon the quality of the original submitted.

The following explanation of techniques is provided to help you understand markings or patterns which may appear on this reproduction.

1. The sign or "target" for pages apparently lacking from the document photographed is "Missing Page(s)". If it was possible to obtain the missing page(s) or section, they are spliced into the film along with adjacent pages. This may have necessitated cutting thru an image and duplicating adjacent pages to insure you complete continuity.
2. When an image on the film is obliterated with a large round black mark, it is an indication that the photographer suspected that the copy may have moved during exposure and thus cause a blurred image. You will find a good image of the page in the adjacent frame.
3. When a map, drawing or chart, etc., was part of the material being photographed the photographer followed a definite method in "sectioning" the material. It is customary to begin photoing at the upper left hand corner of a large sheet and to continue photoing from left to right in equal sections with a small overlap. If necessary, sectioning is continued again — beginning below the first row and continuing on until complete.
4. The majority of users indicate that the textual content is of greatest value, however, a somewhat higher quality reproduction could be made from "photographs" if essential to the understanding of the dissertation. Silver prints of "photographs" may be ordered at additional charge by writing the Order Department, giving the catalog number, title, author and specific pages you wish reproduced.

University Microfilms

300 North Zeeb Road
Ann Arbor, Michigan 48106
A Xerox Education Company

72-24,436

RICH, William Guy, 1939-
LOW ENERGY STUDIES OF THE EXPERIMENTAL ELASTIC
DIFFERENTIAL CROSS SECTIONS FOR THE SYSTEMS
 $H^+ + He$, $H^+ + Ne$, AND $He^+ + He$.

The College of William and Mary in Virginia,
Ph.D., 1972
Physics, molecular

University Microfilms, A XEROX Company, Ann Arbor, Michigan

LOW ENERGY STUDIES OF THE EXPERIMENTAL ELASTIC
DIFFERENTIAL CROSS SECTIONS FOR THE SYSTEMS
 $H^+ + He$, $H^+ + Ne$, and $He^+ + He$

A Dissertation

Presented to

The Faculty of the Department of Physics
The College of William and Mary in Virginia

In Partial Fulfillment
of the Requirements for the Degree of
Doctor of Philosophy

by

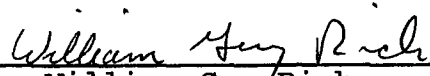
William Guy Rich

1972

APPROVAL SHEET

This dissertation is submitted in partial fulfillment of
the requirements for the degree of

Doctor of Philosophy




William Guy/Rich

Approved, May 1972



Lynn D. Doverspike




Roy L. Champion



Frederic R. Crownfield, Jr.



Richard L. Kiefer



Edward A. Remler

PLEASE NOTE:

Some pages may have
indistinct print.

Filmed as received.

University Microfilms, A Xerox Education Company

TABLE OF CONTENTS

	Page
ACKNOWLEDGEMENTS.	v
LIST OF TABLES.	vii
LIST OF FIGURES	viii
ABSTRACT.	xii
Chapter	
I. INTRODUCTION	2
II. APPARATUS AND EXPERIMENTAL METHOD.	11
Description of Apparatus	11
Experimental Method.	23
Calibrations	24
Experimental Procedure	28
III. HETERONUCLEAR SYSTEMS.	30
Theoretical Considerations	30
Application.	46
Conclusion	67
IV. HOMONUCLEAR SYSTEMS.	70
Discussion	70
Theoretical Considerations	75
Application.	89
Conclusion	109

	Page
APPENDIX.	120
REFERENCES.	128

ACKNOWLEDGEMENTS

The author wishes to express his gratitude for the guidance, assistance, and timely advice of his advisors, Drs. L. D. Doverspike and R. L. Champion. Their continuing interest has made this work enjoyable and rewarding. He wishes to thank Dr. E. A. Remler for the many discussions on the analysis of the data and for the basic computer program used for same. Dr. F. R. Crownfield is thanked for his continuing interest throughout the course of this work. His suggestions and comments have been very helpful on both the experimental and theoretical aspects of this dissertation. Appreciation is extended to the above as well as to Dr. Richard Kiefer and Dr. J. B. Delos for their comments and suggestions on the final draft of this thesis.

Special thanks are due Mr. S. G. Hummel for his help in design and construction of the research apparatus. Mr. H. C. Seyffer's help and many suggestions on the electronic aspect of the apparatus are greatly appreciated.

Appreciation and gratitude are extended to Dr. S. M. Bobbio for the many hours spent working on the acquisition and analysis of the data. Without such able assistance, the task would have been much more difficult.

The author wishes to thank his wife, Linda, for her support, understanding, and encouragement throughout the many years of this work.

LIST OF TABLES

Table	Page
I. Heteronuclear Parameters.	69
II. Homonuclear Parameters.	118
III. Absolute Differential Cross Section Calculations.	119

LIST OF FIGURES

Figure	Page
1. Apparatus	12
2. Duoplasmatron source	14
3. Collision can	17
4. Steps of a potential-model calculation of the differential elastic cross section. (a) Assumed intermolecular potential. (B) Classical deflection function. (C) Phase shifts. (D) Partial wave calculation of differential cross section.	33
5. Remler parameterization of phase shift. (A) Phase shift η_p and deflection function Θ_p for a single pole located at λ_p . (B) Core phase shift η_C , pole phase shift η_A , and the total phase shift η for a typical attractive scattering system.	40
6. Elastic differential cross section of $H^+ + He$, $E = 4$ eV. (A) Experiment. (B) Inverted potential calculation. (C) Potential-model calculation.	47
7. Intermolecular potentials retrieved from $H^+ + He$ experiment, $E = 4$ eV. (A) Inverted potential. (B) Potential-model potential.	52
8. Elastic differential cross section for $H^+ + He$, $E = 4$ eV. (A) Experiment. (B) Mittmann's potential-model calculation.	55
9. Comparison of intermolecular potentials for $H^+ + He$, $E = 4$ eV. (A) Inverted potential. (B) Mittmann's potential-model.	57

Figure	Page
10. Comparison of intermolecular potentials for $H^+ + He$, $E = 4$ eV. Solid line is the inverted potential retrieved from the experiment. The points are from the <u>ab initio</u> calculations of Wolniewicz.	59
11. Elastic differential cross section for $H^+ + Ne$, $E = 5.71$ eV. (A) Experiment. (B) Inverted potential calculation. (C) Potential-model calculation.	61
12. Intermolecular potentials retrieved from $H^+ + Ne$ experiment, $E = 5.71$ eV. (A) Inverted potential. (C) Potential-model potential. (B) Mittmann's potential-model. . .	63
13. Elastic differential cross section of $H^+ + Ne$, $E = 5.71$ eV. (A) Experiment. (B) Mittmann's potential-model calculation.	64
14. Intermolecular potentials for $H^+ + Ne$, $E = 5.71$ eV. Solid line is the inverted potential. The points are the <u>ab initio</u> calculations of Peyerimhoff.	66
15. Contributions to the elastic differential cross section of ${}^3He^+ + {}^3He$, $E = 6$ eV. (A) Direct scattered differential cross section $ f_g(\theta) ^2$. (B) Direct scattered differential cross section $ f_u(\theta) ^2$	79
16. Elastic differential cross section of ${}^3He^+ + {}^3He$, $E = 6$ eV, with charge-exchange being neglected. The two-state direct scattered interference $ f_g(\theta) + f_u(\theta) ^2$ in the differential cross section is dominant in the post rainbow region.	81

Figure	Page
17. Contributions to the elastic differential cross section of ${}^3\text{He}^+ + {}^3\text{He}$, $E = 6$ eV with charge-exchange being considered. (A) Contributions from the gerade potential $ f_g(\theta) + f_g(\pi - \theta) ^2$. (B) Contribution from the ungerade potential $ f_u(\theta) + f_u(\pi - \theta) ^2$. Solid line is a convolution of the high frequency oscillations in both A and B.	84
18. Classical deflection function for ${}^3\text{He}^+ + {}^3\text{He}$, $E = 6$ eV. (A) Ungerade charge-exchange scattering. (B) Gerade charge-exchange scattering. (C) Gerade direct scattering. (D) Ungerade direct scattering.	86
19. Complete elastic differential cross section for ${}^3\text{He}^+ + {}^3\text{He}$, $E = 6$ eV. Different contributions to the differential cross section can be identified by comparison with Figures 15, 16, and 17.	87
20. Elastic differential cross section for ${}^3\text{He}^+ + {}^3\text{He}$, $E = 6$ eV. (A) Remler-Regge calculated differential cross section. (B) Experiment.	90
21. Elastic differential cross section for ${}^3\text{He}^+ + {}^3\text{He}$, $E = 6$ eV. (A) Potential-model calculation. (B) Experiment.	96
22. Intermolecular potentials retrieved from the experiment for ${}^3\text{He}^+ + {}^3\text{He}$, $E = 6$ eV. (A) Inverted potential. (B) Potential-model potential. (C) Analytic fit (potential-model type) to the inverted potential.	97
23. Elastic differential cross section for ${}^3\text{He}^+ + {}^3\text{He}$, $E = 6$ eV. (A) Second potential calculation using an analytic fit to the inverted potential. (B) Experiment.	98

Figure	Page
24. Elastic differential cross section for $^4\text{He}^+ + ^4\text{He}$, $E = 6$ eV. (A) Inverted calculation of the differential cross section. (B) Experiment.	100
25. Inverted intermolecular potential retrieved from the data for $^4\text{He}^+ + ^4\text{He}$, $E = 6$ eV.	101
26. Experimental elastic differential cross sections for (A) $^3\text{He}^+ + ^4\text{He}$ and (B) $^4\text{He}^+ + ^3\text{He}$, $E = 6$ eV.	103
27. Elastic differential cross section for $^3\text{He}^+ + ^4\text{He}$, $E = 6$ eV. (A) Inverted calculation of the differential cross section. (B) Experiment.	106
28. Inverted intermolecular potential for $^3\text{He}^+ + ^4\text{He}$ or $^4\text{He}^+ + ^3\text{He}$, $E = 6$ eV.	107
29. Comparison of the inverted intermolecular potentials for all the $\text{He}^+ + \text{He}$ systems, $E = 6$ eV. (A) $^4\text{He}^+ + ^4\text{He}$. (B) $^3\text{He}^+ + ^4\text{He}$ or $^4\text{He}^+ + ^3\text{He}$. (C) $^3\text{He}^+ + ^3\text{He}$	112
30. Classical deflection function. Illustration of the flexibility in the repulsive branch of the classical deflection function.	127

ABSTRACT

The experimental elastic differential cross sections for low center-of-mass collision energies for ion-atom scattering are reported for heteronuclear systems ($H^+ + He$, $E = 4$ eV; $H^+ + Ne$, $E = 5.71$ eV) and for homonuclear systems ($^3He^+ + ^3He$, $^4He^+ + ^4He$, $^3He^+ + ^4He$, $^4He^+ + ^3He$, $E = 6$ eV). The experiments are performed at energies low enough to prevent inelastic scattering, but high enough to avoid classical orbiting. The intermolecular potentials retrieved from these experiments are reported and are compared with the results of existing ab initio calculations.

Two approaches are utilized in the analysis of the experimental data: (1) A parameterized analytic (Morse) potential is used in the calculation of the JWKB phase shifts, which are then used in the Rayleigh-Faxen-Holtzmark partial wave sum to determine the scattering amplitude and thereby the differential cross section. By an iterative variation of the potential parameters, the calculation is brought into agreement with the experiment. (2) Using the convenient S-matrix (diagonal) parameterization of the scattering amplitude in the complex l -plane, which has been developed by E. A. Remler, the differential cross section is calculated and is iteratively compared to the experiment by varying the S-matrix parameters. A result of this calculation is an analytic expression for the phase shifts which can be used in a formal inversion calculation of the intermolecular potential.

One-state intermolecular potentials are sufficient to calculate the differential cross section for the heteronuclear systems, but two-state intermolecular potentials (gerade and ungerade) are necessary for the homonuclear calculations. The gerade potential is held constant (i.e. is assumed to be known from ab initio calculations) and only the ungerade potential is varied in the analysis of the homonuclear systems.

The experimental method used in this work to obtain high resolution data from which the intermolecular potentials are retrieved is the best method presently available for the determination of such potentials.

William Guy Rich

Department of Physics

The College of William and Mary in Virginia

LOW ENERGY STUDIES OF THE EXPERIMENTAL ELASTIC
DIFFERENTIAL CROSS SECTIONS FOR THE SYSTEMS
 $H^+ + He$, $H^+ + Ne$, and $He^+ + He$

CHAPTER I
INTRODUCTION

In the late 1920's and early 1930's the theoretical ground work for atom-atom and ion-atom elastic differential scattering was laid. This work was an outgrowth of the efforts of the early quantum theorists. However, it was not until the mid 1950's that experimental techniques were developed to a point to where it was possible to start applying the theories to specific laboratory experiments. By this time the neutral atom-atom work of Amdur¹ began to appear in the literature, and in 1959 the classic paper of Ford and Wheeler² on semiclassical scattering was published. The following year Land and Everhart³ reported their work on ion-atom scattering. Thus began a decade of intensive experimental and theoretical work in the scattering of neutrals and ions by atoms and molecules.

The experiments in the late 1950's and early 1960's were primarily in the several KeV energy range. At energies of this magnitude it was not too difficult to obtain reasonably monoenergetic, collimated beams. The KeV energy range was something of a mixed blessing. It

was high enough to use the Born approximation and small-angle approximations in the scattering analysis. On the other hand, the experimental results were very sensitive to apparatus geometry and beam width.

In 1966 Bernstein⁴ wrote an excellent review of elastic molecular scattering in which he expanded upon the small-angle approximations as well as the semiclassical approximations of Ford and Wheeler. The semiclassical approach to the scattering problem gave tremendous insight into the physics of elastic differential scattering through the use of the classical deflection function. By this time several laboratories were reporting experiments on atom-atom and ion-atom differential elastic scattering. Of these laboratories some began concentrating on ion-molecular experiments at energies below the KeV range.

The low-energy ion beams, though much more difficult to obtain, yield scattering data with several desirable characteristics. These are as follows: (a) Meaningful measurements can be made at scattering angles well outside the region to which the primary ion beam is confined. (b) Measurements made at relatively large angles are not as sensitive to apparatus geometry as are measurements taken at very small angles. (c) It may

be possible to resolve fine structure in the data which may be unresolvable at higher collision energies. (d) Inelastic scattering channels can be excluded by keeping the collision energy below a certain threshold. (e) By restricting the experiments to elastic scattering only, the theoretical treatment is greatly simplified. The experiments at low collision energies have truly yielded a great deal of information about the intermolecular potentials between the reactants and have greatly intensified the interest in ion-atom and ion-molecule scattering.

The purpose of these studies is to report the measurement of the differential elastic scattering of low-energy protons and singly charged Helium by several rare gas atoms and to use this information to obtain the intermolecular potentials for the corresponding molecular-ion systems. This has been accomplished with reasonable success. The low-energy experiments reported here can be divided into two classes; (1) heteronuclear systems whose scattering is governed by a single ground-state potential (called one-state systems), and (2) homonuclear systems whose scattering is governed by two states (called two-state systems). The one-state and two-state systems will be discussed separately.

The one-state systems to be studied here are HeH^+ and NeH^+ . The energy range of the experiments is chosen so that orbiting is not possible in the low-energy limit and excitation is also prohibited. In this energy range the Born-Oppenheimer approximation is assumed to be applicable, and in both the experiments and analysis only elastic scattering is considered. The elastic differential cross sections resulting from such experiments have proved to be very rich in structure, and the features of this one-state scattering can be understood in terms of the semiclassical ideas discussed by Bernstein.⁴ That is, the low and high frequency oscillations seen in the data can be related in a straightforward way to simple features of the classical deflection function.

In order to extract the intermolecular potential from the experimental differential cross section, two different approaches are used. (1) Assume an analytic, parameterized form of the intermolecular potential⁵ (hereafter called potential-model). Employing this potential-model in the JWKB calculation for the phase shifts, the scattering amplitude is calculated via the Rayleigh-Faxen-Holtzmark (RFH) partial wave sum. The resulting differential cross section is then compared to

the experimental differential cross section. By varying the parameters of the potential-model, an iterative procedure is employed to obtain agreement between the calculated and experimental differential cross sections. This type potential-model calculation has been used extensively, but it is not completely satisfying because it is not a direct inversion of the data to obtain the intermolecular potential. In addition, the amount of computer time required for a potential-model calculation can be prohibitive. The number of phase shifts necessary to accurately calculate the scattering amplitude is proportional to the product of the wave number ($k = (2\mu E/h^2)^{1/2}$) and a finite radius D , where D is the effective radius at which the interaction between the reactants can be assumed to be zero (D being different for each system). For the systems reported here, up to one thousand phase shifts are necessary to calculate the scattering amplitude in this "semiquantal" fashion. (2) Another method is an inversion technique in which the intermolecular potential is the end product of the calculation.⁶ This is a new method of analyzing the elastic differential cross section which has been developed by E.A. Remler.⁷ In this procedure the S -matrix representing the elastic scattering is parameterized in the complex angular momentum plane. The scattering amplitude

is then calculated using the RFH sum, which has been converted to a sum over a finite number of poles, and the resulting differential cross section is calculated. By varying the parameterization of the S-matrix, the features seen in the calculated differential cross section can be varied. Thus an iterative procedure is employed to achieve agreement between the experimental data and the S-matrix calculation of the differential cross section. The Remler calculation has definite advantages over the potential-model calculations: (a) The calculation is more efficient since it is no longer necessary to calculate a large number of phase shifts in order to insure convergence of the scattering amplitude; (b) The phase shifts are calculated without recourse to any semiclassical approximation; (c) The intermolecular potential calculated via the Remler method is a more direct inversion of the data.

The phase shifts which are available from an S-matrix calculation are used in an inversion procedure²⁴ to obtain the intermolecular potential. Given such a set of phases (within the realm of the validity of the JWKB approximation), the integral equation for the phase shifts is formally inverted to obtain the corresponding intermolecular potential.

For each system to be discussed in Chapter III, the potential-model potential and the inverted potential will be compared with each other as well as with existing ab initio calculations for the intermolecular potential.

The elastic differential cross sections of the homonuclear systems to be reported here are the result of scattering from two states. These two states naturally follow from the symmetry involved in the $\text{He}^+ + \text{He}$ molecular system. That is, the complete symmetry of the potential upon inversion in the center of mass allows the electronic wave functions to fall into two orthogonal families, the gerade and the ungerade. Both states go asymptotically to the same energy at large internuclear separation. The observed $\text{He}^+ + \text{He}$ differential cross section is very interesting in that it contains interference oscillations from several sources: (a) All the high frequency and low frequency oscillations due to the attractive well of the ungerade state are present (as discussed in the one-state systems). (b) There is interference between the gerade and ungerade states themselves. (c) When both ion and target have identical nuclei, there is interference due to this nuclear symmetry. All of these interferences become dominant at different angular positions in the differential cross section.

Several authors have reported work on the $\text{He}^+ + \text{He}$ systems at higher collision energies than those reported here.^{8,9,10,11,12} These higher energies do not allow the clear resolution of the rainbow oscillations or any of the secondary rainbow structure. However, the low collision energy (6 eV) experiments reported here have resolved the rainbow as well as the post rainbow type oscillations and this information is used in the determination of the ungerade state of the $\text{He}^+ + \text{He}$ systems. In addition, the energy is low enough to avoid any interference due to curve crossing or pseudo-curve crossing, but not low enough to allow orbiting of the incident ion. The low-energy experiments reported here have resulted in the determination of a potential (ungerade) which yields much better agreement between calculated differential cross sections and experiments than do those potentials (ungerade) which have been reported previously.

Since the collision energy in the experiments is only 6 eV, it is assumed that the lowest gerade state and the lowest ungerade state (also the ground-state) are the only states which participate in the scattering. The gerade state which is used in the present calculations has previously been carefully calculated,^{10,11} and in the region of interest its value has not changed appreciably

in any calculation reported to date. On the other hand, the ungerade potentials of the different theoretical calculations* have noticeable variations in the values of r_m (position of the potential minimum) and ϵ (well depth). Therefore, the calculational procedure employed in analyzing the data is to assume the gerade state is known (i.e. it is not allowed to change in any computation), and to allow the ungerade state to be varied. If both the gerade and ungerade potentials were allowed to vary, the calculations would have been much more difficult, and the computer time required would have been prohibitive. Both the potential-model potential and inverted potential methods (as discussed for one-state systems) are used in arriving at the final ungerade potential. The ungerade potential reported here is believed to be the most accurate to date.

*References # 10, 11, & 31.

CHAPTER II

APPARATUS DESCRIPTION AND EXPERIMENTAL METHOD

Section I. Apparatus

The purpose of these studies is to measure the differential elastic scattering of low-energy protons and singly charged Helium ions by several rare gas atoms and to use this information to obtain the intermolecular potentials for the corresponding molecular-ion systems. A schematic diagram of the apparatus as used in these investigations is shown in Figure 1. The essential parts of the apparatus are: an ion gun, which produces a mass analyzed and well-collimated low-energy ion beam; a collision region containing scattering gas; and a product ion detection system. The complete detection system both mass and energy analyzes the scattered ions, and it can be rotated about the collision region through an angular range of $-5^\circ \leq \theta \leq 90^\circ$ with respect to the primary beam. The essential parts of the apparatus are described in the following discussion.

Ion Gun

The ion gun is made up of three basic sections: (1) a

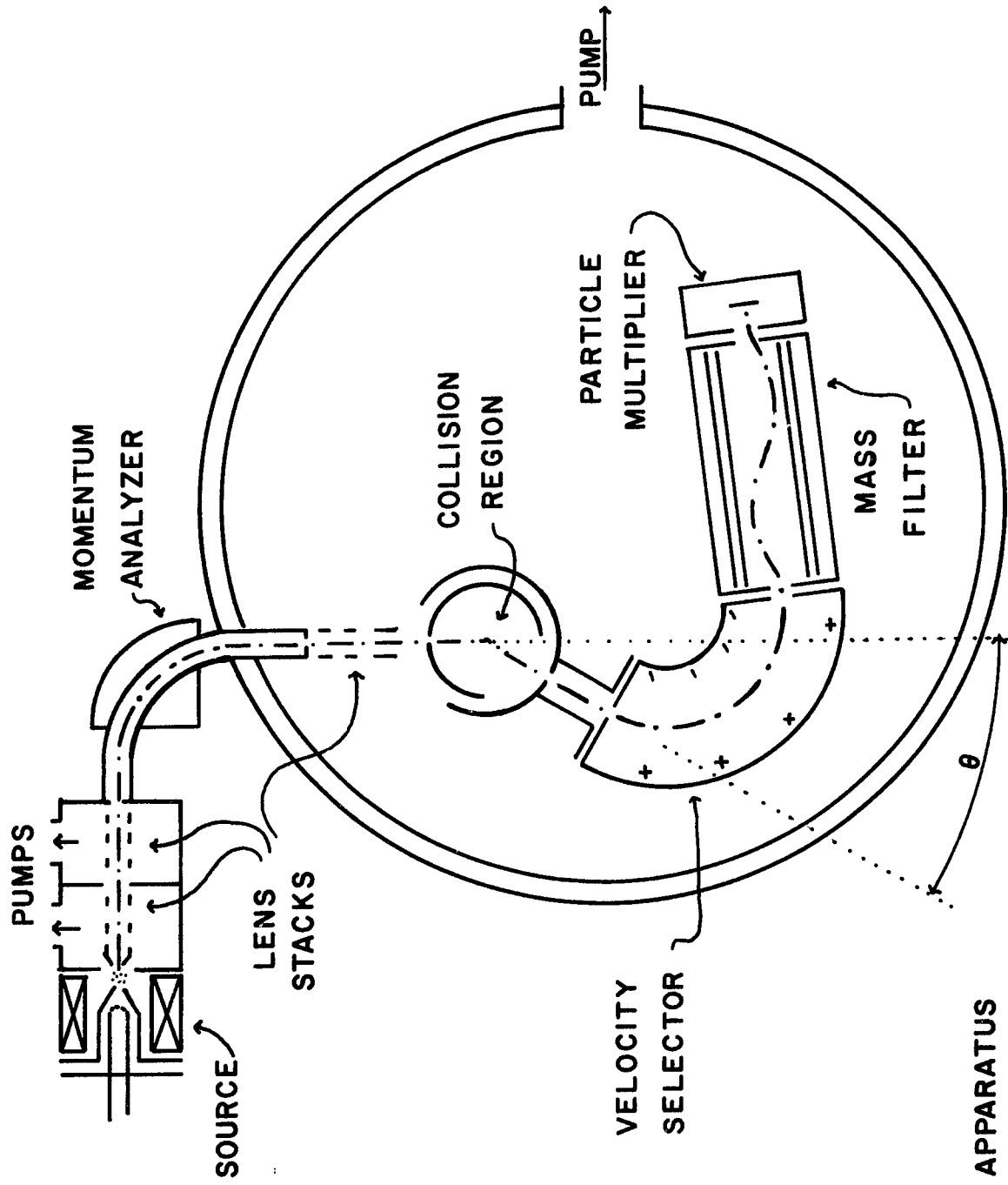


Figure 1. APPARATUS

duoplasmatron ion source in which the ions are formed, (2) a momentum analysis system, and (3) focusing elements which are placed before and after the momentum analyzer.

The source gas is admitted at a controlled rate into the duoplasmatron by a Vacronic VVB-50-Q leak valve. The duoplasmatron is a variation of the ion source described by Aberth and Peterson.¹³ Figure 2 shows a schematic diagram of a typical duoplasmatron. The method of operation is to feed the source gas into the source at a constant rate, to strike and maintain an arc between the filament and anode, and to draw out the desired ions through a small hole in the center of the anode. The purpose of the z-element shown in Figure 2 is to aid in striking the arc and to help confine the arc to a small volume. The source is differentially pumped through the 0.025 inch opening in the anode. The filament, magnet, and z-element can be moved as a unit, under vacuum, in the lateral direction with respect to the anode. This is desirable since there is always an optimum portion of the arc from which to extract certain ions. The magnetic field of the duoplasmatron, which is created by the electromagnet, is used to help contain the arc and to keep the ions and electrons moving parallel to the direction of the flow of the source gas.

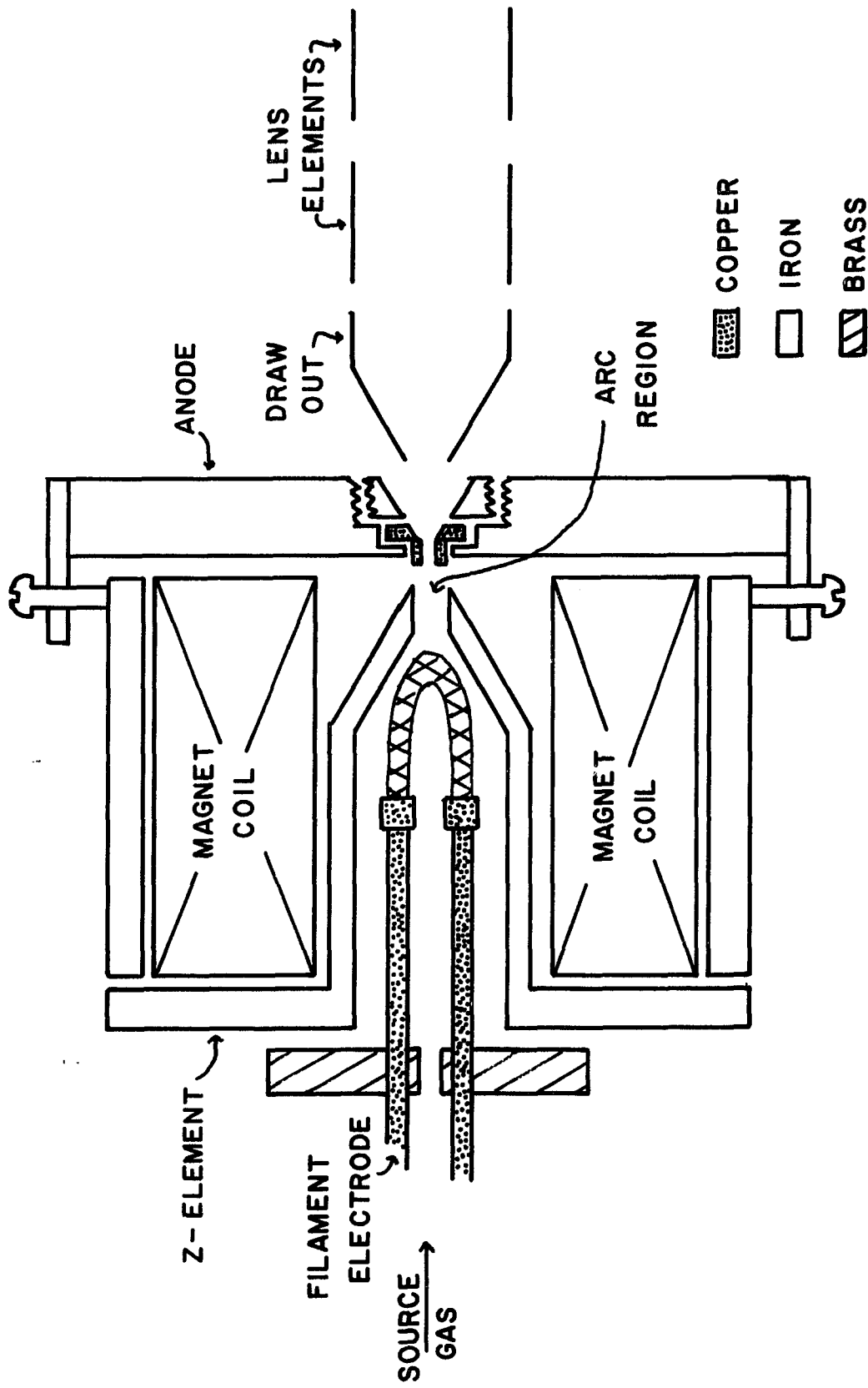


Figure 2. DUOPLASMATRON SOURCE

The duoplasmatron is water and air cooled and is electrically isolated from earth ground. This isolation allows the interaction between the ion and target atom to take place in the collision region at ground potential. By biasing the duoplasmatron and its supporting electronics with respect to earth ground, the ions which are produced can be accelerated through the biasing potential to ground with a predetermined energy. That is, by having the collision region at ground potential, the energy of a singly charged ion in the collision region is approximately the biasing potential applied to the duoplasmatron.

The ion drawout and electrostatic focusing elements are also biased in the same manner as the source. The electrostatic focusing curves of Spangenberg¹⁴ are used in the design of the electrostatic focusing lens systems. Three lens systems (two lens stacks before the momentum analyzer and one lens stack after) are used for focusing purposes at different points along the beam path. A typical lens stack consists of from three to seven cylindrical elements of different lengths. A combination of inside diameter, length, and voltage on an element determines its focusing properties. In two of the lens stacks, an element was split so that a small differential voltage could be placed on the two halves of the element

to provide lateral control of the primary beam.

After being extracted from the arc, the beam of ions is focused by two of the three focusing stacks through a .050 x .500 inch slit. The slit is the entrance of a 6-inch radius, 90° magnetic momentum analyzer which employs second-order focusing.¹⁵ The energy spread of the transmitted ion beam is approximately 1% of the energy of the beam through the analyzer. Typical energies through the momentum analyzer are in the 30 eV region. After momentum analysis the ion beam is collimated and decelerated by the third set of lenses and focused into the center of the collision chamber.

Collision Region

The collision chamber is made up of two concentric, close-fitting cylinders with the inner cylinder being stationary. The outer cylinder is rotatable about the inner cylinder. Each of the cylinders has a slot-slit arrangement such that together they form .050 x .250 inch entrance and exit slits. Figure 3A is a diagram illustrating the slot-slit arrangement. Inside the collision chamber are two electrically isolated deflection plates (see Fig. 3B) which allow an electric field to be applied across the collision region transverse to the path of the primary beam. The target atoms are admitted through the

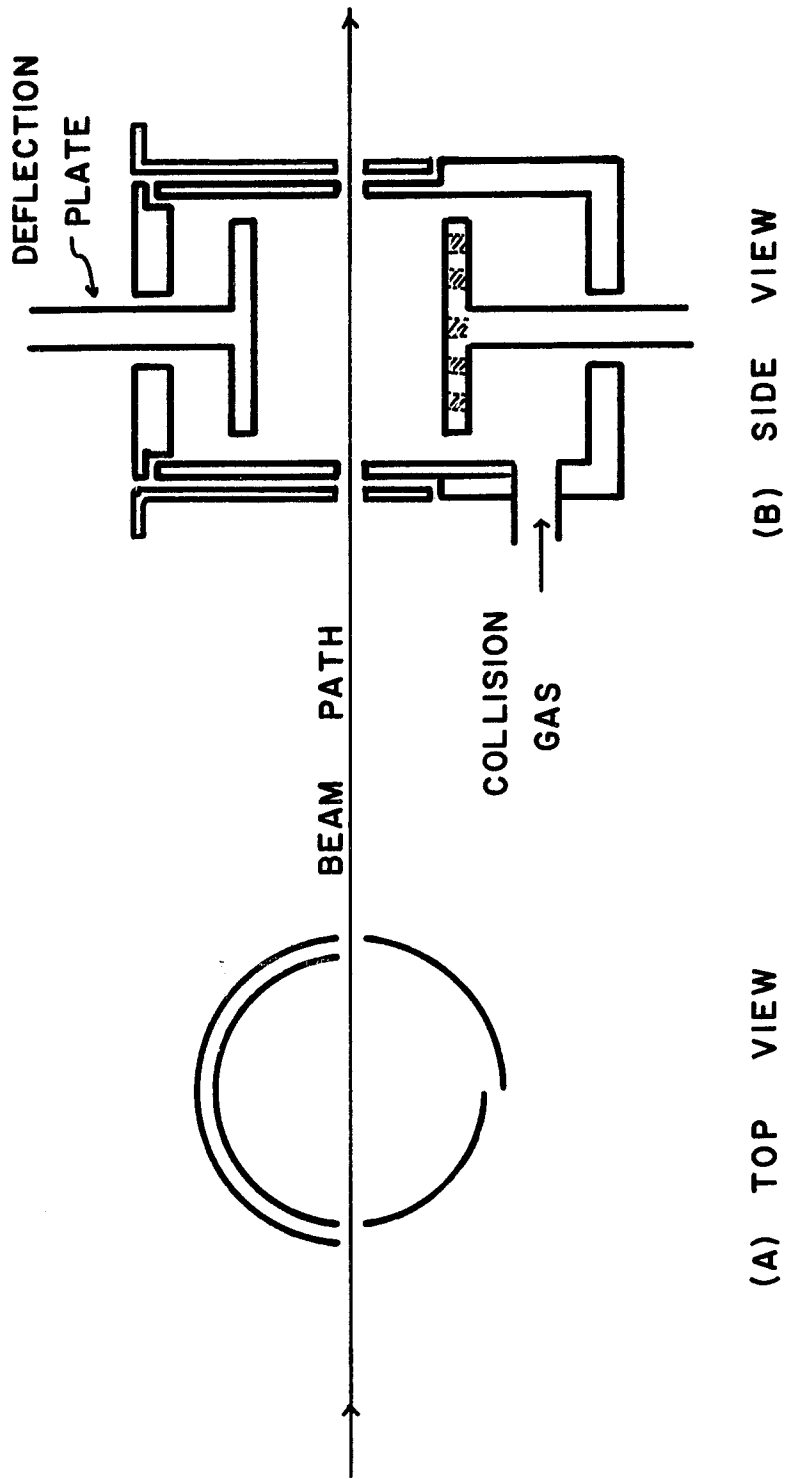


Figure 3. COLLISION CAN

bottom of the collision chamber via a glass tube from an external gas handling system, and they escape through the two slits in the side of the chamber. The target atoms are then removed from the main vacuum chamber by a 6-inch, 260 liters per second, mercury diffusion pump. Additional pumping of condensible vapors is provided by a two-liter stainless steel cold thimble maintained at liquid nitrogen temperature.

A General Radio 1230A electrometer is placed between the collision chamber and earth ground in order to read the ion current reaching the collision chamber. The electrometer can also be used to read the ion current that is deflected by a transverse potential applied to the deflection plates inside the collision chamber. Monitoring the primary beam at these two positions is very helpful when tuning the primary beam through the system.

Product Ion Analyzer

Following the collision chamber is the detection system for the scattered ions. It is a unit consisting of an energy analyzer, a mass analyzer, and a particle multiplier. This complete unit is affixed to a table which can be rotated about the center of the collision

chamber from -5° to $+90^{\circ}$ with respect to the incoming primary beam. The outer cylinder of the collision chamber is electrically isolated from, but mechanically linked to the detection unit. This allows the exit slit of the collision chamber to rotate with the detection system. The table to which the detection system is attached is rotated with a gear system which can be operated from outside the vacuum system. The angle of rotation is obtained from a potentiometer slide wire arrangement. The rotating table has a wiper which slides on a circular resistance wire. A voltage drop along the resistance wire is continuously read with a digital voltmeter and is converted into degrees. It is possible to read the scattering angle to .1 degree with this arrangement.

Immediately following the collision chamber is a 2.5 inch grounded drift tube with a 95% transparent tungsten mesh grid covering the end farthest from the collision chamber. This prevents fringe electric fields from affecting the collision region. The drift tube rotates with the detection system. Following the drift tube is a 127° cylindrical capacitor energy selector.¹⁶ The inner and outer radii of curvature of the selector are 3 cm and 4 cm respectively. Both the entrance and exit slits of the energy selector are .025 x .500 inches in size. The two dee's of the selector

are electrically isolated from the two slits as well as from the top and bottom of the velocity selector. This allows the entrance slit of the selector to be used as an accelerating or decelerating lens. By accelerating the scattered ions through a compensating voltage at different scattering angles, it is possible to pass all elastically scattered particles through the energy selector at the same energy. This removes any variation in the scattered intensity due to the energy selector having a slightly different transmission efficiency for different energies.

After the scattered ions are energy analyzed they are immediately mass analyzed by means of a quadrupole field radio-frequency-mass-spectrometer (RFMS). This type mass filter has been described in the literature,^{17,18} and the design employed is similar to that used by Landes.¹⁸

The scattered ions have now been energy and mass analyzed and are ready to be recorded as events which have occurred at a specific angle with a specific mass and energy. Immediately after passing through the RFMS the scattered ions are accelerated by 2000 volts and strike the cathode of a Bendix Model 306 particle multiplier. The 2000 volt electric field is shielded from the rest of the system by a 95% transparent tungsten

mesh which prevents fringe fields from affecting the ions before they reach the particle multiplier.

The Bendix Multiplier used in the particle counting mode has a gain of about 10^6 . The signal from the multiplier is doubly shielded out to a two-way switch located outside the vacuum system. The background count for this method of amplification is on the order of one-to-two counts per 15 seconds. This is completely negligible when compared to the intensity of the scattered ions (up to 350,000 counts/15 sec.). When observing currents on the order of 10^{-8} to 10^{-11} amperes, the two-way switch is turned so that the current can be read with a 1230A GR electrometer. These are typical current readings when tuning or examining the primary beam. When observing the scattered ion intensity, which is a much smaller current, the signal is switched and passed through a model 108 Ortec preamplifier, then into a pulse shaper and amplifier, and finally is counted as pulses by a 5201L Hewlett-Packard scalar-timer. The scalar-timer is coupled directly into a teletype for printout purposes.

Vacuum System

The total system (excluding supporting electronics) can be divided into two vacuum sections connected by the

magnetic momentum analysis system. The duoplasmatron is attached to a differentially pumped aluminum box which contains the first two lens stacks. The box is pumped with two 2-inch diameter, 30 liters/sec., stainless steel, mercury diffusion pumps. The main vacuum chamber is pumped with a 6-inch, 260 liters/sec., stainless steel mercury diffusion pump which is assisted by a 2-liter stainless steel liquid N₂ cold thimble attached to the top of the main vacuum chamber. All pumps are trapped with liquid N₂ in order to prevent contamination of the system by mercury.

The main vacuum chamber is a 28-inch diameter, 24-inch high aluminum cylinder. The vertical wall is made of 1-3/8 inch aluminum with ten 4-inch ports through which the electrical connections and gear mechanism are admitted. The top and bottom of the chamber are made of 1-3/8 inch aluminum plate, and each is vacuum sealed with an O-ring. Inside the main vacuum chamber are the third lens stack, the collision chamber, and the detection-system-table. All rest on a 3/4 inch flat aluminum plate which is attached to the vertical walls of the chamber. This attachment is necessary because the top and bottom of the chamber flex slightly when being evacuated. Pressures on the order of 10⁻⁷ torr are attainable in the main vacuum

chamber while maintaining a pressure of about 10^{-4} torr in the collision region.

Section II. Experimental Method

Before the experimental and theoretical results of this work are discussed, a brief explanation of the experimental method will be presented.

Primary Beam

The quality of the primary beam is important when performing high resolution experiments. This quality is characterized by three quantities: (1) the intensity, (2) the angular spread, and (3) the spread in energy of the primary. With high intensity primary beams ($\sim 10^{-9}$ amperes) it is possible to conduct experiments in which the statistics are quite good. In addition, the scattered count rate at large angles is sufficient for investigating the differential cross section at angles far removed from the region of the primary beam. The small angular spread (less than 1° FWHM) allows the resolution of fine oscillations in the differential cross section. The energy spread of the primary (FWHM) is 1% of the primary energy through the momentum analyzer (usually about 30 eV). A small energy spread is desirable because it allows better resolution of the data.

Primary beams of H^+ and He^+ are obtainable down to collision energies of 3 eV. Optimum beam quality is to be had in the 6 eV collision energy range. At lower energies it is difficult to keep the angular width of the beam to desirable dimensions. Small electric and magnetic fields have a greater effect on the path of the ion at lower energies.

Calibration of the Energy Selector

The energy selector is calibrated by investigating a collision process in which the probability of charge transfer is large. The system which meets this criterion is that of $He^+ + He \rightarrow He + He^+$. The charge transferred target atom remains behind after collision with an energy in the thermal range. As these thermal ions drift from the collision region through the drift tube, they are accelerated with a known constant voltage just before entering the energy selector. The variable voltage ΔV across the dee's of the selector is varied until maximum intensity of the charge transferred ions is passed. By repeating this process for different acceleration voltages, it is possible to determine a simple relationship between the energy of the ion through the energy selector and the ΔV across the dee's which produces the maximum

passed intensity. That is, $E = A\Delta V - B$, where E is the energy of the ions (in eV) incident upon the velocity selector and A and B are characteristic constants of the energy selector (1.76 and 0.06 respectively). The uncertainty of this procedure is just the uncertainty due to the thermal energy of the target particles and unknown contact potentials (both thought to be contained in the constant B). Once the energy selector is calibrated in this manner, then it can be used to check, with high accuracy, the energy of the primary beam or any charged particle which is scattered from the collision region.

Single Scattering Criterion

The deflection plates inside the collision chamber can be used to check for multiple scattering of the ions in the primary beam. In the analysis of the data, it is necessary to consider only events in which single scattering occurs. By placing a small constant voltage across the deflection plates it is possible to collect the charge transferred current without appreciably deflecting the primary beam. The charge transfer current is produced in the collision region since there is a finite probability that the incident ion will take an electron from the target atom, with the resultant ion having kinetic energy in the thermal range. These charged thermal ions are then

collected by the deflection plates. In this manner it is possible to check the intensity of the charge transfer current vs. the scattering gas pressure. Using the charge transfer total cross section (σ_{ct}) from the literature, the linear term in the expansion

$$I_s = I_0 \left(\eta L \sigma_{ct} - \frac{\eta^2 L^2 \sigma_{ct}^2}{2!} + \frac{\eta^3 L^3 \sigma_{ct}^3}{3!} + \dots \right)$$

is used to determine the number of scattering centers per unit volume (n). I_0 is the incident intensity and L is the length of the collision region (~ 2.5 centimeters). Thus when the mean free path of the incident ions (typically 60 to 90 centimeters) is found to be much greater than the dimensions of the collision region, only single scattered events are considered. Care is exercised in the experiments to be certain that only single scattered events are being recorded.

Reaction Volume

The exit slit of the momentum analyzer and the entrance slit to the collision chamber form a cone into which the incident ions can travel inside the collision chamber. Intersecting this cone is another cone which is formed by the exist slit of the collision chamber and the entrance slit of the energy analyzer. Together the

mutual volume of these two cones form a "reaction volume" inside which the ions in the primary beam must interact with the target atoms in order to be observed by the detection system. This reaction volume can be approximated by a reaction area. The size of the reaction area varies with angle, and it is necessary to adjust the intensity of the scattered data accordingly. A detailed discussion of this correction is given in reference 19.

Section III. Experimental Procedure

The following is a brief discussion of the procedure used in the collection of the data. Source gas is admitted into the duoplasmatron at a constant rate via a leak valve. At pressures of about 10^{-3} torr in the arc region of the duoplasmatron, an arc is struck by applying a voltage of up to 200 volts between the filament and the z-element (see Fig. 2). The ease with which an arc can be struck is directly related to the condition of the filament. After the arc is struck, the z-element and filament are shorted together and the arc is maintained between the filament and anode with a potential difference of about 70 volts.

The magnetic field of the duoplasmatron is used to help confine the arc to a small volume parallel to the direction of the flow of the source gas. Ions of the desired charge are extracted from the arc with a voltage of less than 15 volts and are focused by two stacks of electrostatic lenses into the momentum analyzer. The voltage on each element can be varied independently for focusing purposes.

The ion beam is collimated, momentum analyzed, and focused into the collision region by the final stack of lenses. The primary beam is now checked with the detection system for energy and angular spread. The energy

spread can be reduced by decreasing the energy of the primary through the momentum analyzer. This process is limiting in that it also reduces the intensity of the primary beam being passed by the momentum analyzer. Tuning of the duoplasmatron and all the focusing elements can improve the intensity of the primary somewhat. Also by tuning the beam it is possible to reduce the angular spread to less than 1° at FWHM.

The target atoms are admitted at a constant rate into the collision volume. A pressure of about 10^{-4} torr is maintained inside the collision volume. This pressure will single-scatter from 25 to 35% of the primary beam. The scattered particles are recorded at each $1/3$ degree interval for count times of 15 seconds.

The detection system has already been described in this Chapter. For purposes of analysis the data is punched on computer cards, and the computer is used to convert laboratory scattering data to center of mass relative differential cross sections. The collision area correction is included in the computer program, and the final data is plotted as the \log_{10} (differential cross section) vs. center of mass scattering angle.

CHAPTER III
HETERONUCLEAR SYSTEMS

Section I. Theoretical Considerations

The elastic differential cross sections to be discussed will be calculated using semiquantal techniques. A semiclassical interpretation will be employed when analyzing the detailed structure observed in the experimental differential cross sections. The phase shifts, which are required in the calculation of the differential cross sections and in the determination of the intermolecular potentials, will be calculated in two ways: (1) The phase shifts will be calculated for an assumed parameterized analytic form of the potential, where the JWKB approximation is assumed to be applicable. The validity of the JWKB approximation in the energy range of these experiments has been discussed by numerous authors. Marchi and Mueller²⁶ have compared the JWKB phase shifts to those found by direct integration of the radial Schrodinger equation for a Lennard-Jones-type intermolecular potential. They have shown that for cases where classical "orbiting" is excluded, the JWKB phase

shifts are quite reliable and give differential cross sections nearly identical to those calculated by the exact method. (2) The phase shifts will also be determined from an analytic expression which is the result of the S-matrix parameterization scheme developed by Remler.⁷ The results of using methods (1) and (2) to calculate the phase shifts and corresponding differential cross section will be given for each system to be discussed.

A. "Phase Shifts and Differential Cross Section from Parameterized Potentials."

For a given collision energy the scattering trajectories corresponding to each value of the angular momentum quantum number l are given by the classical expressions when $V(r)$, the potential-model potential, is given. From these classical trajectories the phase shift $\eta(l)$ for each l is calculated by means of the conventional JWKB method.²⁰

$$\eta(l) = \frac{\pi}{2} \left(l + \frac{1}{2} \right) - k r_c + k \int_{r_c}^{\infty} \left[\left(1 - \frac{V(r)}{E} - \frac{\left(l + \frac{1}{2} \right)^2 \hbar^2}{2\mu E r^2} \right)^{\frac{1}{2}} - 1 \right] dr \quad (1)$$

where r_c is the classical turning point or the outermost solution of the expression

$$E - V(r) - \left(l + \frac{1}{2} \right)^2 \hbar^2 / 2\mu r^2 = 0. \quad (2)$$

In all systems reported here, there is only one positive real root of Equation 2. After a variable change $r \rightarrow 1/x$ is made, the integral in Equation 1 is evaluated between limits 0.002 and $1/r_c$ by 32 points of Gaussian quadrature and throughout the calculation double precision arithmetic is used. In all cases the phase shifts are calculated for values of ℓ up to the point where $\eta(\ell) < 0.01$ radian. Then, using the Raleigh-Faxen-Holtzmark method of partial waves²¹ the scattering amplitude

$$f(\theta) = \frac{1}{2ik} \sum_{\ell} (2\ell+1) P_{\ell}(\cos\theta) (e^{2i\eta(\ell)} - 1) \quad (3)$$

and consequently the differential cross section

$$\sigma(\theta) = \frac{1}{4k^2} \left| \sum_{\ell} (2\ell+1) P_{\ell}(\cos\theta) (S_{\ell} - 1) \right|^2 \quad (4)$$

are obtained. S_{ℓ} is the appropriate S-matrix element $e^{2i\eta(\ell)}$.

In the analysis of the experimental differential cross sections, the general features of interest are the observed low and high frequency oscillations (see Fig. 4D). The following is a discussion of how one semiquantally calculates the differential cross section and semiclassically analyzes it.

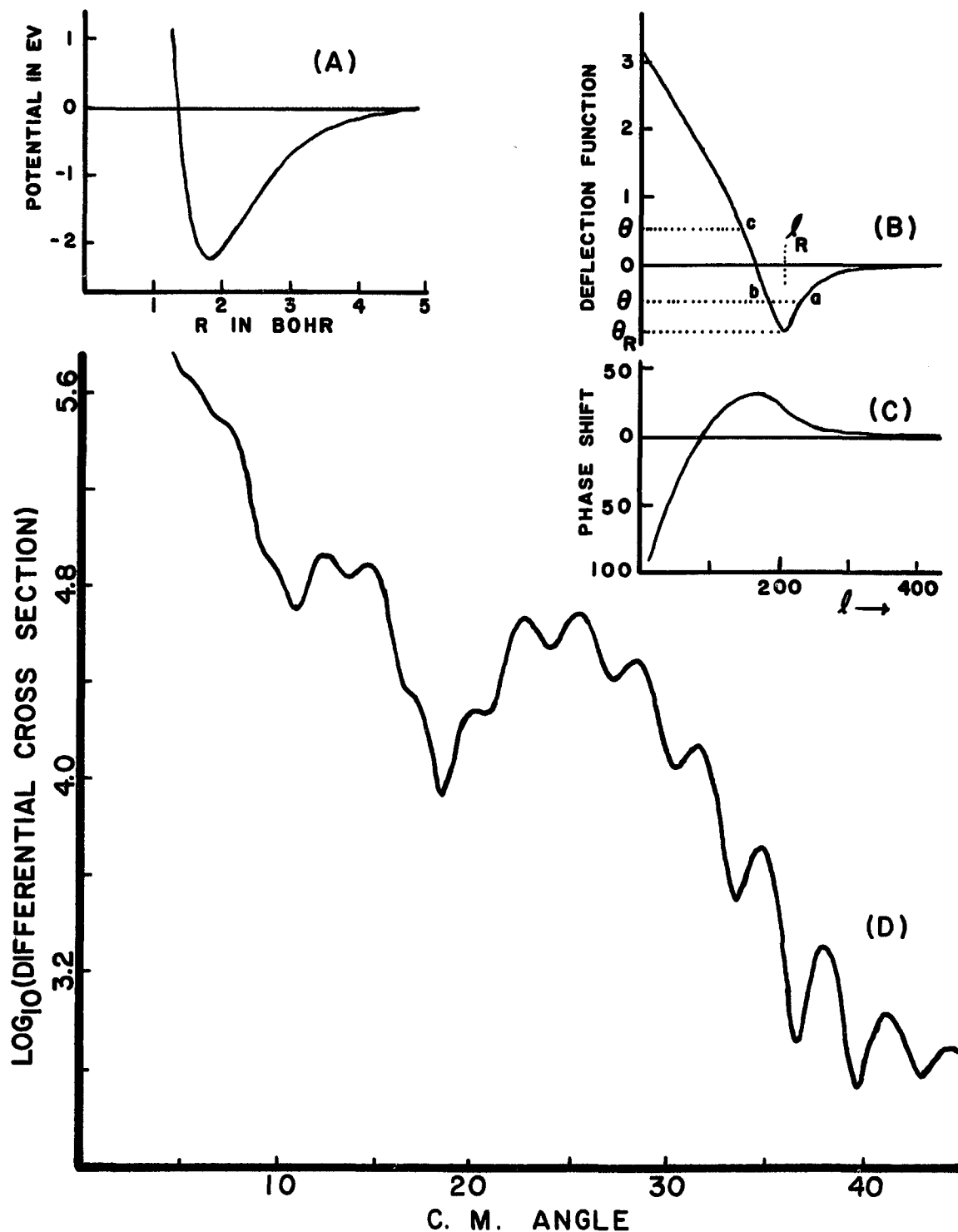


Figure 4. Steps of a potential-model calculation of the differential elastic cross section. (A) Assumed intermolecular potential. (B) Classical deflection function. (C) Phase shifts. (D) Partial wave calculation of differential cross section (ordinate = indicated value - 1.36).

If one presumes an intermolecular potential, either an ab initio calculation or a parameterized potential-model, the JWKB phase shifts $\{\eta(\ell)\}$ may be calculated and $\sigma(\theta)$ is thereby completely determined. Unfortunately this method has two disadvantages associated with it. First, the actual calculation of the partial-wave sum may necessitate the inclusion of several thousand terms, and second, many important features in the differential cross section cannot be intuitively connected with the form of the summand in Equation 3. One way of dealing with both of these difficulties is to employ the semiclassical method which is outlined in the following example. Assuming a typical intermolecular potential (Fig. 4A), the phase shifts (Fig. 4C) are calculated via Equation 1. In order to calculate the scattering amplitude semiclassically, the sum in Equation 3 is replaced by an integral and the assumption of stationary phase is employed. In this case the contributions to the scattering amplitude $f(\theta)$ come from those regions where the summand in Equation 3 has a stationary value as a function of ℓ . Such considerations have allowed the scattering amplitude to be written as an analytic function^{22,23} involving $\eta(\ell)$ and its derivatives at various points. The importance of these simplifications can be more easily seen upon introduction of the semiclassical equivalence relationship.

$$\Theta(l) = 2 \frac{d\eta(l)}{dl} \quad (5)$$

The magnitude of $\Theta(l)$ is equal to the classical center-of-mass scattering angle. Figure 4B shows a plot of the classical deflection function $\Theta(l)$ for a typical bound system shown in Figure 4A. As can be seen in Figure 4B, there are three regions of l which contribute to the same scattering angle Θ for $\Theta < \Theta_R$. Semiclassically one can think of the scattering amplitude as being the sum of the contributions from these three regions of l (i.e. l_a, l_b, l_c), and the interference seen in the resulting differential cross section (Fig. 4D) as being due to interference between these three partial waves.

The classical deflection function is made up of three branches, the two attractive branches 'a' and 'b' and the repulsive branch 'c'. The maximum attractive scattering angle Θ_R (defined as the rainbow angle) is located at l_R . For angles greater than Θ_R no interference phenomena should be seen in the differential cross sections for the heteronuclear systems reported here, since only the repulsive branch of the classical deflection function contributes to this region of the differential cross sections.

The features of a typical differential cross section such as Figure 4D can be related in a semiclassical manner to the classical deflection function. The calculated differential cross sections in this work are computed semiquantally, not semiclassically. However, the semiclassical equivalence relationship and the semiclassical ideas of interference between the different branches of the classical deflection function have been very useful when discussing and interpreting the features observed in the differential scattering cross sections. The scattering in the region of the "rainbow angle" Θ_R has been treated semiclassically by Ford and Wheeler,² and their analysis has shed considerable light on the origins of the various oscillations observed in such differential cross sections. Equations (involving different ℓ values) for the periodicities observed in the differential cross sections can be obtained from such semiclassical considerations and will be presented in Section II of this Chapter.

Some of the high frequency oscillations in the differential cross sections could not always be completely resolved in the experiments. Consequently, in order to compare any calculation to the experiment, the calculated differential cross sections are convoluted with a function

thought to be representative of the resolution of the apparatus.

B. "Differential Cross Section and Phase Shifts
from Data."

The second method of calculating the differential cross section and the corresponding set of phase shifts is the Remler-Regge method. This method obviates the necessity of calculating many terms in the partial-wave sum, and it allows one to apply his intuition about semiclassical processes to scattering experiments without making the explicit semiclassical approximations such as stationary phase, etc. The actual computation of the differential cross section using this method is not limited to the semiclassical regime; and yet, if the semiclassical theory is applicable to a particular experiment, the phase shifts and deflection function used in the calculation may be viewed in the conventional fashion. For a sufficiently well-resolved differential scattering experiment, the phase shifts may be determined from the data without recourse to any semiclassical approximations.

Watson and Summerfeld³⁹ have shown that if one multiplies the summand in Equation 3 by a factor which contains first-order poles (e.g. $1/\sin\pi\ell$ for integer ℓ) and integrates the product over the contour along the

positive real ℓ -axis, a result identical to Equation 3 is obtained. Regge²⁵ has given a general analysis of these pole positions and has determined that only simple poles occur in the first quadrant of the complex ℓ -plane. Further, if the S-matrix element contains a finite number of singularities N which are in the first quadrant of the complex ℓ -plane, the contour of integration may be deformed to include only this finite set of poles, and $f(\theta)$ may then be written as a sum over this finite set (in calculations reported here $5 \leq N \leq 10$). Remler⁷ has parameterized the (diagonal) S-matrix elements in the angular momentum representation such that they are unitary, symmetric, and contain only first-order poles. That is

$$S_A = \prod_{p=1}^N S_p \quad (6)$$

with

$$S_p = (\lambda^2 - \lambda_p^{*2}) / (\lambda^2 - \lambda_p^2)$$

where λ is the real angular momentum $\ell + \frac{1}{2}$ and λ_p is the position of the p th pole in the complex plane. Details of the explicit form of the scattering amplitude in this representation will be deferred until later in this section (see Eq. 9,10). The set of phases $\{\eta(\ell)\}$, which are necessary to predict the intermolecular potential, is derivable from the poles. At this point it is enlightening and desirable to connect the Remler-Regge method with "semiclassical thinking".

Remler has shown that the phase shift $\eta_p(\ell)$ corresponding to a particular pole location at λ_p in the first quadrant of the complex ℓ -plane may be written as

$$\eta_p(\ell) = \arctan \left[\frac{\text{Im} \lambda_p}{\lambda - \text{Re} \lambda_p} \right] - \arctan \left[\frac{\text{Im} \lambda_p}{\lambda + \text{Re} \lambda_p} \right] \quad (7)$$

The $\eta(\ell)$ resulting from a single pole is plotted in Figure 5A. The deflection function arising from this pole (using Eq. 5) is

$$\Theta_p(\ell) = 2 \left[\frac{\text{Im} \lambda_p}{(\lambda + \text{Re} \lambda_p)^2 + (\text{Im} \lambda_p)^2} - \frac{\text{Im} \lambda_p}{(\lambda - \text{Re} \lambda_p)^2 + (\text{Im} \lambda_p)^2} \right] \quad (8)$$

This function (essentially a pulse centered at $\ell = \text{Re} \lambda_p - \frac{1}{2}$ with depth $\approx 2/\text{Im} \lambda_p$ and width $\approx 2\text{Im} \lambda_p$) is also plotted in Figure 5A. The attractive portion of a set of phases (or corresponding deflection function) may be simply constructed by the superposition of a few such η_p (or Θ_p) obtained by placing additional poles in the first quadrant of the complex ℓ -plane. In practice N poles are placed on a small circle of radius ρ ($\rho \approx 1$) centered at λ_p in the complex plane. This has the phenomenological effect of one N th-order pole positioned at λ_p without entailing the mathematical complication that higher-order poles in S would necessitate. The value of ρ can be mathematically

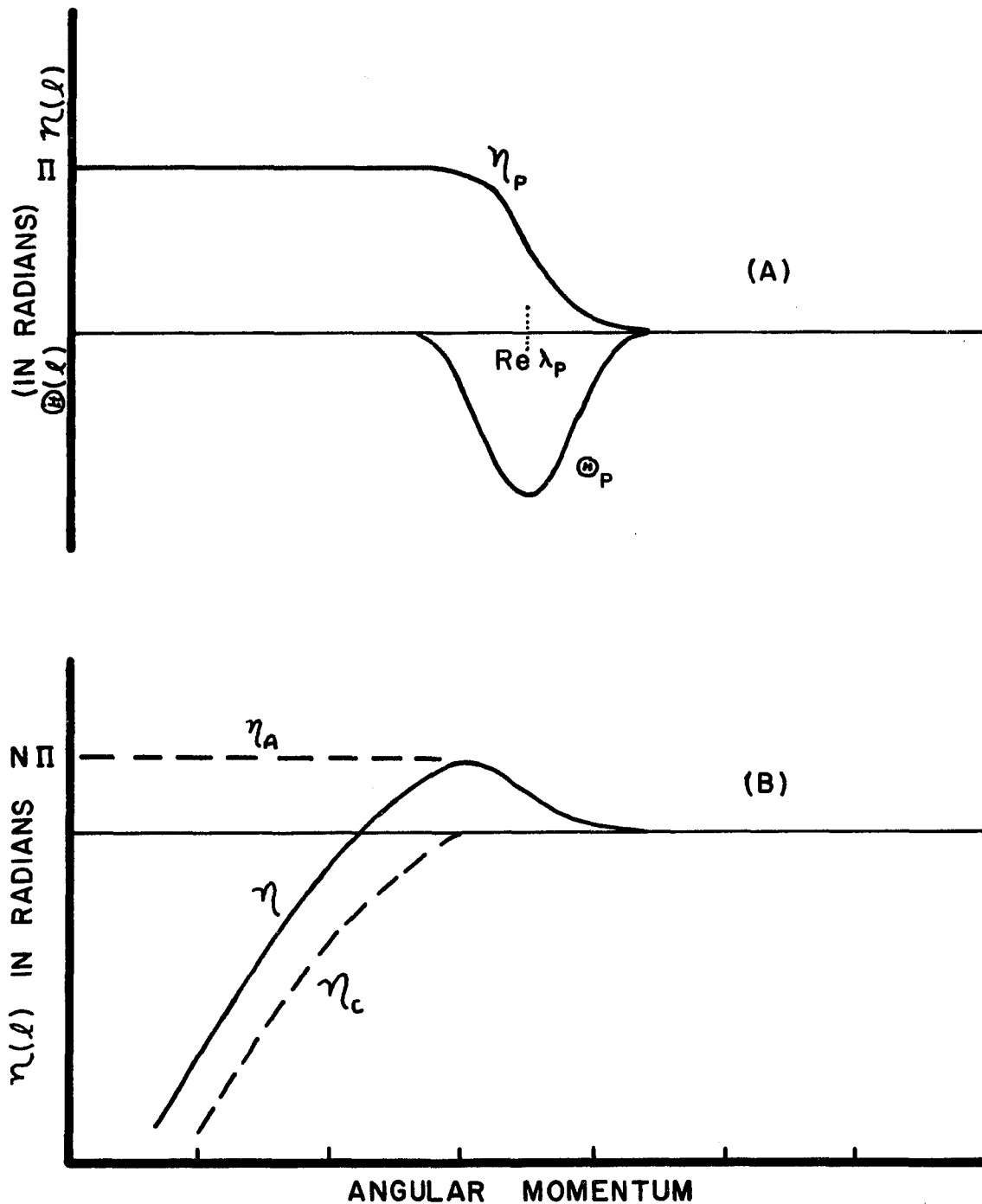


Figure 5. Remler parameterization of phase shift. (A) Phase shift η_p and deflection function Θ_p for a single pole located at λ_p . (B) Core phase shift η_c , pole phase shift η_A , and the total phase shift η for a typical attractive scattering system.

demonstrated to make little difference in the calculations of $\eta(l)$, $\Theta(l)$, or $f(\theta)$ provided it is chosen within reasonable limits. It should be emphasized that $\Theta(l)$ is not actually the basis for calculating $f(\theta)$; rather, the poles are. However, retrieving $\Theta(l)$ from the calculation allows one to use all of his intuition about semiclassical processes in manipulating the pole parameters (N and λ_p) to achieve rapid and accurate agreement between the experimental data and the Remler-Regge calculated cross section.

Since the experimental differential cross section contains interference between both attractive and repulsive components of the deflection function, the method described thus far is not complete. To include the effect of repulsive scattering one could place poles in the fourth quadrant of the complex l -plane. Instead it is more convenient to account for the repulsive scattering by going to the partial-wave expression for $f(\theta)$ and summing over the small range of l for which repulsive effects may occur. For example, if the repulsion were due to a hard core, the maximum l (say, l_{core}) in the restricted sum would be that l corresponding to the impact parameter $b = \hbar l_{\text{core}} / (2mE)^{1/2}$, which equals the core radius. In practice, a parameterized analytic function, which goes

smoothly to zero at l_{core} and is large and negative at $l = 0$ (see Appendix A), is used to represent the repulsive phase shifts because it allows flexibility in fitting the finer points of the experimental differential cross section. This analytic function contains three parameters (one independent and two dependent) which can be varied in the calculation. (1) l_0 is the l -value for which the corresponding deflection function is zero. This parameter is independent and is chosen in the calculation. (2) h_1 is the value of the deflection function when $l = (3/4)l_0$. (3) h_2 is the value of the deflection function when $l = \frac{1}{2}l_0$. By varying l_0 , h_1 , and h_2 it is possible to change the shape of the classical deflection function in the repulsive region. This parameterization of the repulsive part of the phase shifts has proved to be sufficient for the heteronuclear systems reported here.

If one assumes an analytic function for the core phase shifts η_C , which rapidly goes to zero, and adds to them the pole phase η_A , a total phase shift results (see Fig. 5B). That is,

$$\eta = \eta_C + \eta_A ; \quad S = e^{2i(\eta_C + \eta_A)} = S_C S_A$$

with

$$\eta_A = \sum_{p=1}^N \eta_p \approx N\eta_p ; \quad f(\theta) = f_C(\theta) + f_A(\theta) .$$

The scattering amplitude is the sum of the two contributions $f_C(\Theta)$ and $f_A(\Theta)$.

$$f_C(\Theta) = \frac{1}{2ik} \sum_{\ell} (2\ell+1) P_{\ell}(\cos\Theta) [S_A(S_C - 1)]$$

$$f_A(\Theta) = \frac{1}{2ik} \sum_{\ell} (2\ell+1) P_{\ell}(\cos\Theta) [S_A - 1]$$

The term $f_A(\Theta)$ is the pole contribution to $f(\Theta)$ and can be evaluated by simply summing over the poles

$$f_A(\Theta) = \frac{1}{2ik} \sum_{p=1}^N \frac{\pi}{\cos\pi\lambda_p} \left[P_{\lambda_p - \frac{1}{2}}(-\cos\Theta) \right] (\lambda_p^2 - \lambda_p^{*2}) \left[\prod_{\substack{i=1 \\ i \neq p}}^N \left(\frac{\lambda_p^2 - \lambda_i^{*2}}{\lambda_p^2 - \lambda_i^2} \right) \right] \quad (9)$$

For $l > l_C$, $\eta_C = 0$ and $S_C = e^{2i\eta_C} = 1$.

$$f_C(\Theta) = \frac{1}{2ik} \sum_{\ell=0}^{l_{core}} (2\ell+1) P_{\ell}(\cos\Theta) [S_A(S_C - 1)] \quad (10)$$

The simplicity of the application of the Remler-Regge method is very impressive. This is due to the close connection that can be drawn between it and the semiclassical idea of a classical deflection function. The deflection function parameters (Θ_R, l_R) discussed in the previous section and the full width of the deflection function at half maximum $\sqrt{l/2}$ (see Eq. 14) can be closely connected with the pole parameters of the

Remler-Regge method. By allowing λ to assume specific values (i.e. $\lambda = \text{Re}\lambda_p$ and $\lambda = \text{Re}\lambda_p \pm i\text{Im}\lambda_p$) for $\text{Re}\lambda_p \gg \text{Im}\lambda_p$, Equation 8 yields approximate values for Θ_R and $\Gamma_{1/2}$

$$\Theta_R \approx \frac{2N}{\text{Im}\lambda_p}, \quad \Gamma_{1/2} \approx 2\text{Im}\lambda_p \quad (11)$$

with $l_R = \text{Re}\lambda_p$.

Recall that the zero of the deflection function, l_0 , is an adjustable parameter in the analytic expression which represents the repulsive core.

Using these semiclassical considerations, the values for N , $\text{Re}\lambda_p$, $\text{Im}\lambda_p$ and l_0 may be reasonably well approximated by inspection of the experimental data. The Remler-Regge method may then be used to predict the differential cross section. On the basis of this calculation the set of parameters may be adjusted and this procedure repeated until satisfactory agreement between data and calculation is achieved.

The decoupling of the parameters $\text{Re}\lambda_p$ and $\text{Im}\lambda_p$ as well as the simple relation between $\text{Im}\lambda_p$ and N (seen in Eq. 11) makes the iterative procedure to obtain $\eta(l)$ from the experimental cross section quick and efficient.

C. "Intermolecular Potential from Phase Shifts"

If the phase shifts can be obtained by methods such as the Remler-Regge, which was just discussed, then the

intermolecular potential (within the realm of the validity of the JWKB approximation) can be uniquely determined.

The procedure is to first solve for the "quasipotential" $Q(t)$.²⁴

$$Q(t) = \frac{4E}{\pi k} \frac{1}{t} \frac{d}{dt} \int_t^{\infty} \frac{B \eta(B) dB}{(B^2 - t^2)^{1/2}}, \quad (12)$$

where E = collision energy, k = wave number,

$$B = (\ell + \frac{1}{2})/k, \quad \eta = \text{JWKB phase shift},$$

and where the intermolecular potential $V(r)$ is related to $Q(t)$ through the expressions

$$V(r) = E \left(1 - e^{-\frac{Q(t)}{E}} \right), \quad r(t) = t e^{\frac{Q(t)}{2E}} \quad (13)$$

The parameter t is the generator of values of r and $V(r)$ and is normally cycled from about .5 to 5. The expression for $Q(t)$ is evaluated by numerical integration after a variable change, $B = t/\cos\alpha$, is made. It should be pointed out that for small values of t (i.e. the region where $Q(t)$ is positive), extremely accurate integration schemes are necessary in order to obtain satisfactory values for $r(t)$. Double precision arithmetic is employed throughout for evaluating $Q(t)$.

Section II

Application

The potential model and Remler-Regge method of calculating the differential cross section, which were discussed in Section I of this Chapter, will now be applied to the proton-rare gas atom systems.

A. H⁺ + He

The measured elastic differential scattering of protons by Helium at 4 eV collision energy is shown in Figure 6A. The high and low frequency oscillations are clearly resolved in the region of the rainbow angle. For this molecular-ion three separate approaches to the determination of the intermolecular potential will be considered: (1) the inverted potential calculation where the phase shifts are obtained from a Remler-Regge calculation, (2) the potential-model (here-after called P-M) calculation, and (3) potentials which are the result of ab initio calculations. These will be compared and the areas of agreement and disagreement discussed.

The first step in the inversion of the intermolecular

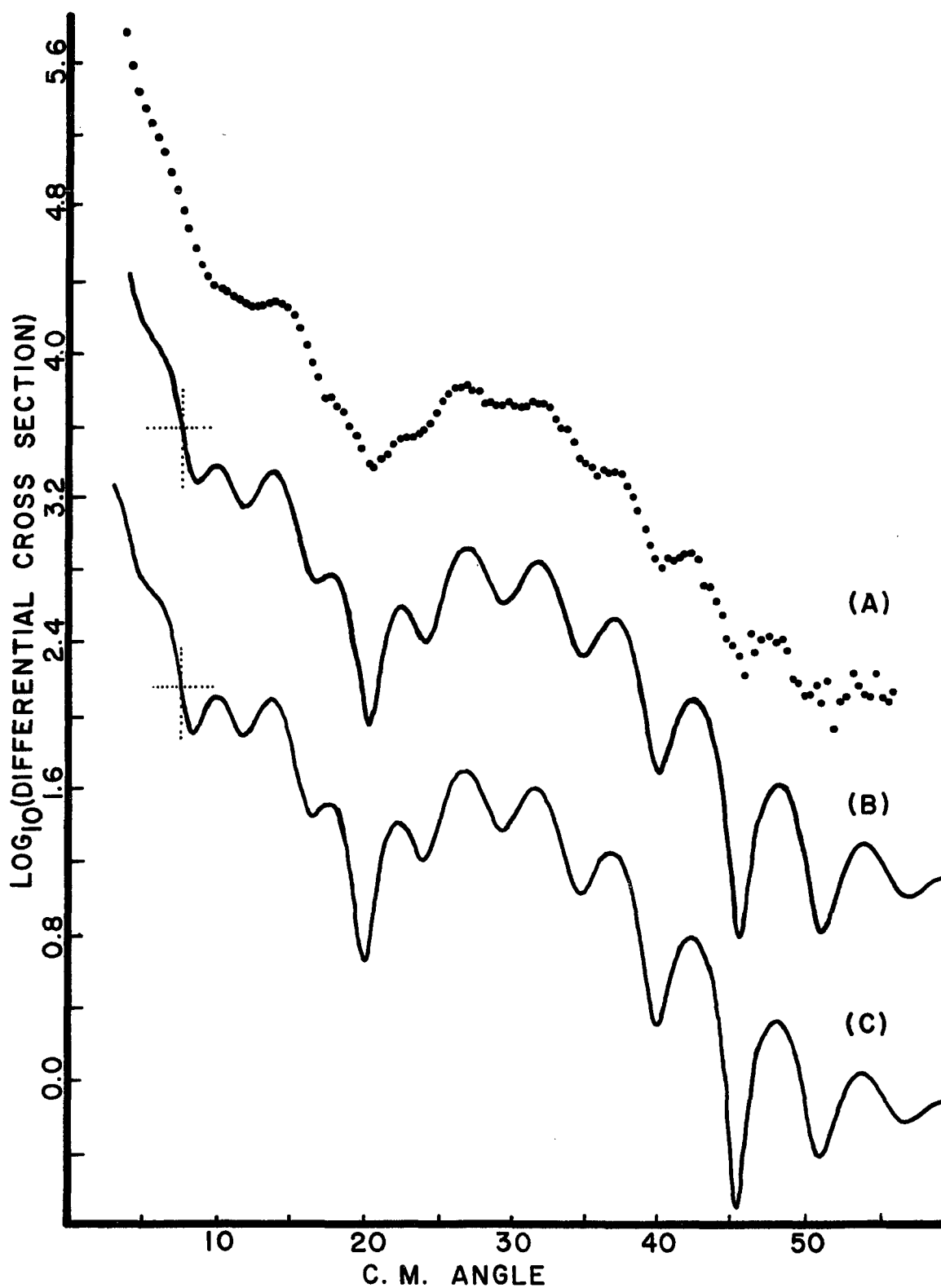


Figure 6. Elastic differential cross section of $H^+ + He$, $E = 4$ eV. (A) Experiment. (B) Inverted potential calculation. (C) Potential-model calculation. (See Table III for value of calculation at indicator.)

potential is to bring the Remler-Regge calculation, Figure 6B, into good agreement with the data, Figure 6A. The initial choice of pole parameters is clearly motivated by semiclassical considerations. The rainbow angle θ_R and the width $\Gamma_{1/2}$, may be readily approximated by fitting the low-frequency oscillatory term (i.e. the Airy function) of the Ford and Wheeler rainbow approximation

$$Ai^2 \left[(\theta - \theta_R) / q^{1/3} \right] \quad (14)$$

where

$$\Gamma_{1/2} = (2 \theta_R / q)^{1/2}$$

to the low-frequency oscillations in the experimental data in the vicinity of the rainbow angle (q being the curvature of a parabola fit to the deflection function in the rainbow region). The large-angle, high-frequency component of the differential cross section determines the value of $l_R + l_C$. That is, from the semiclassical expression for the differential cross section² (assuming stationary phase), the periodicity of the high frequency oscillations is given by

$$\Delta \theta_{h.f.} = \frac{2\pi}{l_R + l_C} \quad (15)$$

where $\Delta \theta_{h.f.}$ is the angle between adjacent maxima of the high-frequency component of the cross section. The value

of l_0 is initially approximated as the average of l_R and l_C . Using the initial estimates for σ_R , $l_R + l_C$, and $\Gamma_{1/2}$, an approximate deflection function is determined. The deflection function may then be related to the pole parameters via Equation 11, and the Remler-Regge method may be used for a prediction of the differential cross section. This technique gives a reasonable first approximation of the pole parameters, and some variation of these parameters is necessary to bring the Remler-Regge calculated differential cross section into very good agreement with the experimental differential cross section. Figure 6B is a plot of the results of this calculation, and the agreement between it and the data is seen to be excellent. Parameter values used in this calculation are given in Table I.

The criteria used to determine how well the calculation and experiment agree are; (1) the positions of the low frequency oscillations (the minima being easiest to compare), (2) the position of the high frequency oscillations, especially in regions of the data which have steep slopes, (3) the relative amplitudes of adjacent high frequency oscillations in the calculation must be the same as in the experiment (This is very sensitive in the regions of the minima of the low frequency

oscillations.), (4) the general slope of the data compared to that of the calculation. When all four of the above are in very good agreement, the comparison is said to be excellent. The agreement is considered good if only condition (4) is violated. If (1), (2), or (3) is violated, the agreement is thought to be only qualitative. The agreement in Figure 6 is termed excellent. The apparent difference in the amplitudes of the high frequency oscillations between the calculation and experiment is due only to the choice of convoluting function used in the calculation.

The differential cross section at scattering angles greater than the rainbow angle is determined by the repulsive branch of the intermolecular potential. Since little data was taken in this region for the proton-rare gas systems, the repulsive part of the classical deflection function (and thereby the repulsive phase shifts) in the Remler-Regge calculation could be adequately represented by a linear function. The value of the parameters h_1 and h_2 in Table I reflect this choice for the repulsive phase shifts. This simple parameterization of the repulsive branch is sufficient since the actual shape

of the deflection function in this region does not significantly influence the detailed structure observed in the data.

The inversion method outlined in Section I-C is used to construct the intermolecular potential using the phase shifts retrieved from the Remler-Regge calculation. The inverted potential is shown in Figure 7A.

The second method used to determine the intermolecular potential is to assume a parameterized potential, to calculate the corresponding phase shifts for each angular momentum l -value (Eq. 1) and the differential cross section (Eq. 4). In this type calculation it is necessary to first choose an analytic form of the potential. Two potential forms which have received much attention in molecular structure calculations are the Lennard-Jones and Morse-type potentials. Modified forms of both of these potentials were used in the initial stages of this work. After some preliminary work the Lennard-Jones-type potential was abandoned because it was less flexible than the Morse-type potential.

The modified Morse potential to be used is

$$V = \epsilon \left[e^{2G_1 G_2 (1-\rho)} - 2e^{G_1 G_2 (1-\rho)} \right] \quad (16)$$

$$G_2 = 1 \text{ for } \rho < 1$$

$$G_2 \neq 1 \text{ for } \rho \geq 1$$

where ϵ is the potential well depth and $\rho = r/r_m$, r_m being

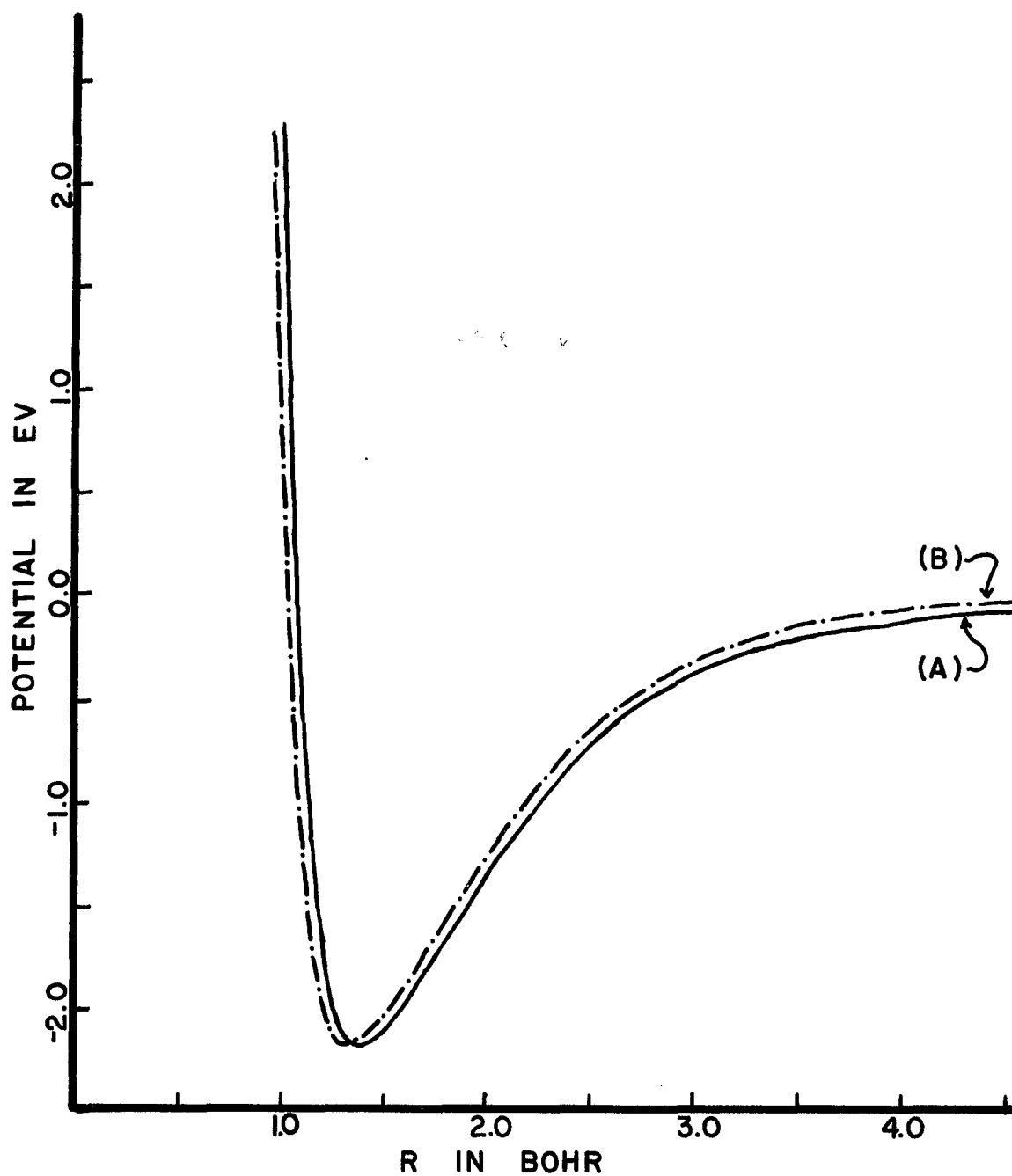


Figure 7. Intermolecular potentials retrieved from $H^+ + He$ experiment, $E = 4$ eV. (A) Inverted potential ($r_m = 1.41a_0$, $\epsilon = -2.18$ eV). (B) Potential-model potential ($r_m = 1.31a_0$, $\epsilon = -2.18$ eV).

the position of the potential minimum. G_1 and G_2 are parameters which affect the shape of the potential and are chosen (along with r_m and ϵ) to give a potential which will best reproduce the data. Mittmann et al.²⁷ have used this potential form to analyze their work, which is similar to some of the systems reported here. Other authors have also used this form of the Morse potential in calculations of differential elastic scattering for other systems. 8,11

The potential-model calculation of the differential cross section which best fits the $H^+ + He$ data is shown in Figure 6C. The corresponding P-M potential is shown in Figure 7B. The parameters used in this calculation are shown in Table I.

The agreement between the $H^+ + He$ data (Fig. 6A) and the potential-model calculation (Fig. 6C) is very good. It is clearly seen in Figure 6 that both Remler-Regge and P-M methods of calculating the differential cross section give excellent agreement with the experimental data.

In the determination of the intermolecular potential by both the P-M and inverted method it has been found that different regions of the potential influence different regions of the differential cross section. The region $r > r_m$ of the intermolecular potential has the greatest influence on the interference patterns observed in the

calculated differential cross section. The shape of the potential in this region is very important and must be varied with extreme care if the data is to be reproduced in detail. In Figure 7 it is readily apparent that both potentials are the same 'shape' in the region $r > r_m$. The region of the potential $r < r_m$ is reflected in the repulsive scattering in the post-rainbow region of the differential cross section. Since little data was obtained in this region of the differential cross section for the $H^+ + He$ system, only qualitative statements can be made about the repulsive region of the intermolecular potential. The differences which are observed between the two potentials in Figure 7 are not experimentally significant.

Mittmann and his co-workers²⁷ have made P-M calculations on their recent $H^+ + He$ experiments. Their calculational procedure is the standard partial wave calculation in which a potential model is assumed (Eq. 16) in order to calculate the set of phase shifts to be used in a RFH sum to calculate the scattering amplitude. In Figure 8 a calculation using Mittmann's potential is compared to our 4 eV $H^+ + He$ data. It is easily seen that the calculation and data are not in good agreement. The calculated rainbow angle is too small and the wave length

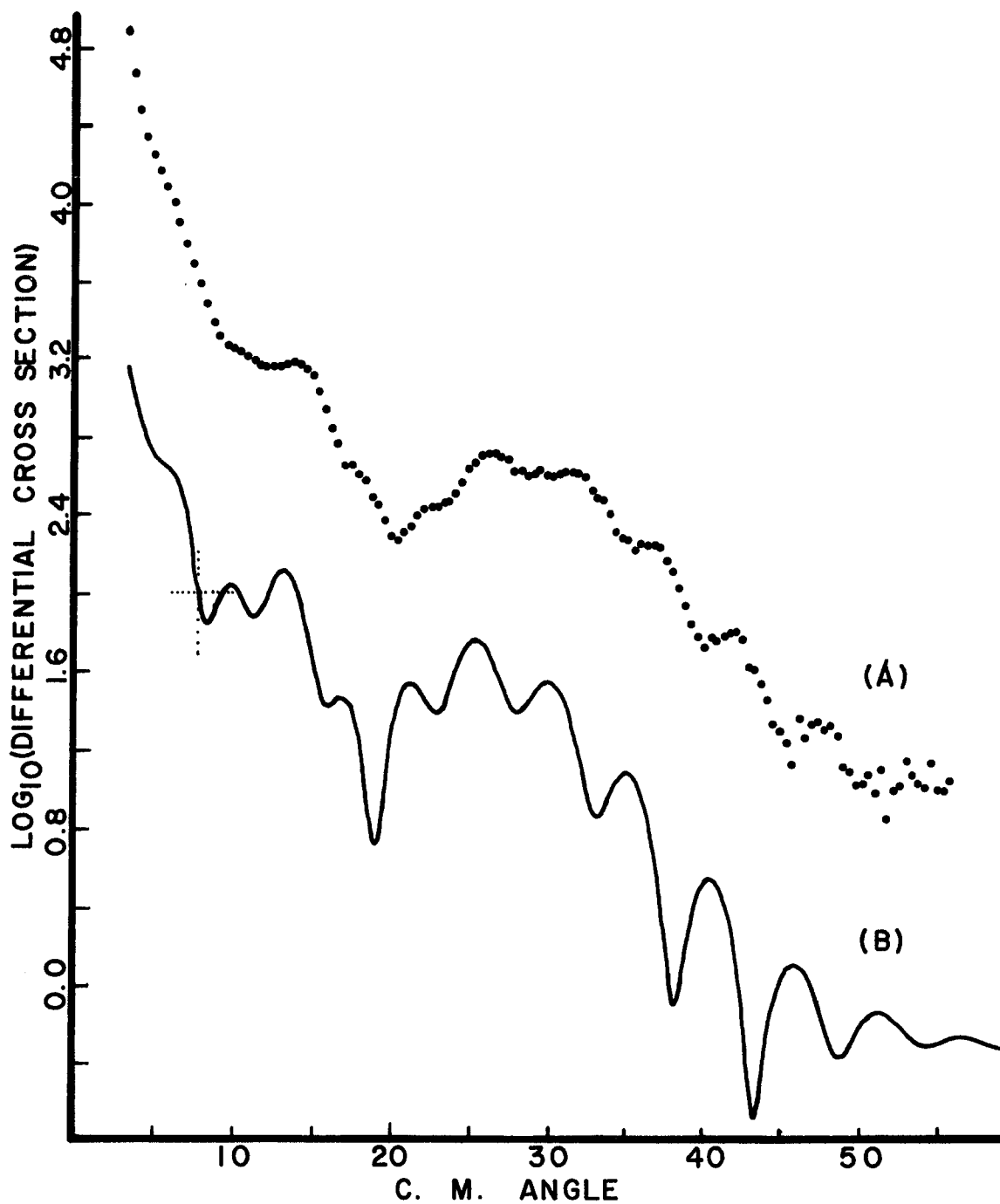


Figure 8. Elastic differential cross section for $H^+ + He$, $E = 4$ eV. (A) Experiment. (B) Mittmann's potential-model calculation. (See Table III for value of calculation at indicator.)

of the high frequency oscillations is too short. The result of this is that both wavelengths (high and low frequency) are shorter than those seen in the data. Therefore, one of the most obvious points of comparison between data and calculation (i.e. ratio of high frequency oscillations per low frequency oscillation) is maintained. The preservation of this ratio is apparently what Mittmann was trying to reproduce in his calculations in the rainbow region. Even in the data and calculations published by him,²⁷ it is possible to discern that there are too many low frequency oscillations in his calculations when compared to his data, especially at small angles. Figure 9 shows a comparison of the inverted potential and the Mittmann potential for $H^+ + He$ at 4 eV collision energy.

Extensive ab initio calculations of the intermolecular potential of HeH^+ have been made in the region of r_m and the recent calculations of Wolniewicz²⁸ are believed to be the most accurate to date. Wolniewicz has computed by the variational method the ground state in which the wavefunction employed was a 64-term generalized James-Coolidge expansion. Figure 10 shows a graph of both the inverted potential and the Wolniewicz points. It is unfortunate that the Wolniewicz points do not extend to larger values of r . As it stands, no absolute statement

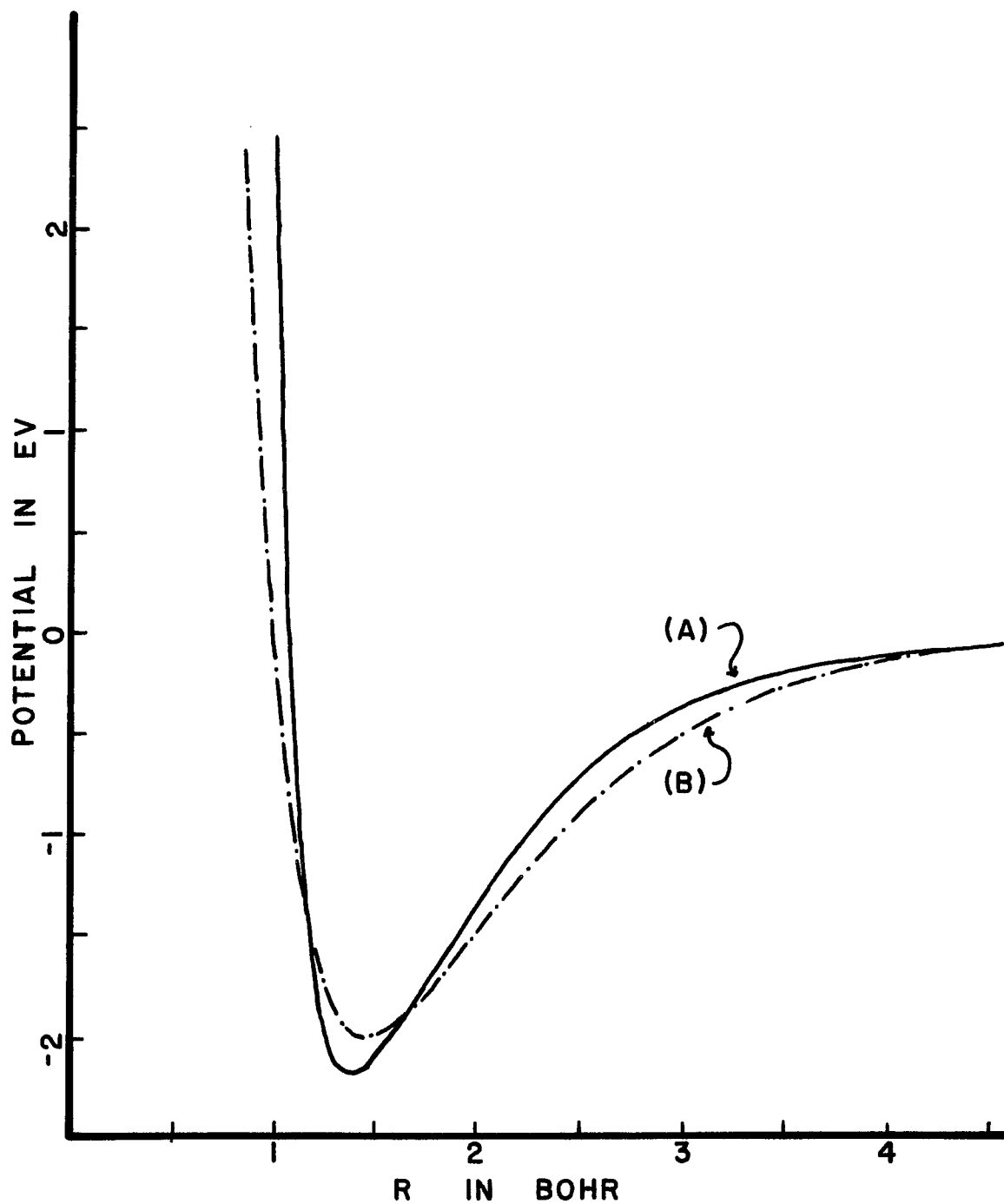


Figure 9. Comparison of intermolecular potentials for $H^+ + He$, $E = 4$ eV. (A) Inverted potential ($r_m = 1.41a_0$, $\epsilon = -2.18$ eV). (B) Mittmann's potential-model ($r_m = 1.45a_0$, $\epsilon = -2.00$ eV).

of agreement or lack of agreement can be made about the two calculations. In the Wolniewicz calculation the effort was to establish good values for r_m and ϵ . These Wolniewicz values agree with the r_m and ϵ of the inverted potential to within 3% and 7% respectively. Since the details of the scattering are less sensitive to these parameters than to other characteristics of the intermolecular potential, the agreement is surprisingly good.

A realistic analytic function²⁹ has been fit to the points of Wolniewicz and extended to larger values of r . The differential cross section calculated utilizing the Wolniewicz-analytic-fit was indeed very good. This was, at first, quite misleading in that the resulting differential cross section is more a result of the choice of the analytic function in the extended area of r than it is a function of the analytic fit in the region of the Wolniewicz points. It should be pointed out that agreement between the Wolniewicz-fit and the inverted potential in the region $r > r_m$ is very good. Of course, the result of this is that both potentials will yield calculated differential cross sections which compare very favorably with the data since the data effectively samples the region $r > r_m$. However, the Wolniewicz-analytic-fit is no better than an assumed potential-model in the region beyond the Wolniewicz points.

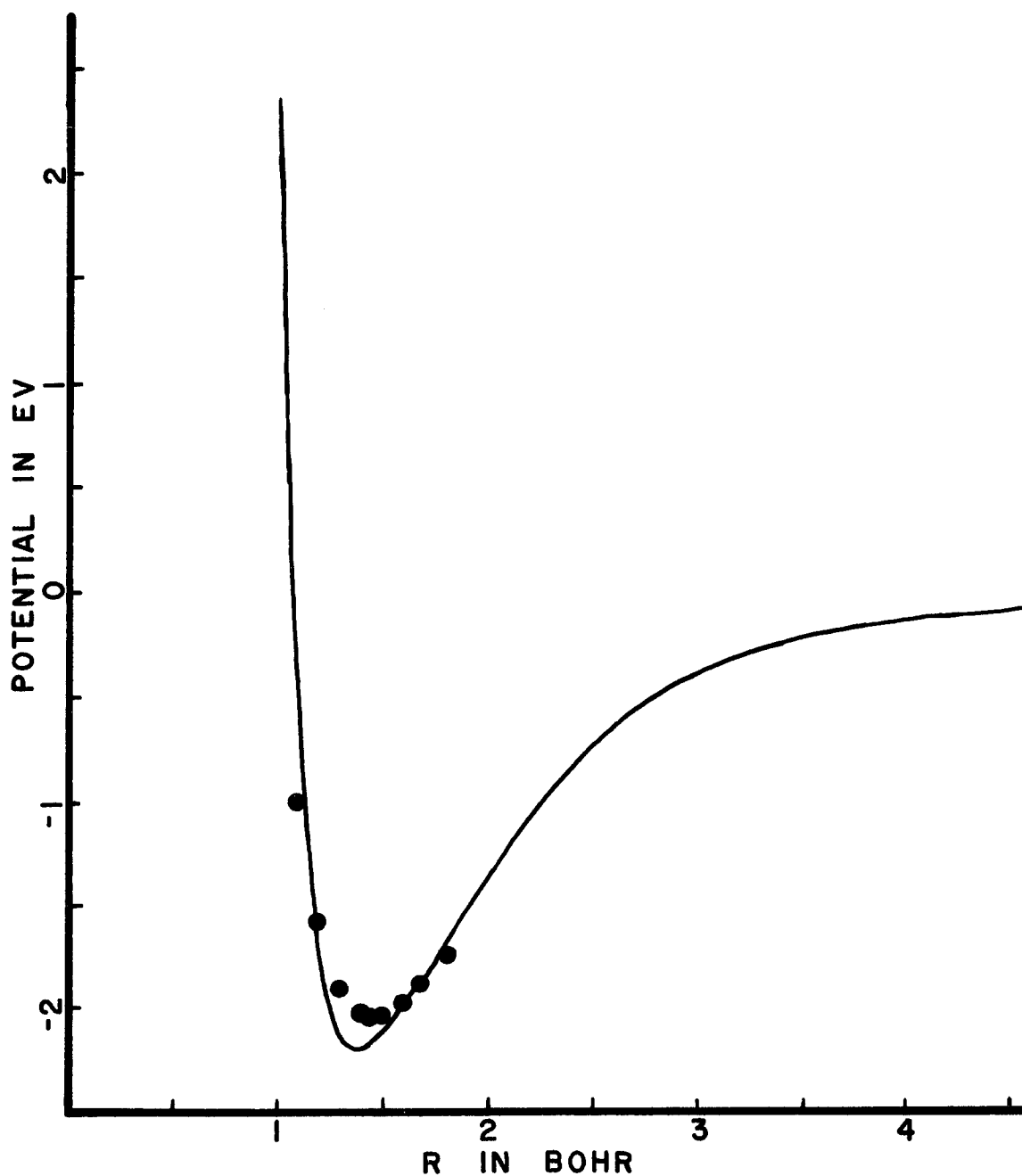


Figure 10. Comparison of intermolecular potentials for $H^+ + He$, $E = 4$ eV. Solid line is the inverted potential retrieved from the experiment ($r_m = 1.41a_0$, $\epsilon = -2.18$ eV). The points are from the ab initio calculation of Wolniewicz ($r_m = 1.46a_0$, $\epsilon = -2.04$ eV).

B. H⁺ + Ne

The H⁺ + Ne experiments were performed in the energy range $3 \leq E \leq 18$ eV. The 5.71 eV data has been selected for analysis because it has the best resolution of both high-and-low frequency oscillations seen in the data. The methods of analyzing the differential scattering are the same as in the previous sections on the H⁺ + He system

The best inverted potential fit to the data (see Fig. 11A,B) is quite good in the positioning of both the low and high frequency oscillations. Some difficulty was encountered in deciding upon the proper value of the parameter N, the number of poles. This is due to the fact that only one secondary rainbow (i.e. low frequency oscillation other than the primary rainbow) is clearly resolved in the data. The number of secondary rainbows increase with increasing N. After several iterative calculations of the differential cross section, it was possible to fix the number of poles at seven.

The very distinct fine oscillations observed in the experimental data in the region of the rainbow serve to fix the value of $l_R + l_C$ (via Eq. 15) while the low-frequency rainbow structure determines the rainbow angle as well as the curvature of $\Theta(l)$ (via Eq. 14).

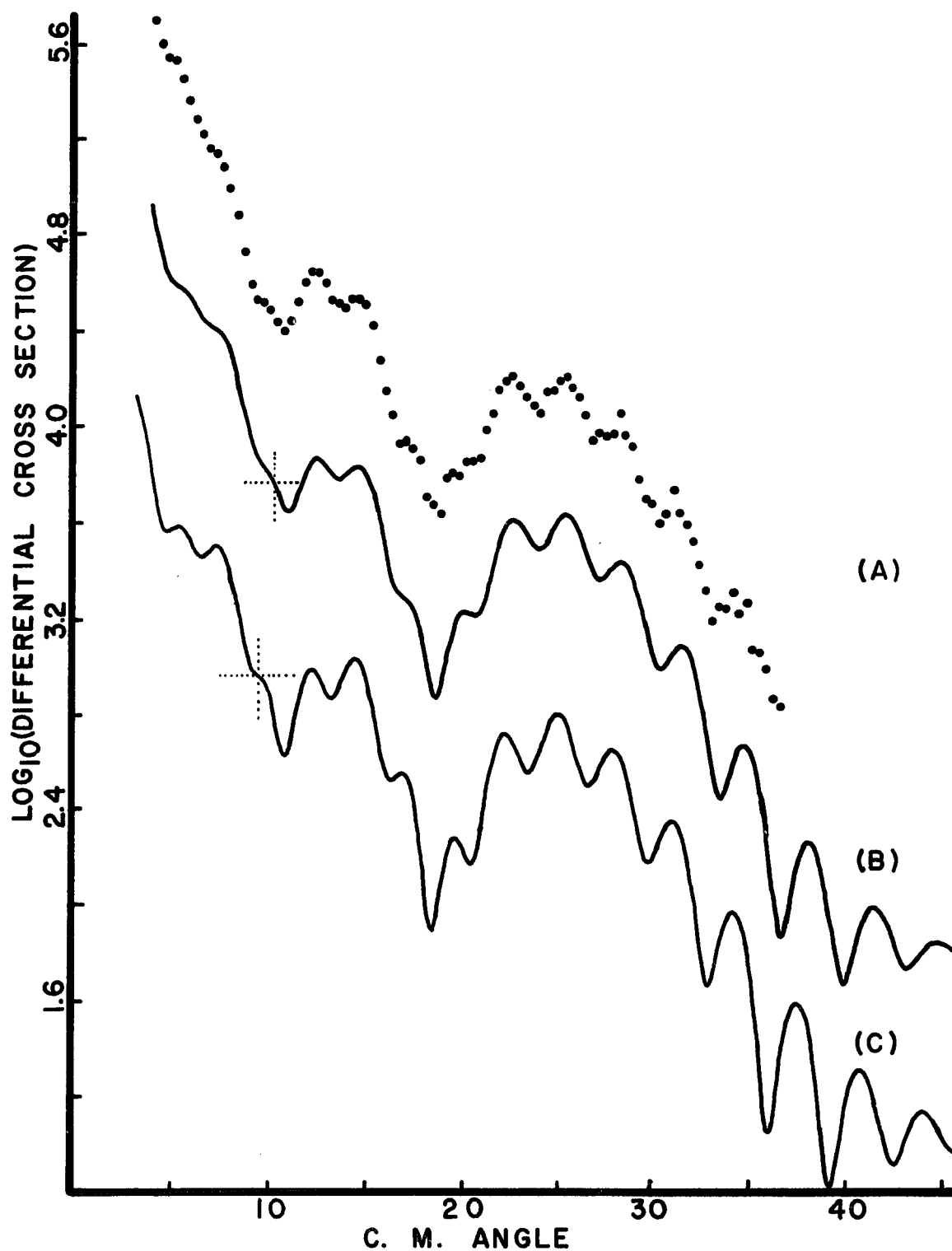


Figure 11. Elastic differential cross section for $H^+ + Ne$, $E = 5.71$ eV. (A) Experiment. (B) Inverted potential calculation. (C) Potential-model calculation. Both calculations are extremely good fits to the experiment. See Table III for value of calculation at indicator.

Thus, one can obtain initial values for the pole parameters. The Remler-Regge method is then iteratively employed to bring the calculation into agreement with the experimental differential cross section. These final pole parameters (see Table I) and the resulting phase shifts have been inverted yielding the intermolecular potential seen in Figure 12A.

The potential-model calculation and the data for the $H^+ + Ne$ system are shown in Figure 11A,C. As can be seen, the agreement is again very good. The potential-model potential for NeH^+ is shown as circles in Figure 12. The agreement between this potential and the inverted potential is excellent.

Mittmann et al.²⁷ have also made calculations on the NeH^+ system. His P-M calculation is compared with the data in Figure 13. There exists a one degree shift between the experimental and calculated primary rainbow angles. The origin of this discrepancy is the same as that discussed earlier in the Mittmann analysis of $H^+ + He$. In order to keep the ratio of high frequency oscillations in the rainbow region the same as that seen in the data, Mittmann has decreased the wavelength of both frequencies. The lack of agreement between calculation and data is most noticeable in the 18° region.

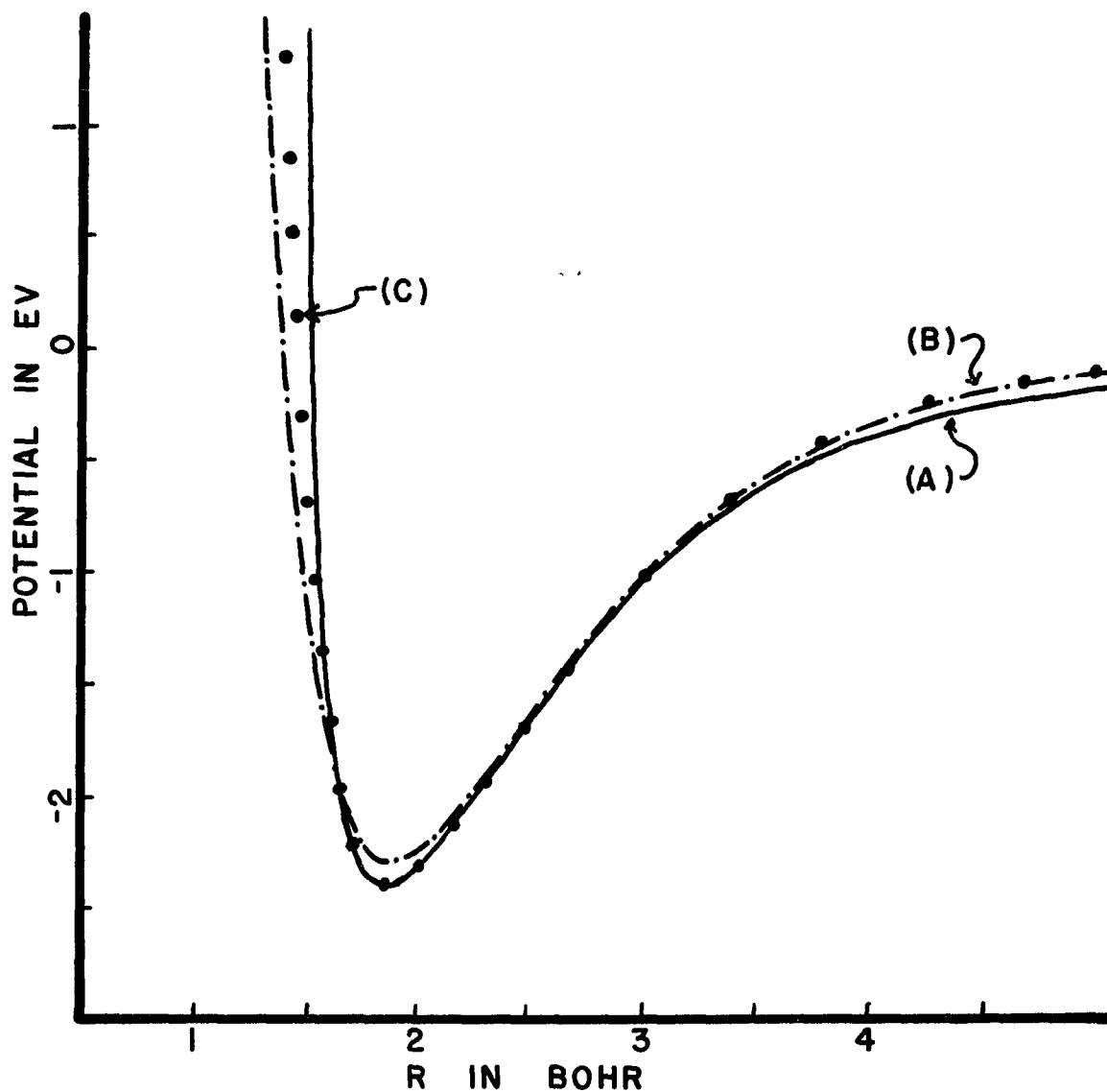


Figure 12. Intermolecular potentials retrieved from $H^+ + Ne$ experiment, $E = 5.71$ eV. (A) Inverted potential ($r_m = 1.85a_0$, $\epsilon = -2.39$ eV). (C) Potential-model potential ($r_m = 1.85a_0$, $\epsilon = -2.39$ eV). (B) Mittmann's potential-model potential ($r_m = 1.87a_0$, $\epsilon = -2.28$ eV).

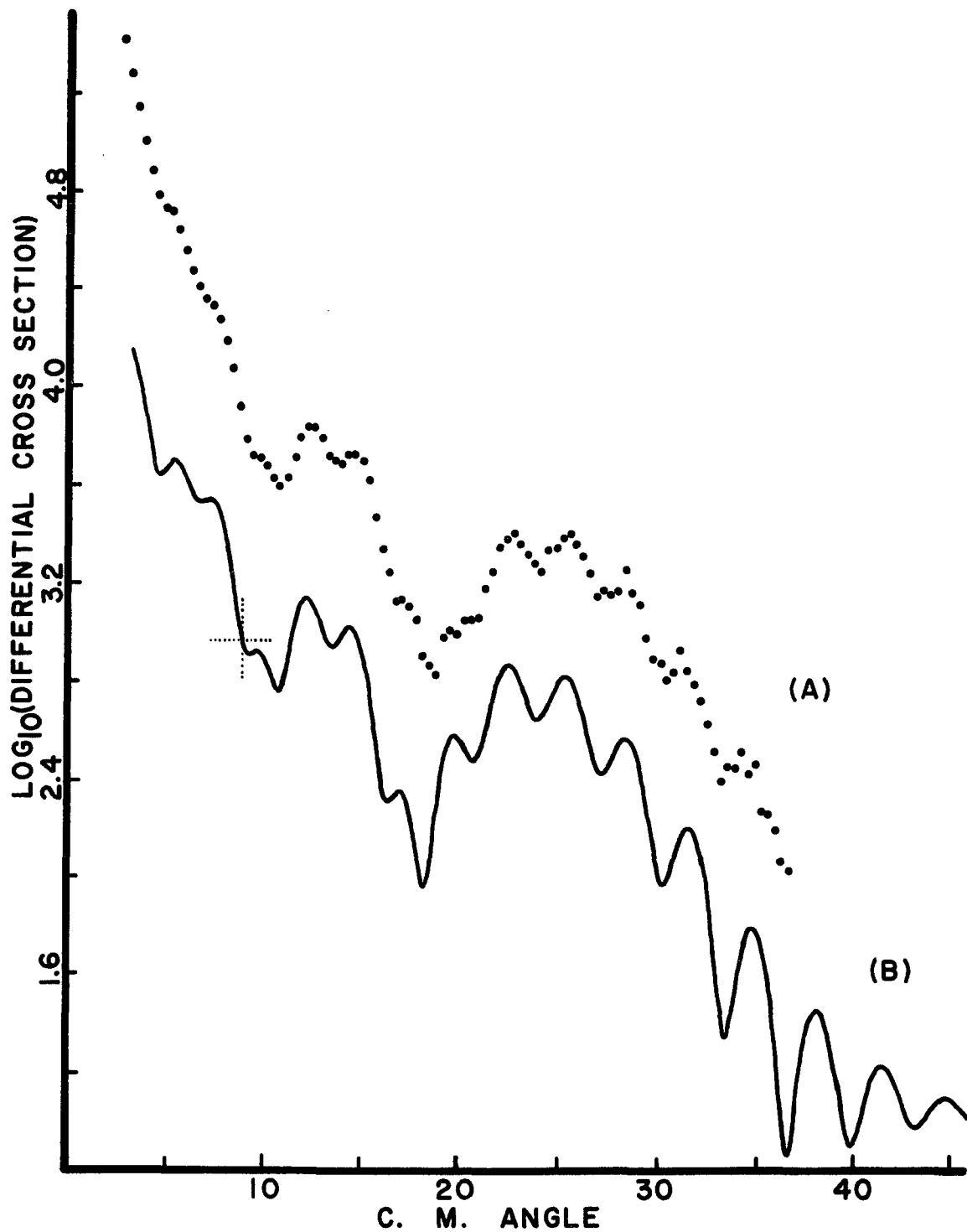


Figure 13. Elastic differential cross section of $H^+ + Ne$, $E = 5.71$ eV. (A) Experiment. (B) Mittmann's potential-model calculation. Note lack of agreement in the $15 - 20^\circ$ region. See Table III for value of calculation at indicator.

The latest ab initio calculation on the NeH^+ system is that of Peyerimhoff.³⁰ Peyerimhoff has used Hartree-Fock-Roothan Type wavefunctions to construct Slater-type molecular orbitals in order to calculate points of the intermolecular potential for the NeH^+ system. A basis set of 24 functions was used. In order to estimate the error in the calculation, Peyerimhoff made a similar calculation for the HeH^+ system. Then assuming the Wolniewicz²⁸ HeH^+ calculations to be the most accurate, the Peyerimhoff HeH^+ calculations were within 1% of the Wolniewicz value for r_m and within 6% of the Wolniewicz value for ϵ . Thus the Peyerimhoff well depth for NeH^+ is believed to be correct to about 6%. Peyerimhoff thought an error of 6 to 7% was acceptable due to the difficulty of the calculation. The NeH^+ calculation is more difficult than the HeH^+ calculation because of the larger number of electrons involved.

Figure 14 is a comparison of the inverted potential and the Peyerimhoff calculated points. For comparison purposes, an analytic function was fit to the Peyerimhoff points, and the differential cross section for this analytic fit was calculated. The resulting differential cross section is not in as good agreement with the data as are the inverted or the P-M potential calculations. The 7%

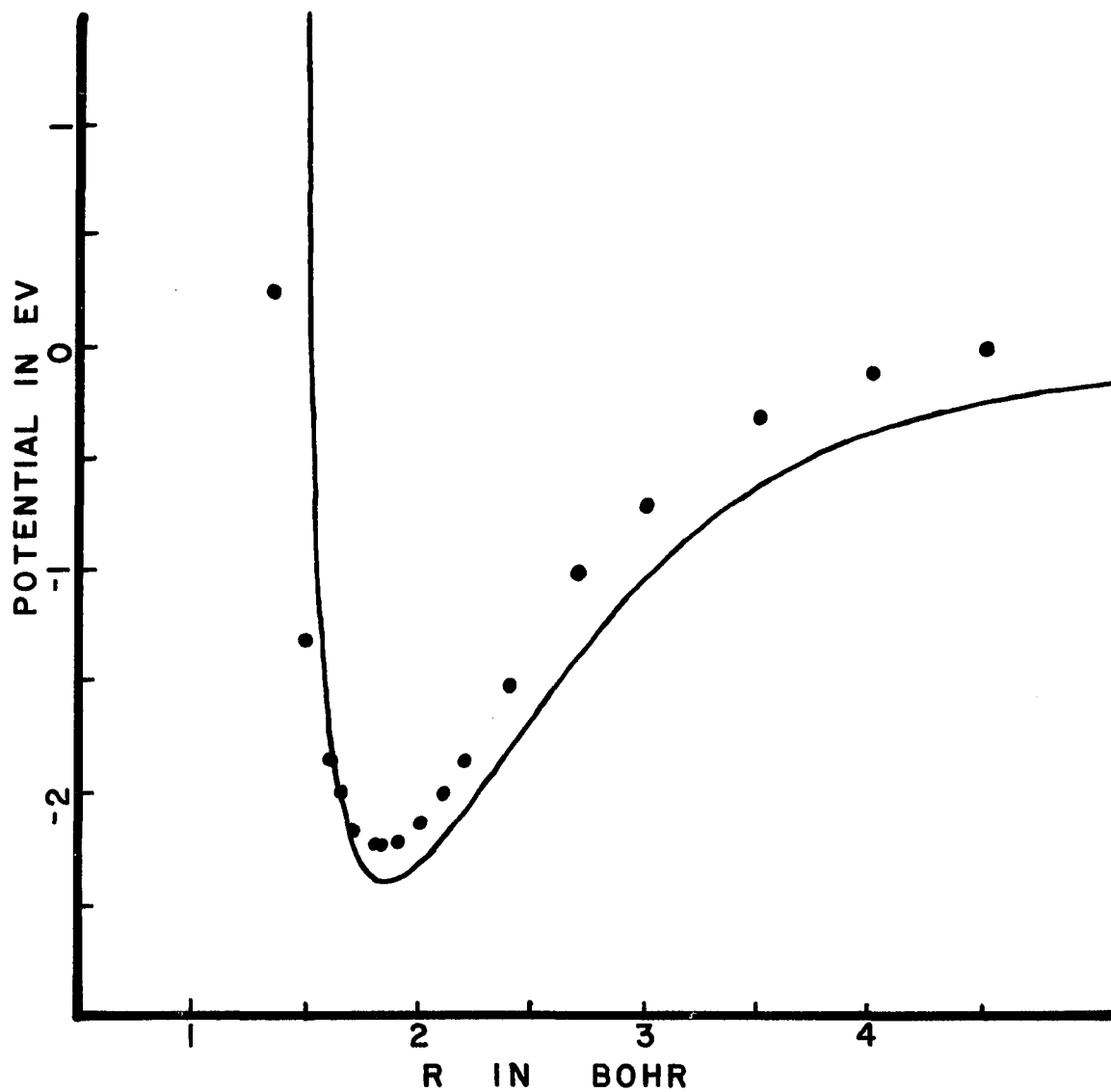


Figure 14. Intermolecular potentials for $H^+ + Ne$, $E = 5.71$ eV. Solid line is the inverted potential ($r_m = 1.88a_0$, $\epsilon = -2.38$ eV). The points are the ab initio calculations of Peyerimhoff ($r_m = 1.83a_0$, $\epsilon = -2.21$ eV).

difference between ϵ for the inverted potential and the Peyerimhoff potential is acceptable for two reasons. First, Peyerimhoff has estimated that the error in his calculation could be as much as 6 or 7%, and second, the differential scattering experiment is not sensitive to this region of the potential. The r_m values of the Peyerimhoff potential and the inverted potential for NeH^+ agree to within 3%.

C. Conclusion

It has been found that the region of the intermolecular potential $r > r_m$ governs the periodicity and position of both frequencies observed in the data. That is, a small change in the potential in the region $r > r_m$ produces very significant changes in the calculated differential cross section. On-the-other-hand, small changes in either r_m or ϵ do not significantly affect the calculation.

In the present analysis both methods (P-M and Remler-Regge) of determining the intermolecular potential yield good results for those portions of the potential effectively sampled by the experiments. However, the S-matrix formalism of Remler is inherently a more powerful method of analysis. For example, if one had a complicated

differential cross section, it should be possible to reproduce the differential cross section by properly placing first order poles in the complex l -plane. Calculations of the same differential cross section could be extremely difficult or even impossible using a Morse or Lennard-Jones type potential in a P-M calculation.

The general method used in this work to determine the intermolecular potential for such bound systems as HeH^+ and NeH^+ is the most reliable method presently known. Potential-model calculations have been made on $\text{H}^+ + \text{He}$ at 3, 4, and 6 eV using the same P-M potential. In each case the comparison between data and calculation (both high and low frequency oscillations) is excellent. The intermolecular potentials reported should be independent of the collision energy within the energy range of the investigation ($3 \leq E \leq 18$ eV) in this work. However, only the best resolved data are analyzed. To have analyzed the higher energies, which are less well resolved, could result in potentials which differ because of the resolution quality of the experiment, not because of real differences in the scattering process.

TABLE I

PARAMETERS

POTENTIAL-MODEL				REMLER-REGGE					r_m (a_0)	ϵ (eV)		
G_1	G_2 ($P < 1$)	G_2 ($P \geq 1$)	$G_1 G_2$	N	R	I	ℓ_0	h_1			h_2	
<u>H⁺ + He</u>												
Potential Model	3.30	1.0	0.59	1.96							1.32	2.18
Mittmann ^a	2.20	1.0	0.85	1.87							1.45	2.00
Inverted					5	44	15.0	29.5	1.57	.785	1.41	2.18
Ab Initio ^b											1.46	2.04
<u>H⁺ + Ne</u>												
Potential Model	3.24	1.0	0.70	2.28							1.85	2.39
Mittmann ^a	2.68	1.0	0.85	2.28							1.87	2.28
Inverted					7	72	25.8	50.5	1.78	.992	1.88	2.38
Ab Initio ^c											1.83	2.21

G_1 and G_2 are parameters in the Morse potential used in P-M calculations. N, R, I, ℓ_0 , h_1 , & h_2 are parameters used in inversion calculations (Remler-Regge). a. Mittmann, et al., Zeitschrift Fur Naturforschung, 26a, 1112 (1971). b. Wolniewicz, L., J. Chem. Phys. 43, 1087 (1965). c. Peyerimhoff, S., J. Chem. Phys. 43, 998 (1965).

CHAPTER IV
HOMONUCLEAR SYSTEMS

Section I. Discussion

The He_2^+ molecular-ion has received much theoretical and experimental attention in the past decade. The lowest gerade ($2\Sigma_g^+$) and ungerade ($2\Sigma_u^+$) molecular states have been the object of many calculations. The ability to reproduce reasonable values for the gerade (g) and ungerade (u) states of He_2^+ has become a measure of the validity of calculations which are made in like manner on other molecular-ions. In 1963 Reagan, Browne, and Matsen³¹ made calculations on the ungerade state of He_2^+ using Slater-type orbitals as a basis for a 26-term atomic orbital-configuration. Two years later (1965) Lorents and Aberth⁹ published their experimental measurements of the elastic differential scattering of the $\text{He}^+ + \text{He}$ system. Their series of experiments contained collision energies from 20 to 600 eV. The Lorents-Aberth work has since been cited by many authors as a basis of comparison between theoretical calculations and experiment. In the work reported here experiments were performed in the energy range $3 \leq E \leq 15$ eV.

Marchi and Smith⁸ were the first to attempt analysis of the Lorents-Aberth data. They assumed that two states were adequate to describe the interference seen in the data. Employing analytic fits to the calculated points of Reagan et al.³¹ for the ungerade potential and to the calculated points of Phillipson¹² for the gerade potential, Marchi and Smith calculated the elastic differential cross section for $\text{He}^+ + \text{He}$. The experimental data together with their analysis produced tremendous insight into the two-state scattering problem of homonuclear systems. In 1967 Olson and Mueller¹¹ again analyzed the Lorents-Aberth data using a nine parameter version of the two potentials (the u and g potentials of Marchi and Smith being used as a starting point) in a standard JWKB partial wave sum calculation of the differential cross section. The nine potential parameters were evaluated by using a least-squares criterion to minimize the difference between the experimental differential cross section and computed differential cross section at each angle in order to determine the best two parameterized intermolecular potentials. Also in 1967 Gupta and Matsen¹⁰ calculated the lowest gerade state using a 26-term valence-bond function. In addition Gupta and Matsen extended the u-state calculation of Reagan et al. to smaller values of internuclear separation.

Recently several papers have appeared on the He_2^+ system. In 1971 Weise, Mittmann, Ding, and Henglein³² reported their experimental investigation of the rainbow region of the ungerade potential for $^4\text{He}^+ + ^4\text{He}$ scattering. Their work was in the 10 to 30 eV collision energy range. They compare their results to those of Gupta and Matsen.¹⁰

The latest theoretical work reported is that of Gilbert and Wahl³⁷ and that of Liu.³⁸ Gilbert and Wahl compare their calculations with the Olsen-Mueller¹¹ analysis of the Lorents-Aberth⁹ experiment. Liu has calculated the dissociation energy of the u-state of He_2^+ and has obtained a rigorous lower bound for the well depth of 2.469 ± 0.006 eV.

In the work reported here the collision energy is reduced to 6 eV in order to move the primary rainbow to larger angles and thereby resolve more of the secondary rainbow structure. Data are also taken at other collision energies, but the maximum amount of pre- and post-rainbow structure is resolved at 6 eV. In all the He_2^+ experiments the differential cross section covers the angular range $3^\circ \leq \Theta \leq 180^\circ$. This large range in scattering angle (previous work was to 36° only) allows effects due to nuclear symmetry to be observed in the angular region $\Theta > 90^\circ$. All combinations of the scattering of the two Helium isotopes are reported ($^4\text{He}^+ + ^4\text{He}$, $^3\text{He}^+ + ^3\text{He}$, $^4\text{He}^+ + ^3\text{He}$, and $^3\text{He}^+ + ^4\text{He}$).

In order to render the analysis of this data tractable, it is necessary to hold either the gerade or ungerade potential fixed. Then by varying only one potential, agreement between data and calculation can be achieved. In the calculations presented here the gerade potential is assumed to be known. The reason for this choice is that the value of the gerade potential in the region of interest has not changed appreciably in the last two theoretical calculations.^{10,12} The same is not true of the ungerade potential.

The experimental data for the homonuclear systems will be analyzed in two ways: (a) via an inverted potential calculation (using the Remler-Regge method to calculate the phase shifts); (b) via a potential-model calculation in which the potential is assumed to be known before the differential cross section is calculated. Finally these results will be compared with the results of existing ab initio calculations for He_2^+ .

The importance of r_m (the equilibrium position of the ungerade potential) and ϵ (the ungerade potential well depth) as points of comparison between the work of different groups will be discussed. A semiclassical discussion of the oscillations seen in both the calculated differential cross section and the experimental differential

cross section will be given. It is impressive that the wavelength of each interference observed in the data or calculation can be associated with the semiclassical idea of interference between partial waves with different l -values being scattered to the same angle. The periodicity of this interference can be shown (using semiclassical methods) to be $2\pi/(\ell_A \pm \ell_B)$, where ℓ_A and ℓ_B are the appropriate points on the deflection function for one-state considerations or the appropriate points on the different deflection functions for two-state considerations.

Section II. Theoretical Considerations

The basic theory related to the low energy two-state scattering of $\text{He}^+ + \text{He}$ was first reported in the early thirties.^{33,34} More recently Marchi and Smith⁸ gave a very good discussion of the physical and theoretical concepts needed to understand the detailed structure seen in the low-energy differential elastic cross sections in their analysis of the $\text{He}^+ + \text{He}$ elastic scattering of Lorents and Aberth.⁹

Due to the symmetry involved in homonuclear scattering, the electronic wave functions for the molecular-ions fall into two orthogonal families -- the gerade and ungerade states. For the low energy experiments (6 eV collision energy) being reported here, it is necessary to consider only the lowest member of each family of states.

Attention will first be directed to elastic scattering in which there is no nuclear symmetry. If nuclear symmetry is ignored, the differential cross section for two-state scattering can be written as,

$$\sigma(\theta) = \frac{1}{4} |f_u(\theta) + f_g(\theta)|^2 \quad (17)$$

where the scattering amplitudes at angle θ are the usual Rayleigh-Faxen-Holtzmark sum

$$f_{u,g}(\theta) = \frac{1}{2ik} \sum_{\ell} (2\ell+1) P_{\ell}(\cos\theta) [e^{2i\eta_{u,g}(\ell)} - 1] \quad (18)$$

with u and g signifying the ungerade and gerade potentials respectively. When it is necessary to consider nuclear symmetry in addition to the electronic symmetry (i.e. when the nuclei are identical), the differential cross section can be expressed as³⁵

$$\begin{aligned} \sigma(\theta) = \frac{1}{4} \{ & x | f_g(\theta) + f_g(\pi-\theta) + f_u(\theta) - f_u(\pi-\theta) |^2 \\ & + (1-x) | f_g(\theta) - f_g(\pi-\theta) + f_u(\theta) + f_u(\pi-\theta) |^2 \end{aligned} \quad (19)$$

where $x = (s + 1)/(2s + 1)$ $s = \text{nuclear spin} = 0, 1, 2, \dots$

$x = s/(2s + 1)$ $s = \text{nuclear spin} = \frac{1}{2}, 3/2, \dots$

The above equation is valid for both boson scattering (${}^4\text{He}^+ + {}^4\text{He}$) and fermion scattering (${}^3\text{He}^+ + {}^3\text{He}$). When different isotopic masses of Helium are used (e.g. ${}^3\text{He}^+ + {}^4\text{He}$), the nuclear symmetry is removed, and Equation 17 is used to calculate the differential cross section.

The gerade phase shifts used in this work are calculated using the JWKB approximation and the analytic fit of Marchi and Smith⁸ to the ab initio points of Phillipson.¹² The analytic fit to the calculated points

is better than 5% in the low energy region of interest in these experiments. The ungerade phase shifts, on the other hand, are calculated two different ways. One method is to use the S-matrix formalism of Remler to calculate the phase shifts associated with the ungerade potential. The potential which is an inversion of this set of phase shifts will be called the inverted (ungerade) potential. The ungerade phase shifts are also calculated by assuming a form of the modified Morse potential (Eq. 16) and calculating the phase shifts using Equation 1. This will be called the (ungerade) potential-model method of calculating the differential cross section.

The method of calculating the differential cross section is via Equation 17 or 19, depending upon the nuclear symmetry of the reactants. The two independent methods of calculating the ungerade phase shifts allow two independent differential cross section calculations to be made. For each differential cross section, the calculation and data are brought into agreement using an iterative procedure in which only the ungerade potential is varied.

Before discussing the complicated structure observed in the $\text{He}^+ + \text{He}$ systems, it is instructive to look at the different scattering amplitudes which are involved

in the scattering. This procedure will allow the different frequencies observed in the data to be examined independently. In this manner it is possible to extract maximum information from the analysis of the different frequencies observed in the calculation or data. The detailed structure observed in the differential cross sections can be related semiclassically to the deflection functions involved in the scattering. For the $\text{He}^+ + \text{He}$ system it is possible to have scattering with nuclear symmetry (e.g. ${}^3\text{He}^+ + {}^3\text{He}$) and without nuclear symmetry (e.g. ${}^3\text{He}^+ + {}^4\text{He}$).

When nuclear symmetry is ignored, the elastic differential cross section contains three different frequencies (see Fig. 16). Two of these frequencies are the low and high frequency oscillations resulting from the attractive well of the ungerade potential. These are the low frequency rainbow oscillations along with the superimposed high frequency fine structure which are observed for scattering angles less than the rainbow angle (see Fig. 15B). Curve A of Figure 15 shows the differential cross section assuming direct (i.e. no nuclear symmetry) gerade scattering only, and curve B shows direct ungerade scattering only. The two frequencies being discussed are obviously the result of only ungerade potential.

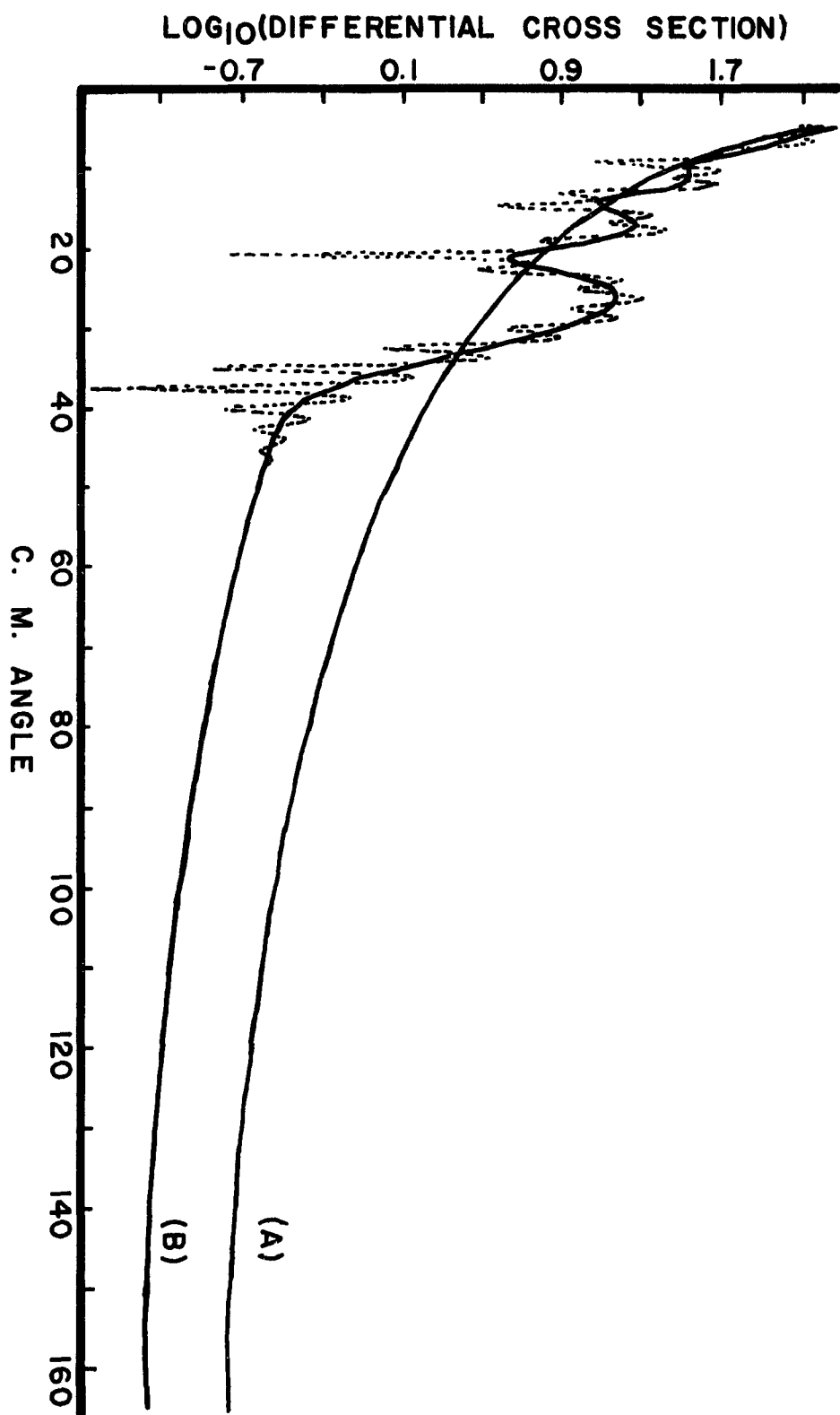


Figure 15. Contributions to the elastic differential cross section of ${}^3\text{He}^+ + {}^3\text{He}$, $E = 6$ eV. (A) Direct scattered differential cross section $|f_g(\theta)|^2$. (B) Direct scattered differential cross section $|f_u(\theta)|^2$. Note that the gerade scattering is dominant in the post-rainbow region.

The purpose of showing the gerade and ungerade differential cross sections separately is to point out the dominance of gerade scattering in the post-rainbow region and to note that the structure seen in the rainbow and pre-rainbow regions is due to ungerade scattering. The third frequency in the differential cross section (no nuclear symmetry) is due to interference between partial waves which are scattered by different potentials and is dominant in the post-rainbow region. This interference is clearly seen in Figure 16, where the differential cross section resulting from the sum of the gerade and ungerade scattering amplitudes (Eq. 17) is shown and the three frequencies under discussion are easily identified. It should be pointed out that assuming a superposition of two states in this manner (which is assumed for all homonuclear calculations made in this work) is a restricted use of the two-state theory. In general, the interaction between two states in a two-state theory (e.g. curve crossing) excludes the use of simple superposition. However, in this particular set of experiments there is no interaction between the states involved because they are of different symmetry, and as a result superposition can be successfully used. Interaction with higher states of the same symmetry is ruled out because the collision energy is restricted to values well below threshold for any inelastic processes.

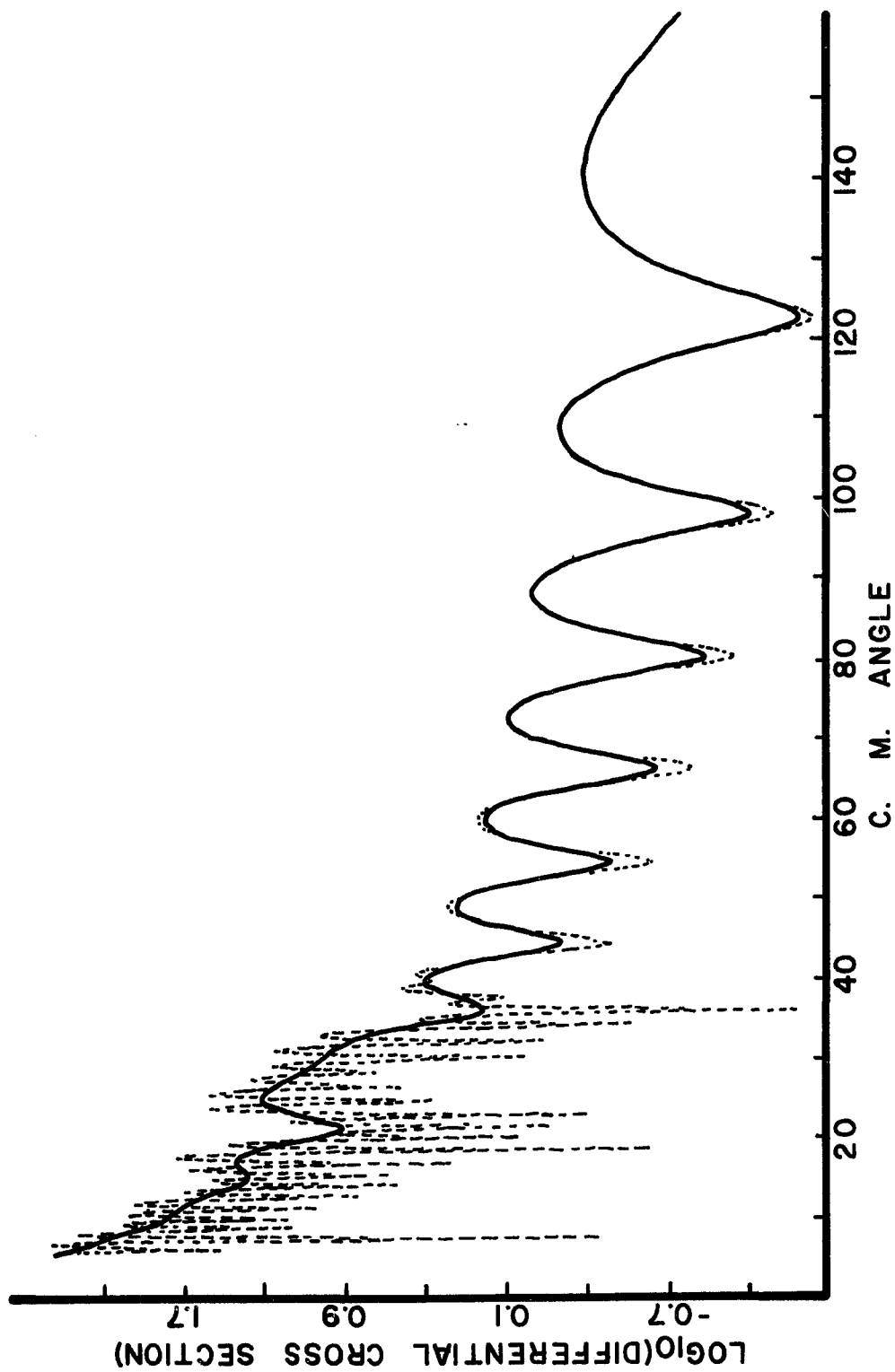


Figure 16. Elastic differential cross section of ${}^3\text{He}^+ + {}^3\text{He}$, $E = 6$ eV. The two-state direct scattered interference $|f_g(\theta) + f_u(\theta)|^2$ in the differential cross section is dominant in the post rainbow region.

Figure 16 corresponds to the scattering of ${}^3\text{He}^+ + {}^4\text{He}$ or ${}^4\text{He}^+ + {}^3\text{He}$ for which there is no nuclear symmetry. The period $\Delta\theta$ of the oscillations observed in the differential cross section at angles greater than the rainbow angle can be associated with partial waves by use of the semiclassical relation

$$\Delta\theta = \frac{2\pi}{|\ell_A - \ell_B|} \quad (20)$$

where ℓ_A is the ℓ -value on the classical deflection function for state A at angle θ , and ℓ_B is the ℓ -value on the classical deflection function for state B at angle θ (see Fig. 18). The period of the oscillations in the region of the primary rainbow can be determined semiclassically by using the results of Ford and Wheeler (Eqs. 14 and 15).

When nuclear symmetry is being considered, the analysis of the data is basically the same. However, with nuclear symmetry included the differential cross section has more structure since the possibility of charge exchange scattering must be taken into account. In order to better understand the source of the different oscillations which are present in the differential cross section with nuclear symmetry included, contributions from different combinations of scattering amplitudes, which are dominant in the data, will be examined separately.

In Figure 17 curve A is an illustration of the interference due to the $f_g(\theta)$ and $f_g(\pi - \theta)$ scattering amplitudes, and curve B shows the interference due to $f_u(\theta)$ and $f_u(\pi - \theta)$. Note that in the 90° scattering region both curve A and curve B exhibit high frequency oscillations. In this region it is obvious that the oscillations due to $f_g(\theta)$ and $f_g(\pi - \theta)$ have the greater amplitude and a higher frequency than those of $f_u(\theta)$ and $f_u(\pi - \theta)$. The important point here is to notice that the wavelength of either combination of scattering amplitudes in any angular region can be calculated by using the classical deflection functions and Equation 20. This is a useful method of determining which frequency is due to contributions from which branch of the respective deflection functions.

In order to make proper use of Equation 20 when nuclear symmetry is present, one must have a classical deflection function for charge exchange scattering. Even though one is not able to distinguish between direct scattering to angle θ or charge exchange scattering to angle $\pi - \theta$ when nuclear symmetry is present, the charge exchange scattering can be represented by a classical deflection function in a fashion similar to that of direct scattering. Recall from Chapter III,

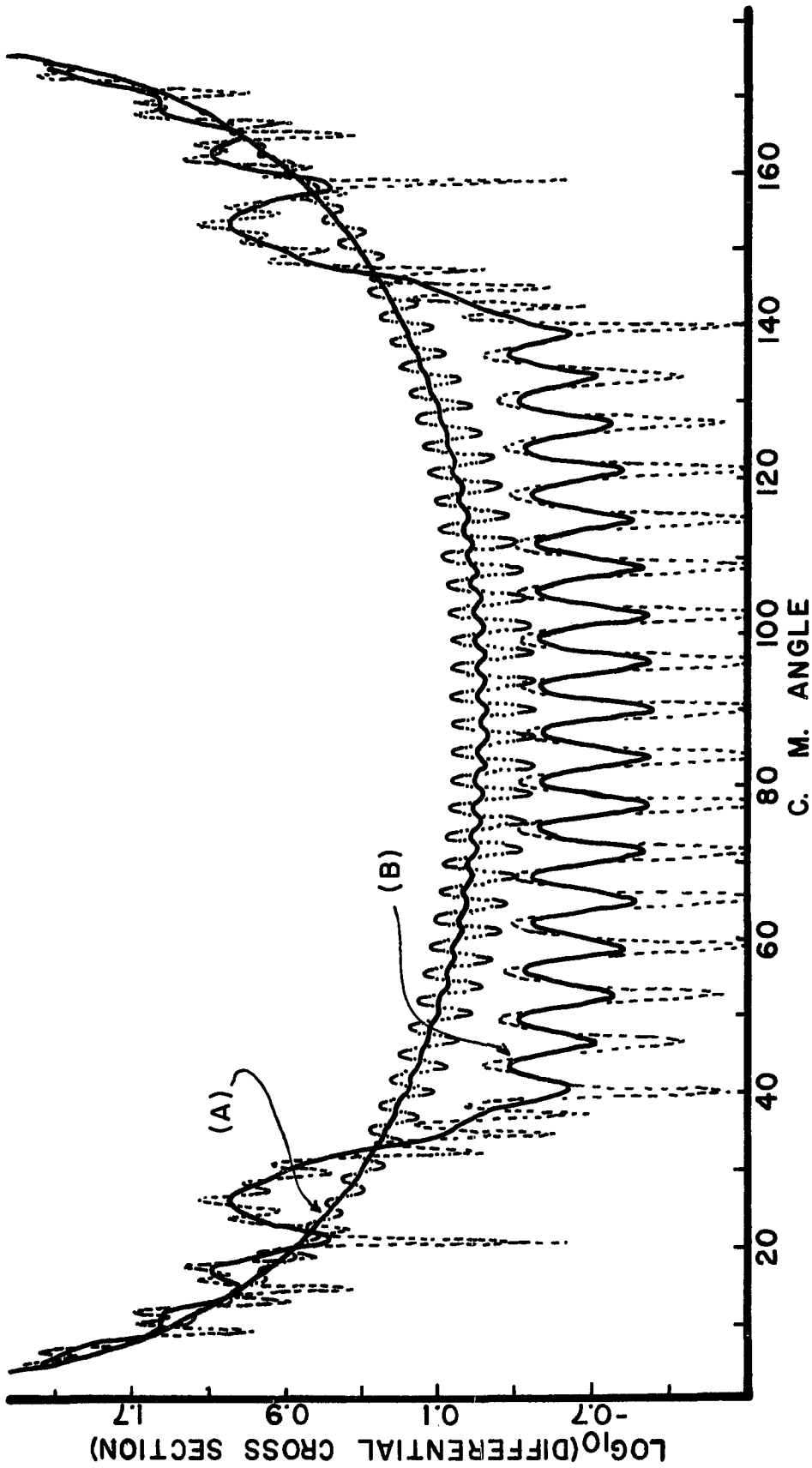


Figure 17. Contributions to the elastic differential cross section of ${}^3\text{He}^+ + {}^3\text{He}$, $E = 6$ eV with charge-exchange being considered. (A) Contributions from the gerade potential $|f_g(\theta) + f_g(\pi - \theta)|^2$. (B) Contribution from the ungerade potential $|f_u(\theta) + f_u(\pi - \theta)|^2$. Solid line is a convolution of the high frequency oscillations in both (A) and (B).

Section I-A that the angle of deflection and the classical deflection function are related by $\Theta = -\Phi$ for attractive scattering and $\Theta = +\Phi$ for repulsive scattering. In order to construct the corresponding deflection function for charge exchange scattering, let $\Phi_{\text{ex}} = \pi - \Phi$. The procedure is simple and it produces deflection functions which are representative of the charge exchange scattering. Figure 18 shows plots of the deflection functions for direct and charge exchange scattering.

In Figure 17A,B it is seen that ungerade scattering will dominate the cross section at small and very large angles while in the angular region between the observed rainbow angles (one at $\Theta = 25^\circ$ and one at $\Theta = 180^\circ - 25^\circ$) the gerade scattering is dominant. Figure 19 shows the combination of all four scattering amplitudes via Equation 19 for the ${}^3\text{He}^+ + {}^3\text{He}$ system at 6 eV collision energy. The high frequency oscillations seen in the post-rainbow region of the calculated differential cross section ($\Theta < \pi/2$) are due to direct and charge-exchange gerade interference, and the low frequency oscillations in this region are due to $f_u(\Theta)$ and $f_g(\Theta)$ interference. Both of these frequencies can be readily identified using the classical deflection functions in Figure 18 and Equation 20. For angles greater than 90° the

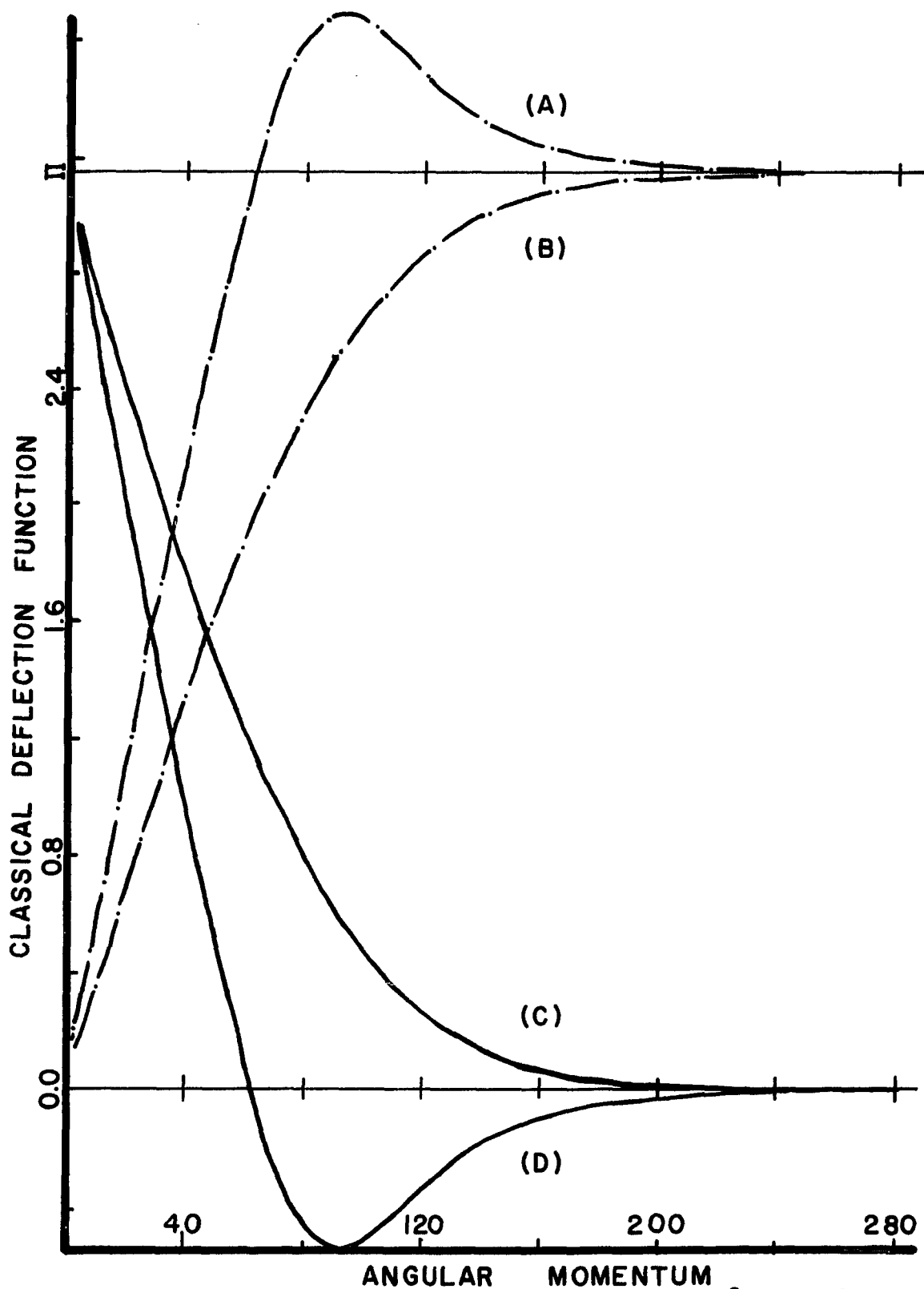


Figure 18. Classical deflection function for ${}^3\text{He}^+ + {}^3\text{He}$, $E = 6$ eV. (A) Ungerade charge-exchange scattering. (B) gerade charge-exchange scattering. (C) gerade direct scattering. (D) Ungerade direct scattering.

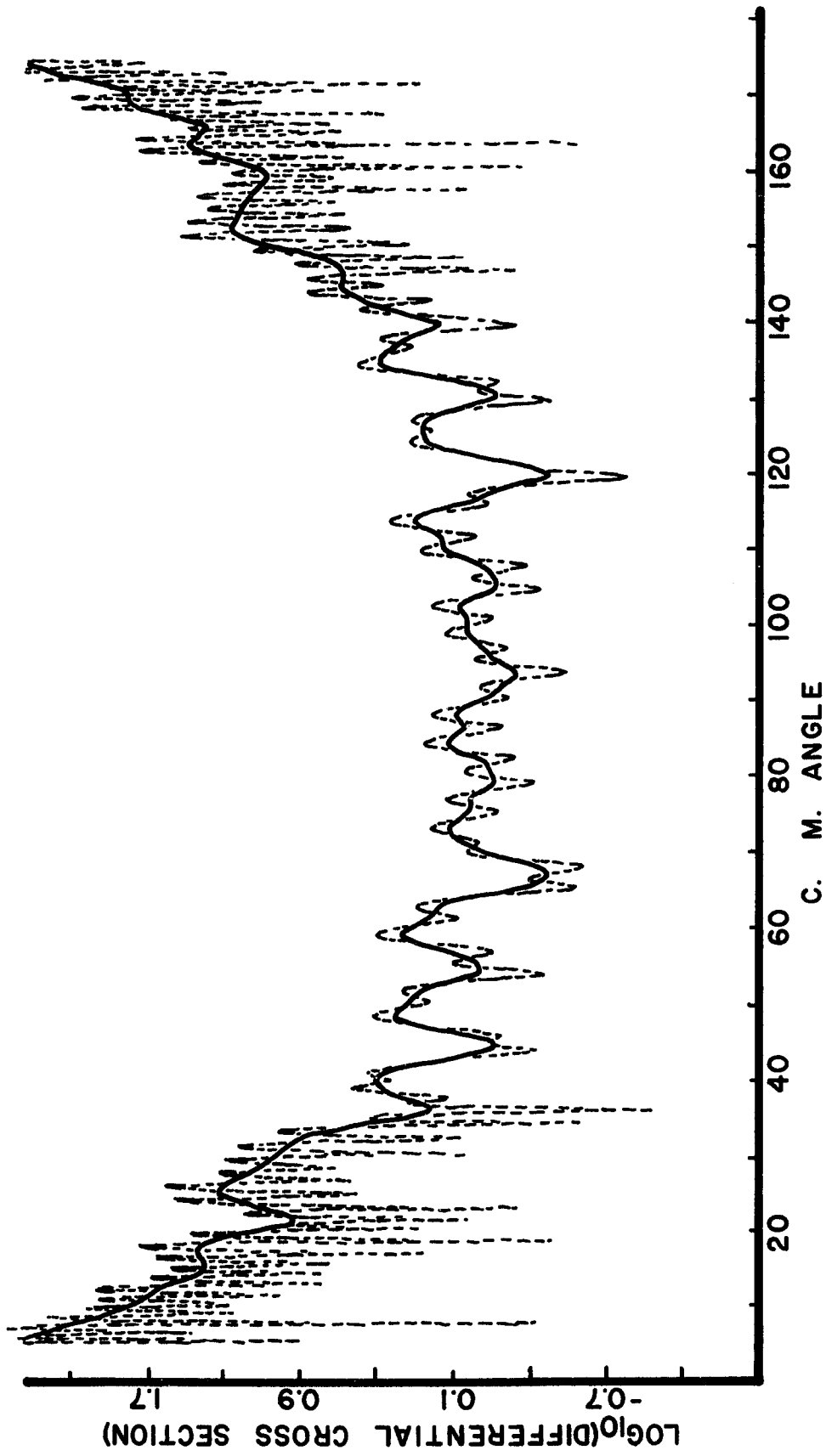


Figure 19. Complete elastic differential cross section for ${}^3\text{He}^+ + {}^3\text{He}$, $E = 6 \text{ eV}$. Different contributions to the differential cross section can be identified by comparison with Figures 15, 16, and 17.

explanation is the same except charge exchange scattering is dominant. In the case of no nuclear symmetry, the high frequency oscillations in the post rainbow region as well as the charge exchange interference for $\Theta > \pi/2$ are removed (see Fig. 16).

The classical deflection functions (Fig. 18) are a useful tool in unraveling the different oscillations seen in the differential cross sections. There is indeed a great deal of information which can be obtained from well resolved experimental data.

Section III. Application

A. ${}^3\text{He}^+ + {}^3\text{He}$

The 6 eV ${}^3\text{He}^+ + {}^3\text{He}$ experimental differential cross section shows the direct scattering rainbow in the region of 25° and the charge-exchange scattering rainbow in the region of 155° (see Fig. 20B). Even though the data at all angles are due to scattering from the two states (gerade and ungerade), the ungerade state is responsible for the structure observed in the rainbow and pre-rainbow region. There is some interference in the pre-rainbow region due to interference with the gerade state, but its effect is just to reduce the amplitude of the secondary rainbow oscillations rather than to add more structure to this region. On the other hand, the post-rainbow region (up to the charge-transfer rainbow seen at 155°) of the differential cross section is completely dominated by two-state interference. In this region for $\theta < \pi/2$ the interference between $f_g(\theta)$ and $f_u(\theta)$ is dominant. For $\theta > \pi/2$, the low frequency oscillations are due primarily to the interference of $f_g(\pi - \theta)$ and $f_u(\pi - \theta)$. In the 90° region (about 20° on each side of 90°) there are comparable contributions from all four scattering amplitudes involving direct and charge-transferred scattering. The high frequency

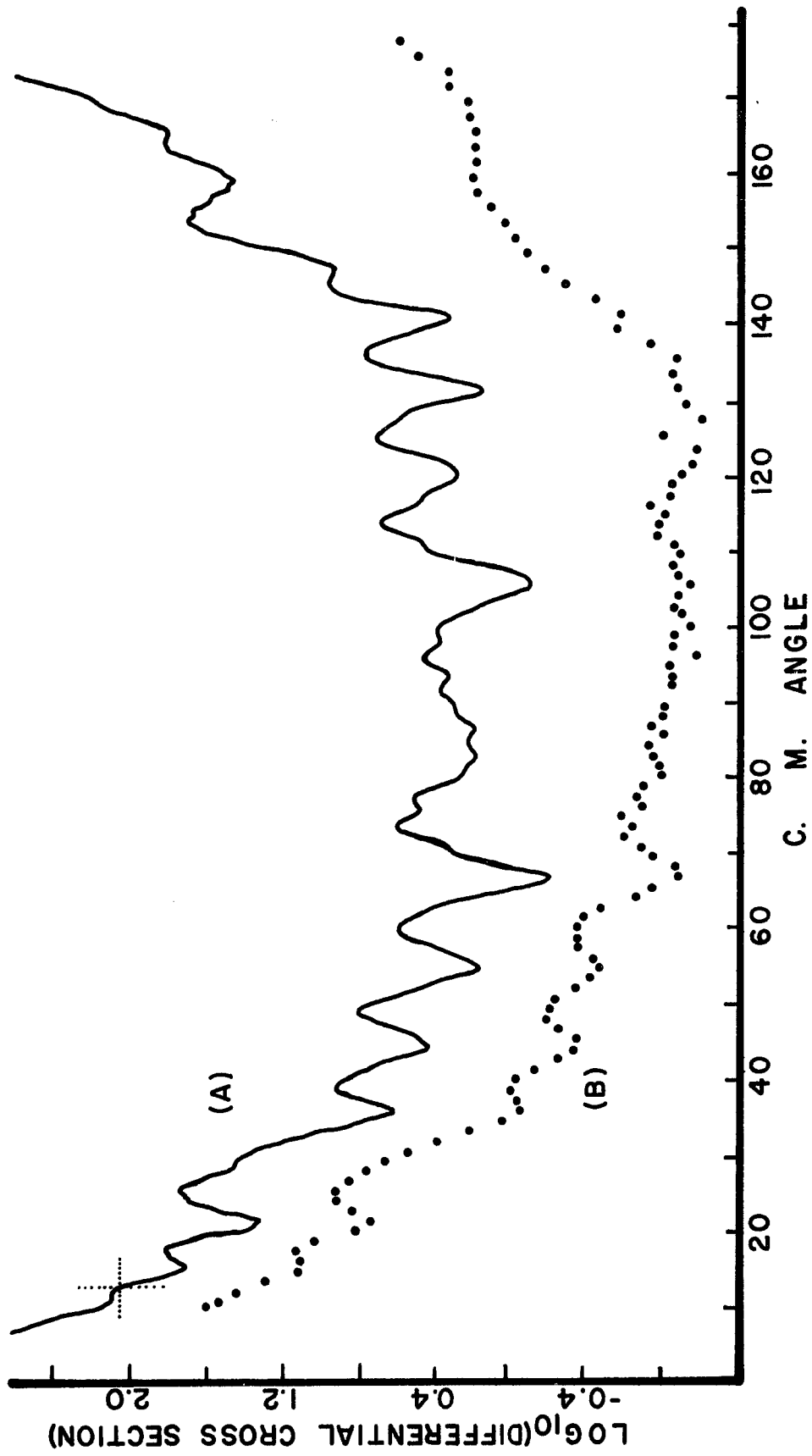


Figure 20. Elastic differential cross section for ${}^3\text{He}^+ + {}^3\text{He}$, $E = 6$ eV. (A) Remler-Regge calculated differential cross section. (B) Experiment. See Table III for value of calculation at indicator.

oscillations in the post-rainbow region, which are due to interference between the scattering amplitudes $f_g(\theta)$ and $f_g(\pi - \theta)$, were not completely resolved experimentally. There are other possible combinations of scattering amplitudes which give rise to fine oscillations in the same region, but their contribution is negligible in comparison with the amplitudes of the oscillations which are due to interference between $f_g(\theta)$ and $f_g(\pi - \theta)$.

In the simpler situation where nuclear symmetry is not present, as is the case for ${}^3\text{He}^+ + {}^4\text{He}$ or ${}^4\text{He}^+ + {}^3\text{He}$, then the only scattering amplitudes contributing to the differential cross section are $f_g(\theta)$ and $f_u(\theta)$. In this case only low frequency oscillations will be seen in the post-rainbow region (see Fig. 17), and there will be no increase in the scattering cross section in the region $\theta > \pi/2$. The lack of nuclear symmetry has no appreciable effect on the rainbow and pre-rainbow region.

It is necessary for one to proceed with care in the analysis of the scattering data for all the $\text{He}^+ + \text{He}$ systems. Even though the experiments reported here show more structure and cover a larger angular region than any data reported to date, the high frequency oscillations are not completely resolved in the pre- and post-rainbow regions of the differential cross section.

The lack of sufficient resolution in the pre-rainbow region is unfortunate since this is the scattering region which is most influenced by the region $r > r_m$ of the ungerade potential. As can be seen in Figure 22, the intermolecular potentials obtained for the ${}^3\text{He}^+ + {}^3\text{He}$ system are different in the region $r > r_m$. The lack of sufficient resolution of the high frequency oscillations in the post-rainbow region also limits the amount of information on the direct gerade and charge-exchanged gerade scattering.

In all calculations of the differential cross sections made on the homonuclear systems, the gerade state was assumed to be known. The contribution from the gerade potential to the differential cross section (via Eq. 17 or 19) was always included without any variation in $V_g(r)$. Variation in the differential cross section was achieved by iteration of the ungerade potential $V_u(r)$. In this manner the calculated differential cross section was brought into agreement with the data. As in Chapter III, Section I-A, two methods are employed to determine the ungerade potential. The first method is the inverted potential method and is the same as described in Chapter III, Section I-A. The parameters N , I , R , and l_0 are varied until there is agreement between the data and calculation in the rainbow and pre-rainbow regions. These parameters

are not considered to be extremely accurate as the fine oscillations in this region of the data are not resolved. To achieve agreement in the post rainbow region, the parameters h_1 and h_2 were varied (see Appendix A). In the immediate pre- and post-rainbow region, l_0 was the most important parameter to be varied. Figure 20 shows a plot of the ${}^3\text{He}^+ + {}^3\text{He}$ data and the calculated cross section which was calculated by the Remler-Regge method. Using the phase shifts retrieved from this calculation, the inverted potential was obtained and is shown in Figure 22A. The parameters used in the inversion calculation are listed in Table II.

No attempt has been made to insure agreement between data and calculation for $\theta > \pi/2$ due to the fact that the velocity of the scattered ions in the laboratory frame is approaching the thermal energy range. Detection of thermal energy ions is very difficult due to the influence of small electric and magnetic fields on their motion. In addition, it has been found that a very small parameter change will produce considerable change in the interference pattern in the 90° region. This is because all four scattering amplitudes ($f_g(\theta)$, $f_u(\theta)$, $f_g(\pi - \theta)$, $f_u(\pi - \theta)$) contribute to the structure in this region and slight changes in either

will result in a much greater change in the total structure. This behavior is very noticeable when several calculations are made in order to achieve agreement between calculation and experiment. It is gratifying, however, to see that the differential scattering cross section does increase in intensity in the region $\Theta > \pi/2$. At 155° it is possible to discern the charge-exchange rainbow.

The second method used to determine the ungerade potential is the potential-model calculation. The analytic form of the potential-model is that of Equation 16. Weise et al.³² have used this potential form to reproduce the rainbow and superimposed high frequency oscillations which they claim to have resolved in a 10 eV $^4\text{He}^+ + ^4\text{He}$ experiment. When their reported potential is used to calculate the differential cross section at 6 eV for $^3\text{He}^+ + ^3\text{He}$, the agreement is acceptable in the rainbow and pre-rainbow regions, but the post-rainbow oscillations are not in phase with the data. Using this available information as a starting point, the four parameters (G_1 , G_2 , r_m , and ϵ) are varied until satisfactory agreement is obtained between the data and calculation. The potential-model parameters which give a good fit to the data are shown

in Table II. Figure 21 shows a plot of the data and calculation for this potential-model potential. The resulting potential is shown in Figure 22A. The slight difference between these two curves illustrates that the two methods of calculation may respond somewhat differently to the same set of data. On the other hand, the difference may be due to noise that is inherent in either method of determining the intermolecular potential. Never-the-less, it is seen that the agreement between the two curves of Figure 22 is best for $1.4 a_0 < r < r_m$. As has been pointed out previously, this is just the region of $V(r)$ for which the low energy differential cross section is most sensitive.

In order to test the internal consistency of the S-matrix parameterization inversion scheme, the inverted $V(r)$ was fitted by an analytic form, and the differential cross section was calculated using the potential-model method. The result of this calculation is shown in Figure 23. As can be seen, the agreement between the calculation and experiment is very good for $\theta < \pi/2$. The lack of agreement in the 90° region is not considered to be significant, but rather is a function of how well the analytic function approximates the inverted potential.

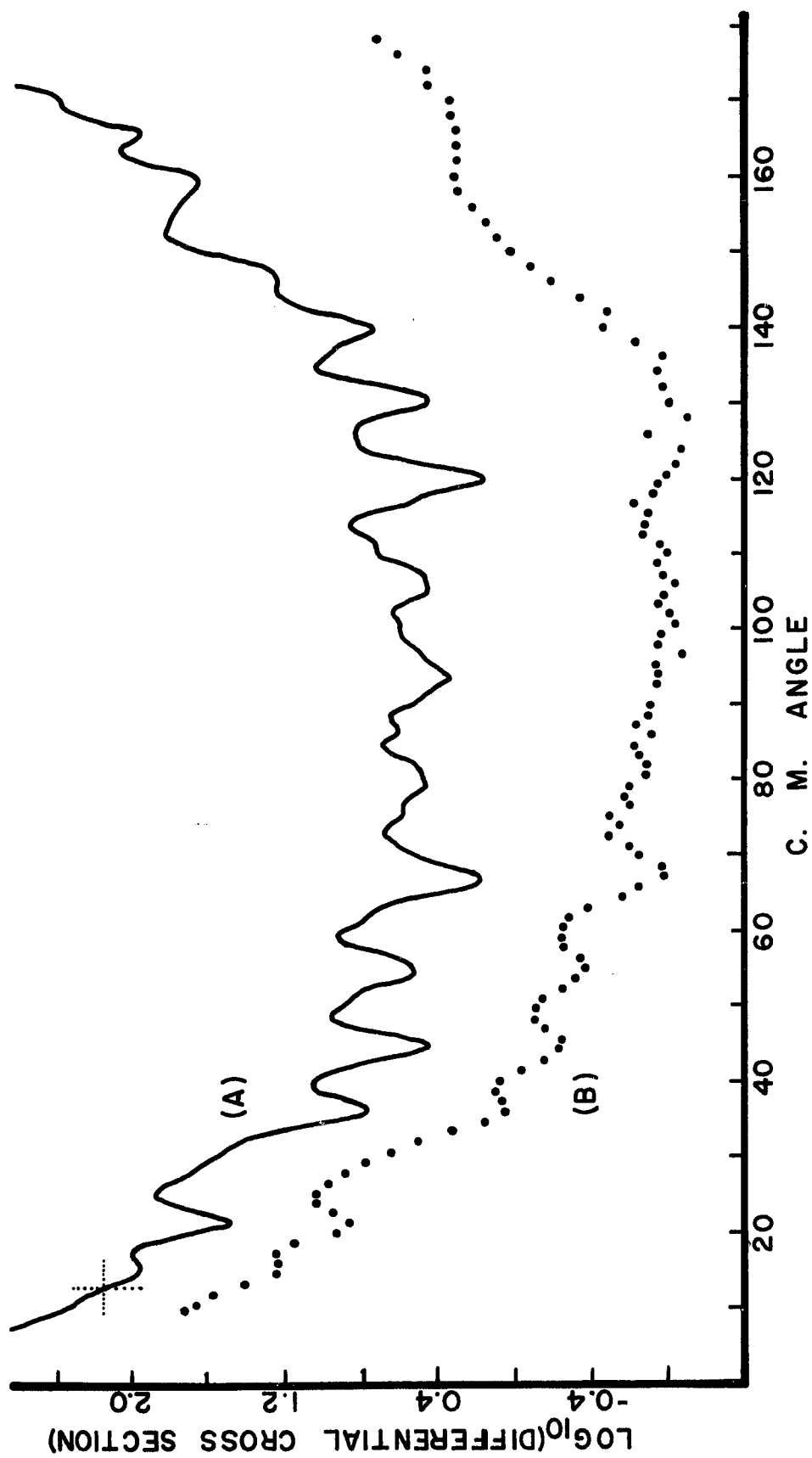


Figure 21. Elastic differential cross section for ${}^3\text{He}^+ + {}^3\text{He}$, $E = 6$ eV. (a) Potential-model calculation. (B) Experiment. See Table III for value of calculation at indicator.

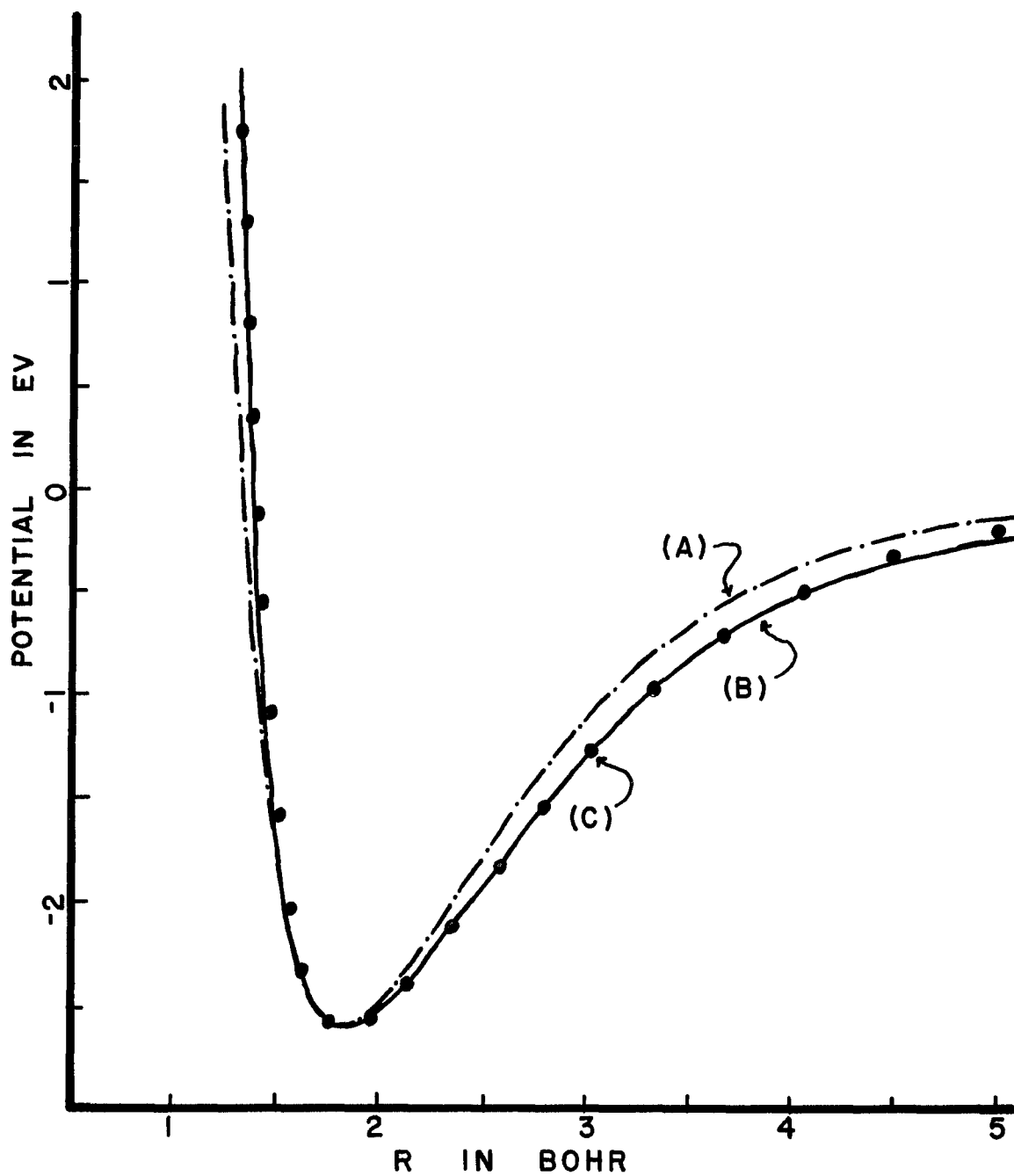


Figure 22. Intermolecular potentials retrieved from the experiment for ${}^3\text{He}^+ + {}^3\text{He}$, $E = 6$ eV. (A) Inverted potential ($r_m = 1.87a_0$, $\epsilon = -2.59$ eV). (B) Potential-model potential ($r_m = 1.80a_0$, $\epsilon = -2.60$ eV). (C) Analytic fit (potential-model type) to the inverted potential ($r_m = 1.80a_0$, $\epsilon = -2.60$ eV).

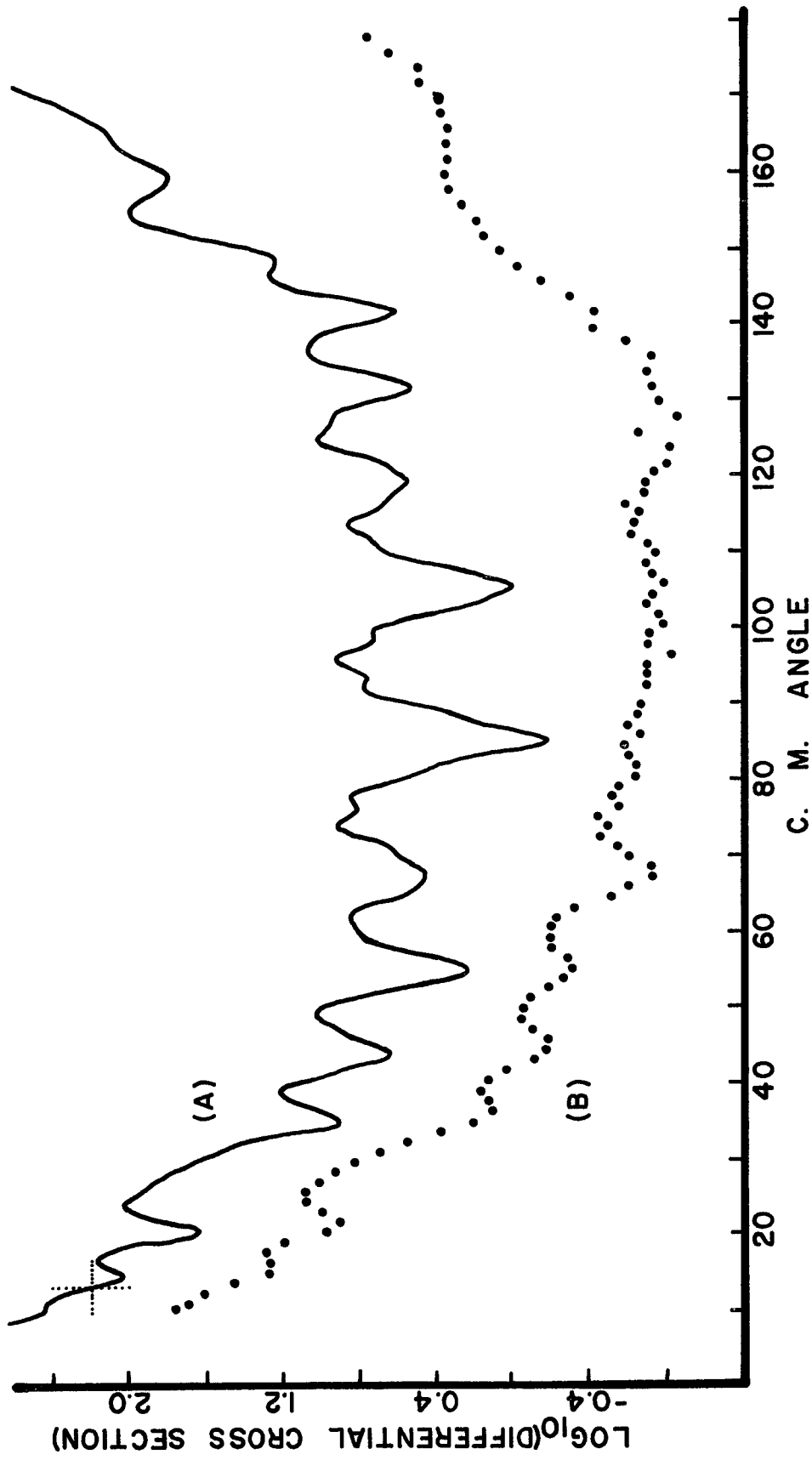


Figure 23. Elastic differential cross section for $^3\text{He}^+ + ^3\text{He}$, $E = 6 \text{ eV}$.
 (A) Second potential-model calculation of the differential cross section using an analytic fit to the inverted potential. See Table III for value of calculation at indicator. (B) Experiment.

Internal consistency is thought to be demonstrated without involving the computer time necessary to make a small parameter change (in G_2) in order to effect better agreement in the 90° region. The heavy circles shown in Figure 22 are points on the analytic-fit to the inverted potential which was used in the calculation.

The stated purity of the ^3He gas is $\geq 99.5\%$. Since the ^3He gas is extracted from tritium, any contamination that may be present is not due to ^4He .

B. $^4\text{He}^+ + ^4\text{He}$

The experimental differential elastic cross section for $^4\text{He}^+ + ^4\text{He}$ at 6 eV collision energy is shown in Figure 24. The basic structure observed in the data is the same as for the $^3\text{He}^+ + ^3\text{He}$ system. Only the inverted potential (i.e. S-matrix) calculation has been performed, and the parameters are given in Table II. To have made a potential-model calculation would not have added any information because the lack of fine structure resolution in the data prevents an accurate determination of the potential. Figure 25 shows the inverted potential which has been determined. The inverted potentials for both $^3\text{He}^+ + ^3\text{He}$ and $^4\text{He}^+ + ^4\text{He}$ have the same well depth. However, r_m for $^4\text{He}^+ + ^4\text{He}$ is 7% smaller than r_m for $^3\text{He}^+ + ^3\text{He}$.

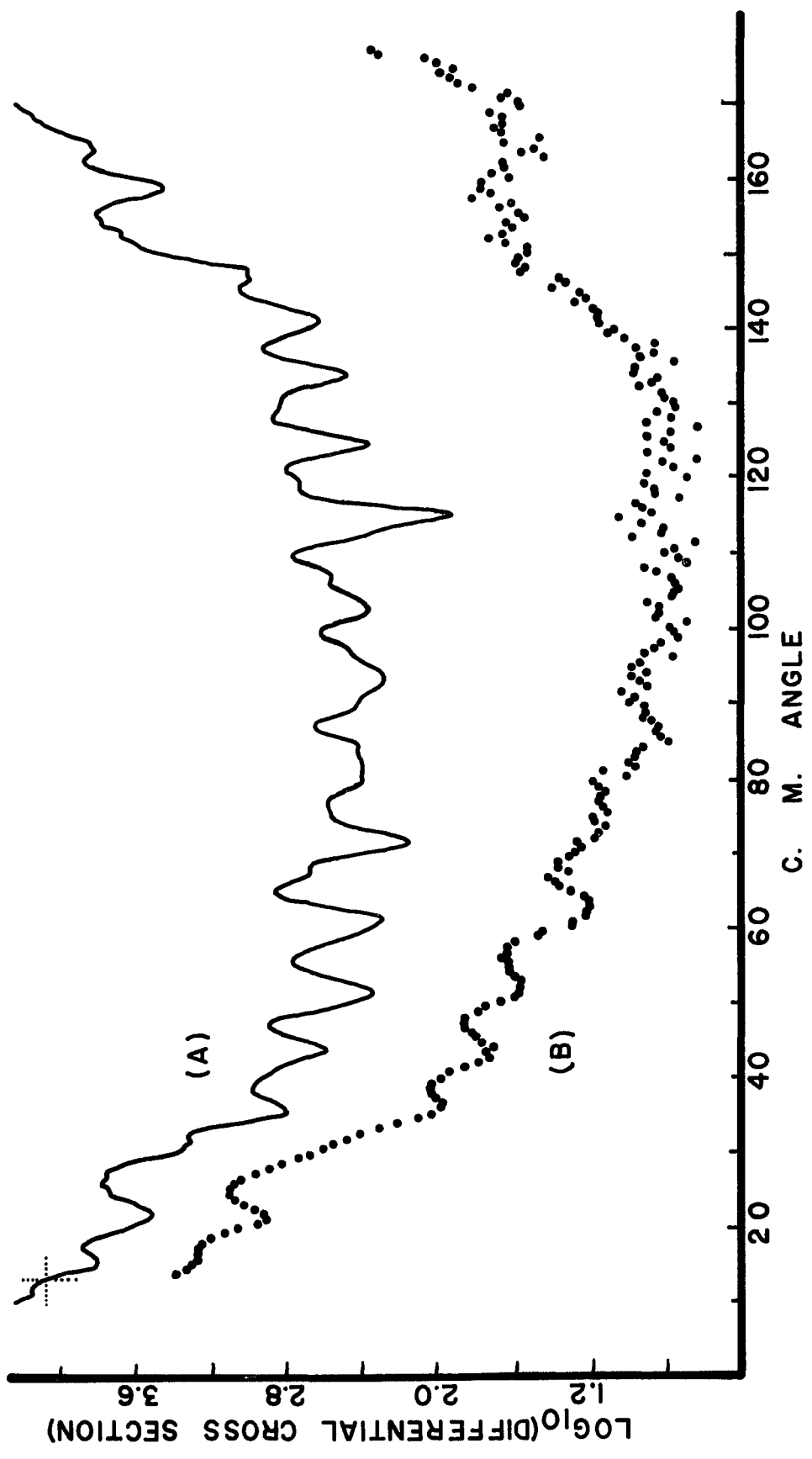


Figure 24. Elastic differential cross section for ${}^4\text{He}^+ + {}^4\text{He}$, $E = 6 \text{ eV}$.
(A) Inverted calculation of the differential cross section. (B) Experiment.
(See Table III for value of calculation at indicator.)

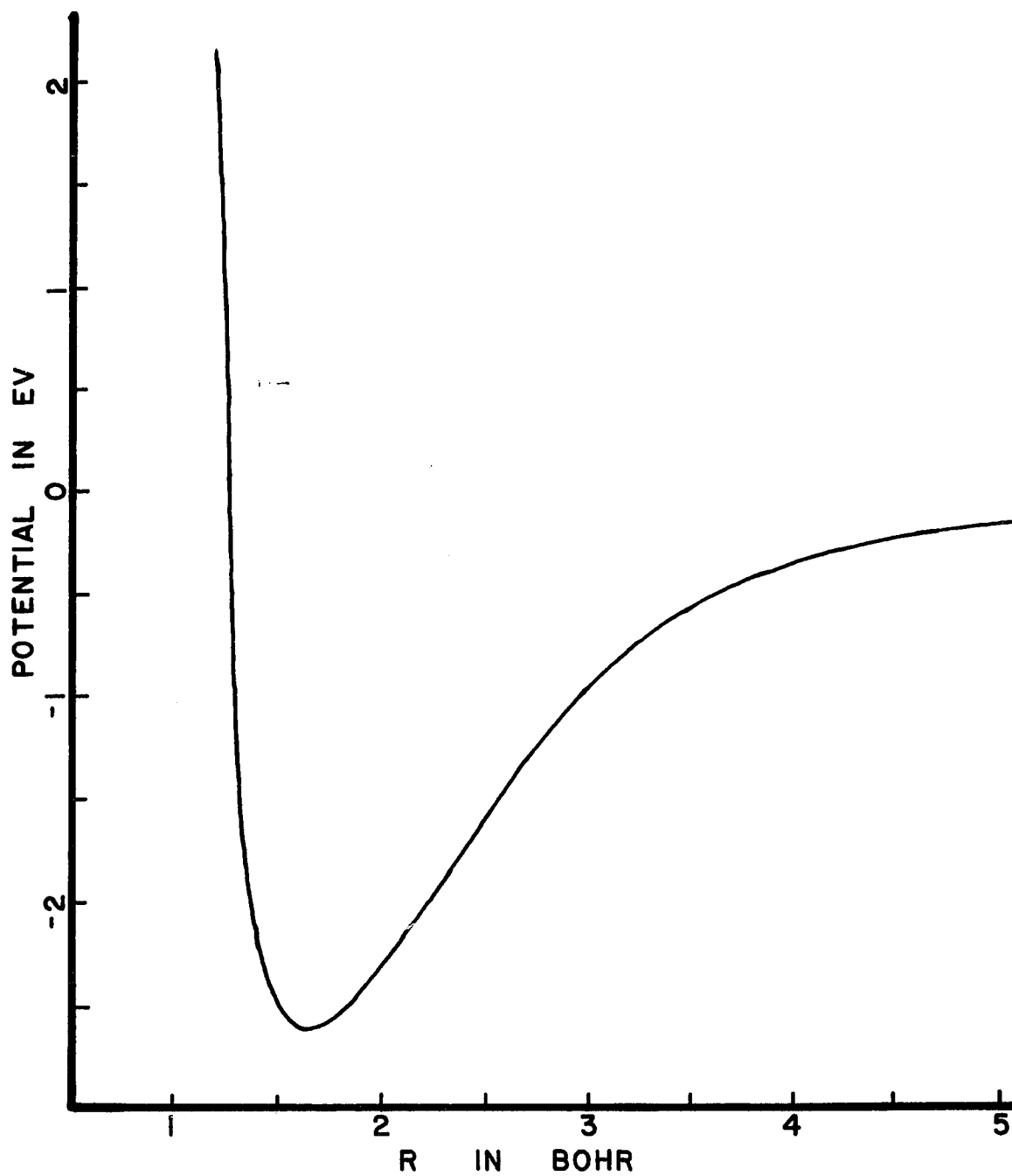


Figure 25. Inverted intermolecular potential retrieved from the data for ${}^4\text{He}^+ + {}^4\text{He}$, $E = 6$ eV. ($r_m = 1.67a_0$, $\epsilon = -2.6$ eV)

C. ${}^3\text{He}^+ + {}^4\text{He}$ or ${}^4\text{He}^+ + {}^3\text{He}$

The ${}^3\text{He}^+ + {}^4\text{He}$ system is very interesting for several reasons. The scattering process is identical in the center of mass to ${}^4\text{He}^+ + {}^3\text{He}$. Figure 26A,B shows the experimental differential cross sections for both systems at 6 eV collision energy. Even though the scattering is identical for both systems in the center of mass, the scattering angle for ${}^3\text{He}^+ + {}^4\text{He}$ is expanded in the laboratory frame when compared to ${}^4\text{He}^+ + {}^3\text{He}$ scattering. As a result it is possible to better resolve structure in the differential cross section of the ${}^3\text{He}^+ + {}^4\text{He}$ system. This improvement in resolution is very noticeable when comparing the two experimental differential cross sections in Figure 26.

Another point of interest is that nuclear symmetry is not present in these two systems. This can be seen in the data since there is no increase in the experimental differential cross section for $\theta > \pi/2$, as is the case when nuclear symmetry is present. When it is experimentally possible to distinguish between the nuclei (as is the case here), the scattering amplitudes $f_g(\pi - \theta)$ and $f_u(\pi - \theta)$ no longer enter into the scattering, and as a result the elastic differential cross section will not increase for $\theta > \pi/2$. In addition,

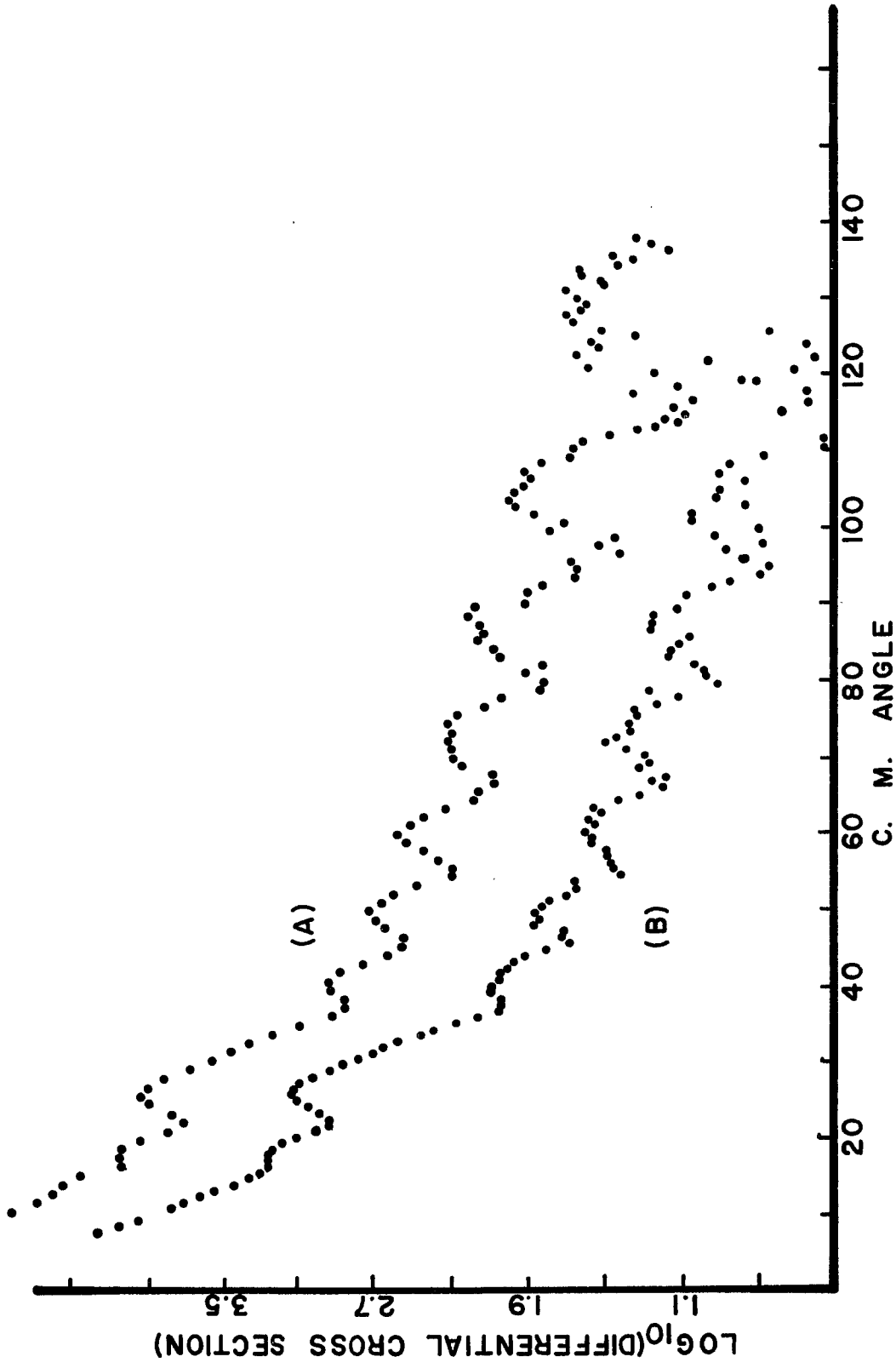


Figure 26. Experimental elastic differential cross sections for (A) ${}^3\text{He}^+ + 4\text{He}^+$ and (B) ${}^4\text{He}^+ + {}^3\text{He}^+$, $E = 6$ eV. Note the more distinct resolution of curve A.

the absence of these scattering amplitudes removes high frequency oscillations in the post-rainbow region and allows the two-state interference between $f_u(\theta)$ and $f_g(\theta)$ to be clearly resolved in the region around 90° . As a consequence it is possible to match the calculation and data up to angles of about 140° . For the systems with nuclear symmetry the additional scattering amplitudes limited the resolution to angles less than 90° .

The high frequency oscillations in the rainbow and pre-rainbow regions of the differential cross section are not resolved for the $^3\text{He}^+ + ^4\text{He}$ or $^4\text{He}^+ + ^3\text{He}$ system. However, the ability to resolve the post-rainbow two-state interference to angles greater than 90° has allowed a more detailed look at the method used to calculate the repulsive phase shifts necessary to reproduce the differential cross section and the ungerade potential.

The analytic function used to represent the repulsive branch of the classical deflection function is an adequate and convenient method for determining the repulsive phase shifts for the heteronuclear systems discussed in this work where the attractive scattering is dominant in the differential cross section. This same analytic function

is employed in the calculation of the repulsive phase shifts for the homonuclear systems. In this situation, however, the scattering is more sensitive to the repulsive phase shifts than is the case for the heteronuclear systems. This has allowed the repulsive phase shifts to be determined more accurately for the homonuclear systems. The initial estimates of the parameters for the repulsive phase shifts were easily inferred using Equation 20, and the agreement between the calculated differential cross section and experiment were quickly obtained.

With the present resolution of the oscillations in the post-rainbow region of ${}^3\text{He}^+ + {}^4\text{He}$, it should be possible to calculate the repulsive phase shifts by the appropriate parameterization of the S-matrix in the complex l -plane as has been done for the attractive phase shifts.⁷ This calculation has not been made.

Figure 27 shows the experimental differential elastic cross section for the ${}^3\text{He}^+ + {}^4\text{He}$ system and the corresponding inverted-potential calculation at 6 eV collision energy. The agreement is extremely good. Figure 28 shows a plot of the inverted ungerade potential for ${}^3\text{He}^+ + {}^4\text{He}$ and for ${}^4\text{He}^+ + {}^3\text{He}$. The resolution of the large number of oscillations in the post-rainbow region of the experimental differential cross section has allowed

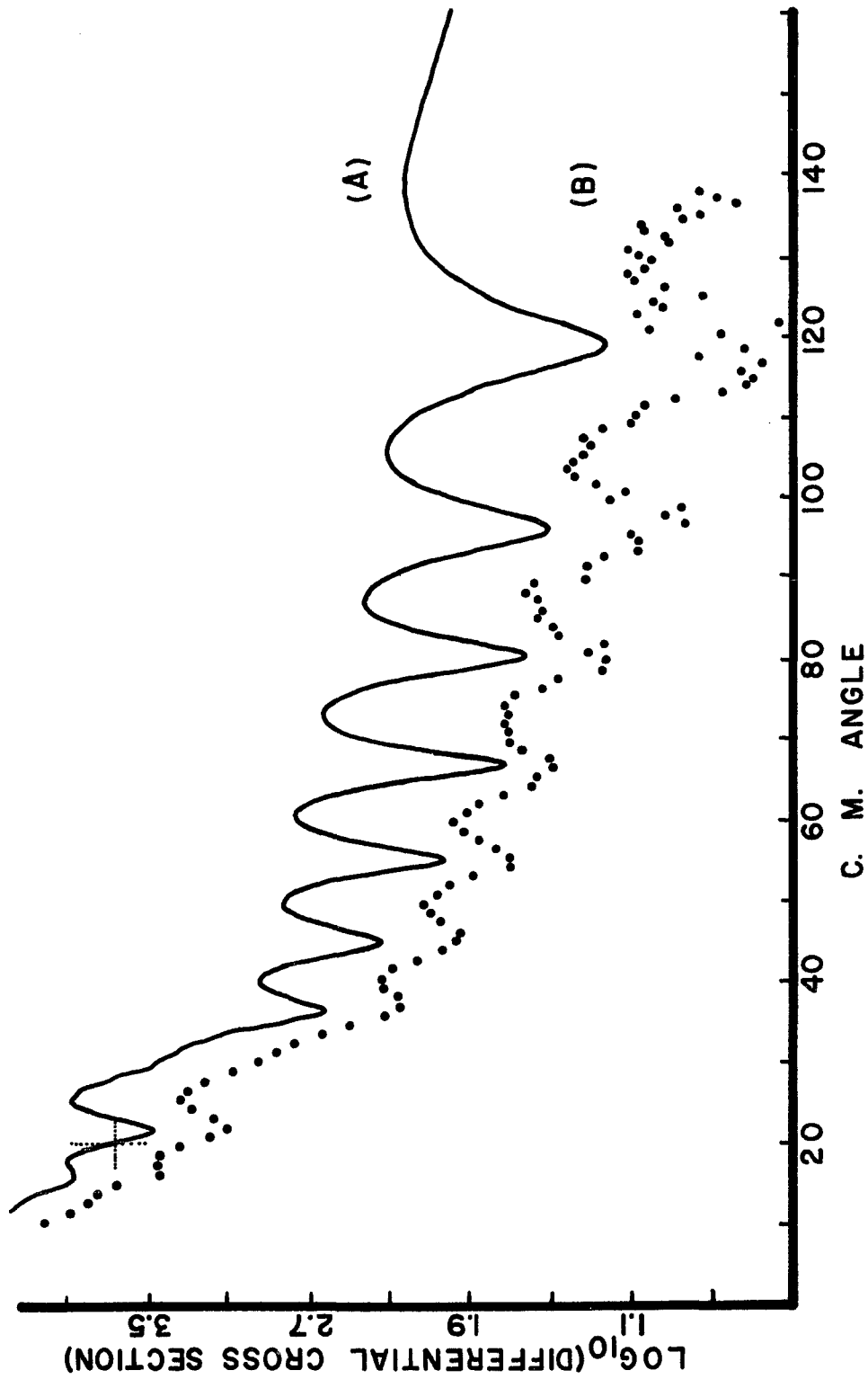


Figure 27. Elastic differential cross section for ${}^3\text{He}^+ + {}^4\text{He}$, $E = 6 \text{ eV}$.
 (A) Inverted calculation of the differential cross section. (B) Experiment.
 Note that the resolution of the two-state interference is observed to $\sim 140^\circ$.
 See Table III for value of calculation at indicator.

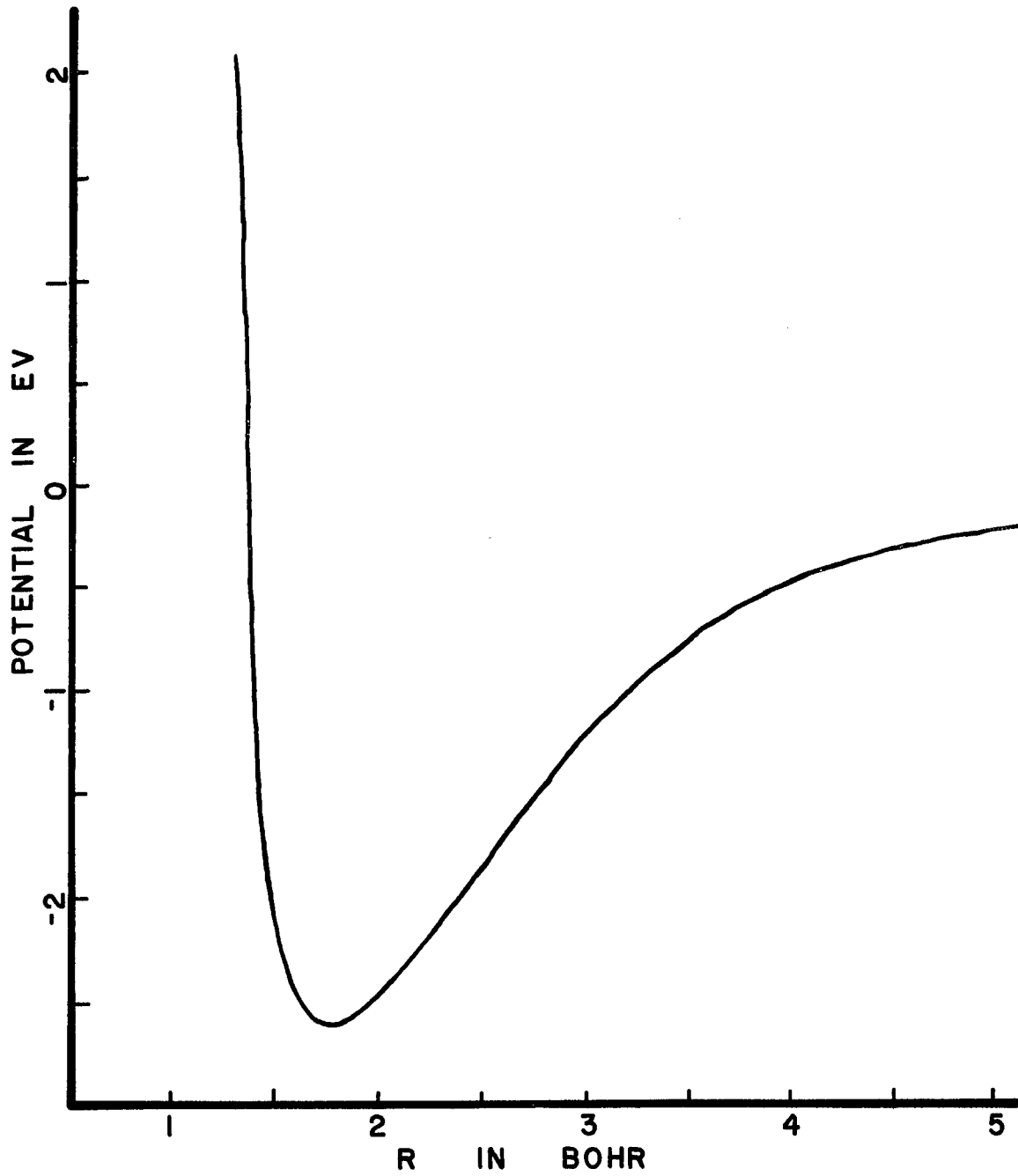


Figure 28. Inverted intermolecular potential for $3\text{He}^+ + 4\text{He}$ or $4\text{He}^+ + 3\text{He}$, $E = 6$ eV. ($r_m = 1.80a_0$, $\epsilon = -2.60$ eV)

a sensitive determination of the repulsive branch of the potential. No potential-model calculation is presented due to lack of resolution of the high frequency oscillations in the rainbow and pre-rainbow region of the data.

Section IV. Conclusion

The experimental resolution in the $\text{He}^+ + \text{He}$ systems reported here is better than any reported to date, and the potential (ungerade) reported is believed to be the most accurate. Due to the lack of resolution of the high frequency oscillations in the rainbow and pre-rainbow regions of the differential cross section, there is more uncertainty in the intermolecular potential in the region $r > r_m$ than in the region $r < r_m$. If these high frequency oscillations had been resolved, it would have been possible to determine with considerable accuracy the ungerade intermolecular potential in the region of the potential well (assuming the gerade potential used in the calculation to be accurate).

The nuclear symmetry effects are easily observed by comparing the $^3\text{He}^+ + ^4\text{He}$ or $^4\text{He}^+ + ^3\text{He}$ experiments with the $^3\text{He}^+ + ^3\text{He}$ or $^4\text{He}^+ + ^4\text{He}$ experiments. Other laboratories³⁶ have observed the high frequency oscillations in the post-rainbow region (at higher energies) which are due to nuclear symmetry, but the experiments presented in this work are the first to be reported in which the symmetry effects in the region $\theta > 90^\circ$ are shown.

The parameters most often used for comparison of theoretical calculations with experiment are r_m and ϵ . In the work presented here it has been established that these two parameters are of secondary importance in determining the structure observed in the low-energy differential cross sections.

Gilbert and Wahl³⁷ note that the experimentally determined well depth for the ungerade potential increases as the energy of the experiment is decreased. That is, experiments⁹ with collision energies of 50, 15, and 10 eV (for ${}^4\text{He}^+ + {}^4\text{He}$ scattering) have corresponding well depths of 2.22, 2.34, and 2.49 eV. These well depths were calculated via potential-model calculations which were made by the authors reporting the experiments. Gilbert and Wahl believe the well depth value corresponding to the lowest collision energy to be the most accurate. From their ab initio calculations (calculated in the molecular-orbital, self-consistent-field approximation), they report a well depth of 2.67 eV at $r_m = 2.0a_0$. In the inverted potential calculation from this experimental work, a well depth of 2.60 eV at $r_m = 1.8a_0$ for ${}^3\text{He}^+ + {}^3\text{He}$ is obtained.

The use of different isotopes of Helium at the same collision energy has allowed a check on the procedures

used to determine the intermolecular potential for $\text{He}^+ + \text{He}$ scattering. A single intermolecular potential should indeed describe all the scattering observed regardless of the isotopes involved. Figure 29 is a plot of the inverted potentials for all four possible combinations of Helium which are investigated in this work. The ${}^4\text{He}^+ + {}^4\text{He}$ inverted potential is thought to be the least accurate due to unfavorable source conditions at the time of the experiment. The ${}^3\text{He}^+ + {}^4\text{He}$ inverted potential is believed to be quite accurate in the region $r < r_m$. This is the result of being able to clearly resolve the experimental differential cross section through scattering angles greater than 90° . The ${}^3\text{He}^+ + {}^4\text{He}$ potential should be the most representative of the true intermolecular potential for $\text{He}^+ + \text{He}$ scattering. In the region $r > r_m$, the ${}^3\text{He}^+ + {}^4\text{He}$ and ${}^3\text{He}^+ + {}^3\text{He}$ potentials agree to within 4%. Due to the lack of resolution of the fine oscillations in the experiment, the difference between the three potentials shown in Figure 29 can not be considered experimentally meaningful.

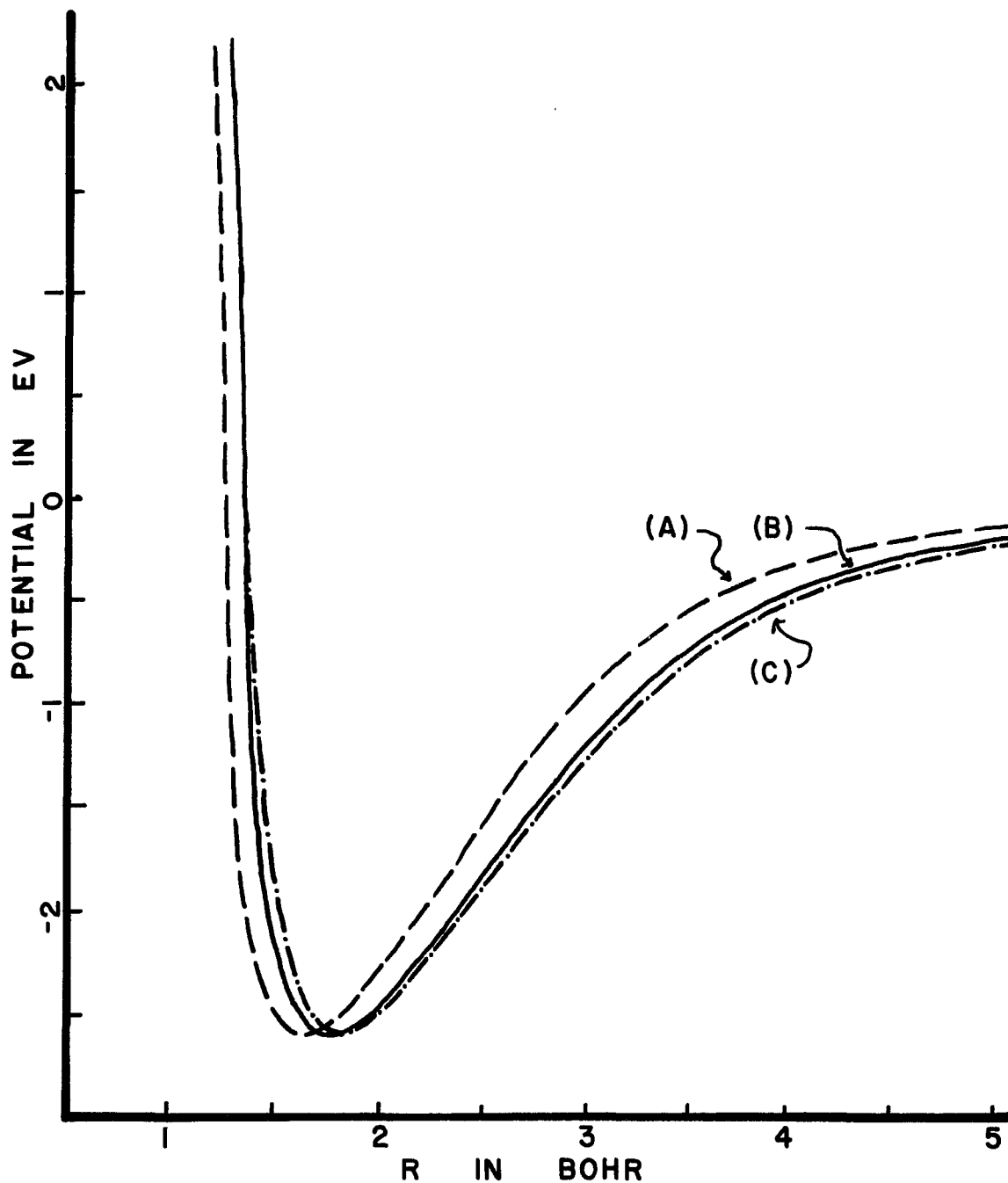


Figure 29. Comparison of the inverted intermolecular potentials for all the $\text{He}^+ + \text{He}$ systems, $E = 6$ eV. (A) ${}^4\text{He}^+ + {}^4\text{He}$, $r_m = 1.67a_0$, $\epsilon = -2.60$ eV. (B) ${}^3\text{He}^+ + {}^4\text{He}$ or ${}^4\text{He}^+ + {}^3\text{He}$, $r_m = 1.80a_0$, $\epsilon = -2.60$ eV. (C) ${}^3\text{He}^+ + {}^3\text{He}$, $r_m = 1.87a_0$, $\epsilon = -2.59$ eV.

Section V.

Error

Any error which has accrued during the acquisition of the data presented in this work is due to the experimental uncertainty in the determination of three quantities. These three are the measurement of the collision energy, the measurement of the angle of deflection, and the measurement of the scattering intensity (corrected for apparatus geometry). Each will be discussed and the error associated with each will be given.

All of the experiments reported herein are 6 eV collision energy or less. In a typical experiment the full width at half maximum for the energy spread of the primary beam is about .3 eV before entering the collision region. The energy selector which is used to analyze the primary beam (or scattered ions) after it (they) has (have) passed through the scattering region has a passband (FWHM) of about 2%. This gives a full-width at half maximum in the energy transmitted of about .1 eV for a 6 eV primary beam. Therefore it is reasonable to assume that the energy of the primary beam is known to $\pm .05$ eV. Taking into account the thermal energy of the target gas, the uncertainty in energy of the scattered ions should

not be more than $\pm .07$ eV. As a result, the collision energy is believed to be known to 1%. Other sources which could contribute to the uncertainty in the energy are contact potentials, but these are thought to be small (i.e. in the millivolt range).

The measurement of the angle of deflection of the scattered ions is precisely done with a slide-wire mechanism. From simple slit geometry, the velocity selector can accept ions scattered into an angular region slightly less than $1/3$ of a degree. Checks have been made and the structure observed in the data is reproducible to within $1/3$ of a degree. Thus the uncertainty in the angular position of the scattered ions is thought to be known to better than $\pm 1/4$ of a degree. The calculated differential cross sections can be fitted to the data to a high degree of accuracy in angular location of the oscillations. In fact, a variation in the inverted calculation of the parameters N , R , or I in the heteronuclear systems or the parameters h_0 , h_1 or h_2 in the homonuclear systems of 1% can be readily observed.

The statistical error in the intensity of the scattered particles at angle θ is proportional to the square root of the number of particles scattered to

that angle. Since the data is a relative differential cross section, the intensity of a peak is not as important in the analysis as is how well the peak is resolved. The typical range in the intensity of the data is from about 20,000 counts per sec to less than 12 counts per sec. In much of the data the structure in the 12 count region is well resolved and reproducible. Even though there is statistical variation in the intensity on the order of 10%, the location of the structure is reproducible to much better accuracy than 10% (i.e. to 1/4 of a degree as discussed).

Even though the general, over-all slope was not explicitly used in fitting the calculated differential cross section to the experimental results, it does merit discussion. When considering the general slope of the data, systematic errors are probably more important than random errors in contributing to the decay. This can be seen by comparing two different experiments. Figure 20 shows the ${}^3\text{He}^+ + {}^3\text{He}$ differential cross section where the experimental conditions are thought to be optimum. Normalizing the calculation and experiment at the rainbow angle, the calculation is only 7% greater than the data in the 90° region. On the other hand, in Figure 24 (${}^4\text{He}^+ + {}^4\text{He}$) where systematic errors are known

to exist, the calculation is about 600% above the data in the 90° region. An amplitude difference as large as 600%, however, does not affect the location of the observed structure in the data. As a result, systematic errors were not considered when matching calculations to experiments. The primary contributions to systematic errors are the changing conditions in the beam source. During an experiment which requires from three to four hours to perform, it is possible for several source parameters to vary which could in turn change the intensity of the primary beam.

In summary, the following experimental quantities are known to within the stated percentages: collision energy to 1%, angle of scatter to $\pm 1/4^\circ$, differential scattered intensity to $(\text{\#counts per unit})^{1/2}$, and the general slope of the heteronuclear systems to 5% (normalized at smallest angle possible).

The purpose of these experiments is to retrieve the intermolecular potential which governs the interaction between the reactants. How accurately this has been done for the Homonuclear systems can be estimated by looking at Figures 22 and 29. Figure 22 is the result of making three calculations on the same system. Figure 29 is the result of making the same calculation on three

isotopically different but electronically similar systems. The percentage difference in r or in ϵ for any two curves seen in the figures is very dependent upon the position along the curves chosen for comparison. As a result of this, no numbers representing percent differences are given. These potentials on the $\text{He}^+ + \text{He}$ systems are believed to be as accurate as can be determined without resolution of the fine oscillations in the experimental differential cross section. The accuracy of the intermolecular potential for the heteronuclear systems (where the fine oscillations are resolved experimentally) is thought to be within the experimental accuracy of the apparatus.

TABLE II

PARAMETERS

	POTENTIAL-MODEL			REMLER-REGGE					r_m (a_0)	ϵ (eV)		
	G_1	G_2	G_1G_2	N	R	I	o	h_1			h_2	
${}^3\text{He}^+ + {}^3\text{He}$												
Potential Model	2.7	1.0	.798	2.155						1.8	2.6	
*Potential Model	3.15	1.0	.587	1.85						1.8	2.6	
Mittmann ^a	3.8	1.0	1.8	4.10						1.98	2.55	
Inverted					10	98	37.7	62	1.57	.785	1.87	2.59
Ab Initio ^b (Liu)										2.04	2.47	
${}^3\text{He}^+ + {}^4\text{He}$ OR ${}^4\text{He}^+ + {}^3\text{He}$					10	104	37.7	64	1.5	.95	1.8	2.6
${}^4\text{He}^+ + {}^4\text{He}$					10	104	37.7	64	1.5	.95	1.67	2.6

*Analytic fit to inverted potential.

a. Mittmann, H. U., et al., Zeitschrift Fur Naturforschung, 26a, 1112 (1971). b. Liu, B., Phys. Rev. Letters 27, 1251 (1971). G_1 and G_2 are parameters in the Morse potential used in P-M calculations. N, R, I, o, h_1 , & h_2 are parameters used in inversion calculations (Remler-Regge).

TABLE III

ABSOLUTE VALUES FOR DIFFERENTIAL
CROSS SECTION CALCULATIONS

Figure*	Curve	Angle (degree CM)	$\text{Log}_{10} \sigma(\theta)$ ($a_0^2/\text{steradian}$)
6	B	7.30	2.16
	C	7.25	2.00
8	B	7.25	2.00
11	B	10.25	1.93
	C	9.75	2.00
13	B	8.75	2.00
20	A	12.50	1.70
21	A	13.00	1.60
23	A	13.00	1.60
24	A	13.25	1.59
27	A	20.50	1.15

*The ordinate axes of the figures listed here only indicate the relative differential cross section. In order to ascertain the absolute values for the calculated differential cross section, each curve can be adjusted with the use of this table. The indicator on each curve in the respective figure marks the ordinate and abscissa values listed in the above table.

APPENDIX A

REPULSIVE PHASE SHIFTS

The repulsive phase shifts used in a Remler-Regge calculation are obtained by making use of the semi-classical equivalence relationship $\Theta(\ell) = 2\mathcal{N}(\ell)/d\ell$. Through the use of this relationship, it is possible to calculate the repulsive phase shifts using an analytic function for the repulsive branch of the classical deflection function. As a result it is convenient to use the classical deflection function in this discussion.

The function used to represent the repulsive branch of the classical deflection function has the following properties: (a) It fits smoothly with the poles contribution to the deflection function in the region of ℓ_R (ℓ_R being the position in ℓ of the rainbow angle \mathcal{O}_R on the deflection function). (b) The function and its first derivative are smooth and continuous in the region of ℓ_R . (c) At $\ell = \ell_0$, the function = 0 (ℓ_0 being an external parameter which is variable). (d) It goes smoothly to π at $\ell = 0$. (e) At position $(3/4)\ell_0$, the value of the

function is adjustable (this is the external parameter h_1).

(f) At position $l_0/2$ the value of the function is adjustable (this is the external parameter h_2). The range of values which l_0 , h_1 , and h_2 can take is considerable, but they must be chosen within reasonable limits. If the range of values is violated, the computer program will so indicate.

The total classical deflection function can be thought of as the sum of the poles contribution (contributing the attractive phase shifts) and the contribution from an analytic function representing the repulsive phase shifts.

$$\Theta_{\text{Total}}(l) = \Theta_p(l) + \Theta_{\text{core}}(l)$$

Where $\Theta_p(l) = \text{poles contribution}$

For $l \leq l_R$

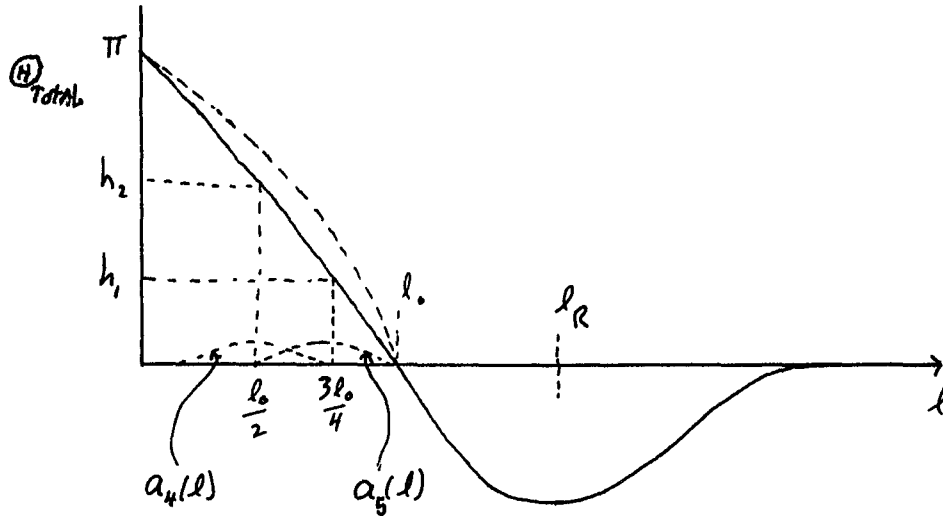
$$\Theta_{\text{core}}(l) = a_1(l) \cdot a_2(l) + a_4(l) + a_5(l) - \Theta_R - \Theta_p(l)$$

For $l > l_R$

$$\Theta_{\text{core}}(l) = 0$$

Of the five terms in $\Theta_{\text{core}}(l)$ the first is the most complicated and will be discussed last. $\Theta_p(l)$ is determined from Equation 8, and Θ_R is known from the poles contribution (i.e. $\Theta_R \approx 2N/I$ where $N = \# \text{ poles}$, $I = \text{Im } \lambda_p$ being the position of the poles in the complex l -plane). The second and third term are related to parameters h_1 and h_2 and allow some variation in the

shape of the deflection function between l_0 and π . That is, h_1 and h_2 are the value of $\Phi_{\text{Total}}(l)$ at positions $l = (3/4)l_0$ and $l = l_0/2$ respectively.



For $l \leq l_0$

$$a_4(l) = 1 - C_4 \cos\left(\frac{2\pi l}{l_0}\right)$$

For $l > l_0$

$$a_4(l) = 0$$

For $\frac{l_0}{2} \leq l \leq l_0$

$$a_5(l) = 1 - C_5 \cos\left(\frac{4\pi l}{l_0}\right)$$

For $l > l_0$ and $l < \frac{l_0}{2}$

$$a_5(l) = 0$$

where $C_4 = h_2\left(\frac{l_0}{2}\right) + \Phi_R - 1 - a_1\left(\frac{l_0}{2}\right) \cdot a_2\left(\frac{l_0}{2}\right)$

$$C_5 = h_1\left(\frac{3l_0}{4}\right) + \Phi_R - 2 - a_1\left(\frac{3l_0}{4}\right) \cdot a_2\left(\frac{3l_0}{4}\right)$$

Values for $a_1(l)$ and $a_2(l)$ must be found before C_4 and C_5 can be evaluated.

The evaluation of the first term of $\oplus_{\text{core}}(l)$ is now in order. Graphs will be used to illustrate the effect of $a_1(l)$ and $a_2(l)$ in the different regions of interest.

For all l

$$a_1(l) = (\pi + \theta_R) \cdot (C, l + 1)$$

For $l_1 \leq l \leq l_R$

$$a_2(l) = \frac{1}{2} \{1 + \cos[\omega(l + l_R) - \pi]\}$$

For $l < l_1$

$$a_2(l) = 1$$

CASE I

$$l_1 = l_R - \frac{\pi}{\omega}$$

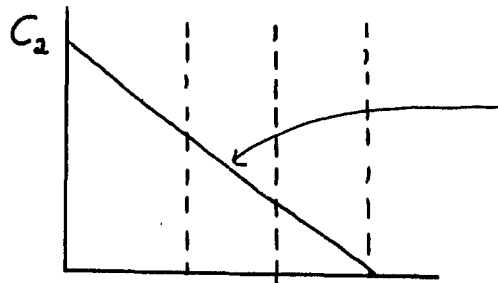
$$\text{If } \frac{l_0}{l_R} < \frac{\pi}{\pi + \theta_R} \quad \text{Then } C_1 = -\frac{l}{l_R} \text{ and}$$

ω is the root of

$$\frac{1}{2} \left(1 - \frac{l_0}{l_R}\right) (\pi + \theta_R) \{1 + \cos[\omega(l_0 - l_R) - \pi]\} - \theta_R = 0,$$

Otherwise branch to CASE II.

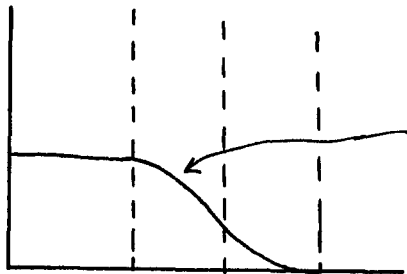
case I cont...



$$a_1(l) = C_1(l) + C_2$$

$$C_2 = \pi + \theta_R$$

$$C_1 = -\frac{1}{l_R}(\pi + \theta_R)$$

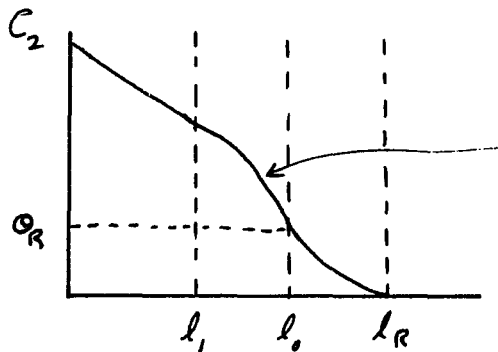


$$\text{for } l < l_1$$

$$a_2(l) = 1$$

$$\text{for } l \geq l_1$$

$$a_2(l) = \frac{1}{2} \{ 1 + \cos[\omega(l - l_R) + \pi] \}$$



$$a_1(l) \cdot a_2(l)$$

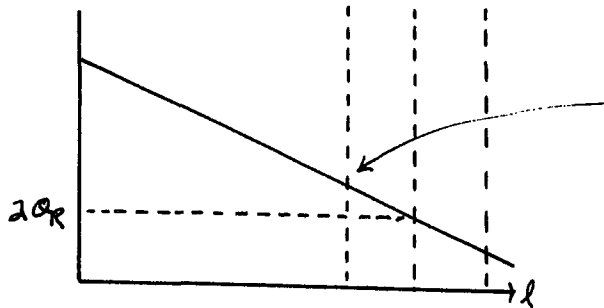
Case I is the situation most often encountered in calculations. However if l_R is too large for a smooth matching of $\Theta_p(l)$ and $\Theta_{\text{core}}(l)$ at l_0 , then the program will branch to Case II. The condition for branching to Case II is $C_1 l_0 + C_2 < \theta_R$.

CASE II

$$l_1 = 2l_0 - l_R$$

when $\frac{l_0}{l_R} > \frac{\pi}{\pi + \theta_R}$

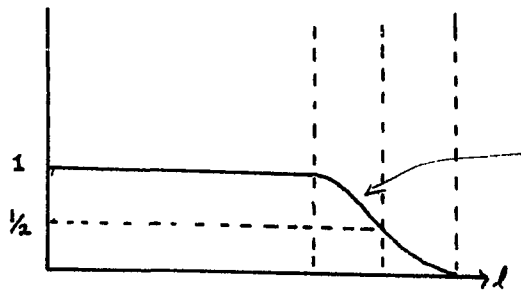
Then $\omega = \frac{\pi}{2} \left(\frac{1}{l_R - l_0} \right)$ and $C_1 = -\frac{1}{l_0}$



$$a_1(l) = A_1 l + A_2$$

$$A_2 = C_2 = \pi + \theta_R$$

$$A_1 = -\frac{1}{l_0} (\pi + \theta_R)$$

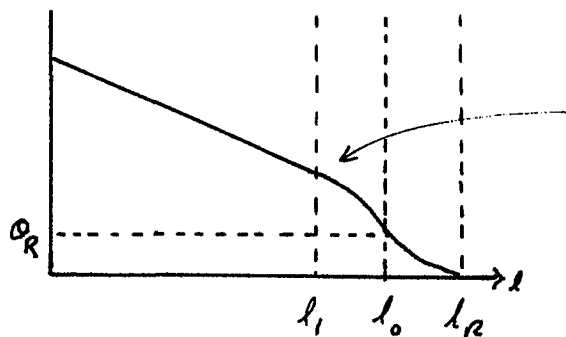


for $l < l_1$

$$a_2(l) = 1$$

for $l \geq l_1$

$$a_2(l) = \frac{1}{2} [1 + \cos[\omega(l - l_R) + \pi]]$$



$$a_1(l) \cdot a_2(l)$$

Both Case I and Case II will fail if $l_1 < 0$. The computer program will return a fail message. In this program the input values are $N, R, I, l_0, h_1,$ and h_2 . These are external parameters supplied initially from semiclassical estimates. The latter three apply directly to the analytic function necessary to determine the repulsive branch of the classical deflection function. Other values ($\mathbb{H}_p(l), \mathbb{Q}_R$) needed in the determination of the repulsive function are calculated by the computer program.

In order to demonstrate how well the analytic function works, two deflection functions are shown for comparison in Figure 30. Curve A shows a deflection function in which h_1 and h_2 have been chosen to be $\pi/4$ and $\pi/2$ respectively. This should generate a "straight" line for $\mathbb{H}_{\text{total}}$ from l_0 to π . In curve B the values of $h_1, h_2,$ and l_0 are increased slightly in order to show a deflection function with more curve in its repulsive branch. $\text{Im}\lambda_p$ has also been increased to better show how smoothly the sum $\mathbb{H}_p(l)$ and $\mathbb{H}_{\text{core}}(l)$ come together around l_R (i.e. using $\mathbb{Q}_R \approx 2N/I$ to vary the depth of the deflection function). Curve B will generate (via the inversion method) a potential in which the repulsive branch is sharper (i.e. greater negative slope) than will curve A.

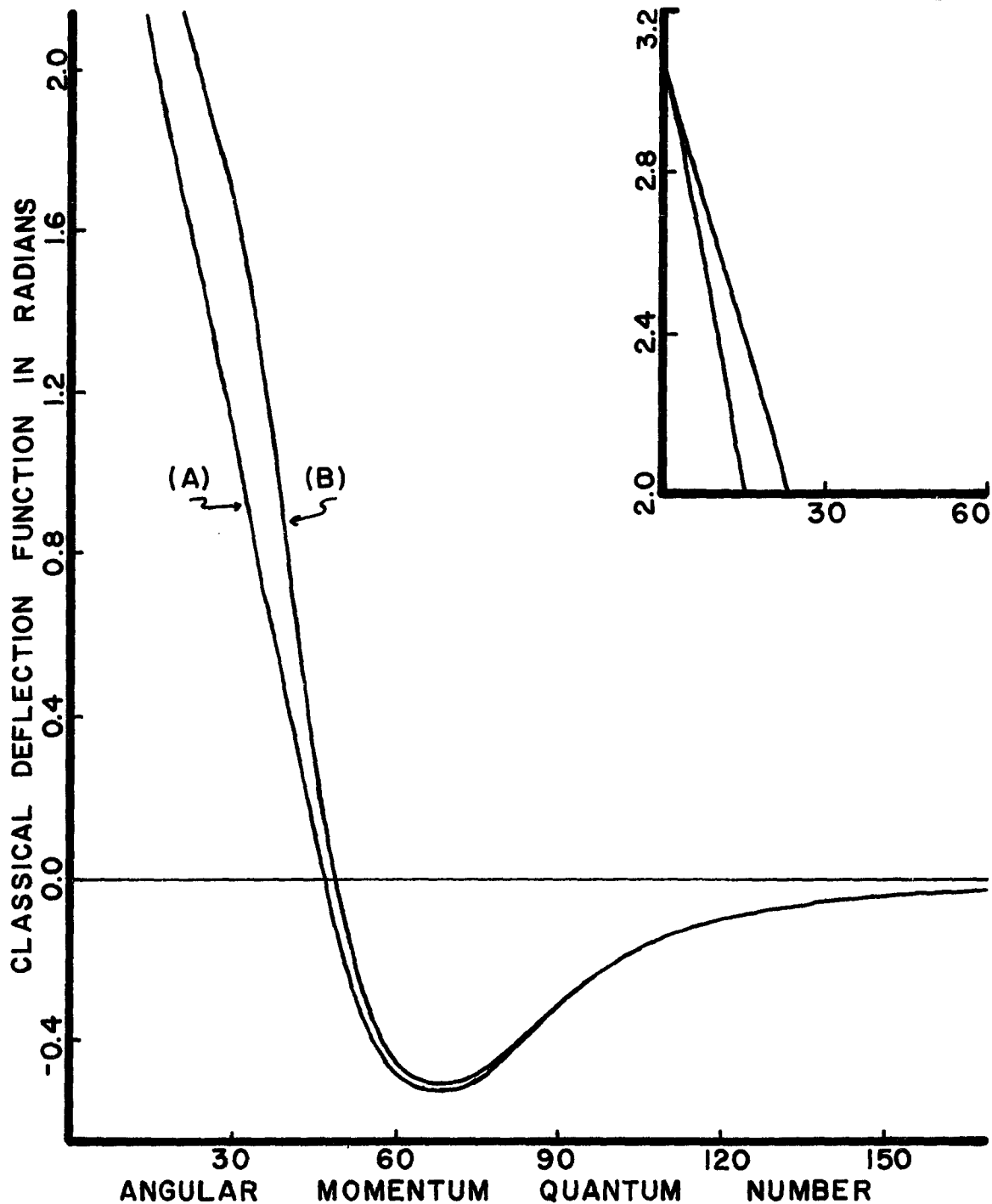


Figure 30. Classical deflection function. Illustration of the flexibility in the repulsive branch of the classical deflection function. The parameter values of curves A and B respectively are : $l_0 = 48.0, 50.0$; $h_1 = \pi/4$ (.785), 1.2; $h_2 = \pi/2$ (1.57); $I = 25.8, 26.5$; $N = 7, 7$; $R = 70.0, 70.0$.

REFERENCES

1. For example: Amdur, I. and Harkenss, A. L., J. Chem. Phys. 22, 664 (1954). Amdur, I. and Mason, E. A., J. Chem. Phys. 22, 670 (1954); 23, 415 (1955); 23, 2268 (1955); 25, 624 (1956); 25, 630 (1956); etc.
2. Ford, K. W. and Wheeler, J. A., Ann. Phys. 7, 259 (1959).
3. Lane, G. H. and Everhart, E., Phys. Rev. 117, 920 (1960); Phys. Rev. 120 2064 (1960).
4. Bernstein, R. B., Advances in Chemical Physics, Vol. X, edited by John Ross (Interscience, New York, 1966) pt. 75.
5. For example: Champion, R. L., Doverspike, L. D., Rich, W. G., and Bobbio, S. M., Phys. Rev. A 2, 2327 (1970). Mittmann, H. U., Weise, H. P., Ding, A., and Henglein, A., Zeitschrift Fur Naturforschung, 26a, 1112 (1971).
6. Rich, W. G., Bobbio, S. M., Champion, R. L., and Doverspike, L. D., Phys. Rev. A 4, 2253 (1971).
7. Remler, E. A., Phys. Rev. A 3, 1949 (1971).
8. Marchi, R. P. and Smith, F. T., Phys. Rev. A 139, 1025 (1965).
9. Lorents, D. C. and Aberth, W., Phys. Rev. A 139, 1017 (1965).
10. Gupta, B. K. and Matsen, R. A., J. Chem. Phys. 47, 4860 (1967).
11. Olson, R. E. and Mueller, C. R., J. Chem. Phys. 46, 3810 (1967).
12. Phillipson, P. E., Phys. Rev. 125, 1981 (1962).

13. Aberth, W. and Peterson, J. R., Rev. Sci. Instr. 38, 745 (June 1967).
14. Spangenberg, K. R., Vacuum Tubes, (McGraw-Hill Book Company, New York 1948) pg. 328.
15. Hintenberger, H., Rev. Sci. Instr. 20, 855 (1949).
16. Marnet, P., and Kerwin, L., Can. J. Phys. 38, 787 (1960).
17. Paul, W., Reinhard, H. P., and von Zahn, U., Z. Phys. 152, 143 (1958).
18. Landes, H. S., "The Analysis of Ion Beams Using an R. F. Mass Spectrometer", University of Virginia Report No. EP-2894-106-60U (1960).
19. Champion, R. L., Thesis, "Collision-Induced Dissociation of D_2^+ Ions by Argon and Nitrogen", (University of Florida 1966), pg. 22.
20. Mott, N. R. and Massey, H. S. W., The Theory of Atomic Collisions, (Oxford U. P., Oxford, England, 1965), pg. 99.
21. Reference 14, pg. 24.
22. Berry, M. V., Proc. Phys. Soc. (London) 89, 479 (1966).
23. Miller, W. H., J. Chem. Phys. 48, 464 (1968).
24. Firsov, O. B., Zh. Eksp. Teor. Fiz. 24, 279 (1953). Vollmer, G., Z. Physik 226, 423 (1969). Vollmer, G. and Kruger, H., Phys. Letters A 28, 165 (1968). Miller, W. H., J. Chem. Phys. 51, 3631 (1969).
25. Regge, T., Nuovo Cimento 14, 951 (1959).
26. Marchi, R. P. and Mueller, C. R., J. Chem. Phys. 38, 740 (1963).
27. Mittmann, H. U., Weise, H. P., Ding, A., and Henglein, A., Zeitschrift Fur Naturforschung, 26a, 1112 (1971).

28. Wolniewicz, L., J. Chem. Phys. 43, 1087 (1965).
29. Helbig, H. R., Millis, D. B., and Todd, L. W., Phys. Rev. A 2, 771 (1970).
30. Peyerimhoff, S., J. Chem. Phys. 43, 998 (1965).
31. Reagan, P. M., Browne, J. C., and Matsen, F. A., Phys. Rev. 132, 304 (1963).
32. Weise, H. P., Mittmann, H. U., Ding, A., and Henglein, A., Zeitschrift Fur Naturforschung, 26a, 1122 (1971).
33. Mott, M. R., Proc. Roy. Soc. A, 126, 259 (1930).
34. Massey, H. S. W. and Smith, R. A., Proc. Roy. Soc. A 142 (1933).
35. Reference 20, pg. 646.
36. Aberth, W., Lorents, D. C., Marchi, R. P., and Smith, R. T., Phys. Rev. Letters 14, 776 (1965).
37. Gilbert, T. L. and Wahl, A. C., J. Chem. Phys. 55, 5247 (1971).
38. Liu. B., Phys. Rev. Letters, 27, 1251 (1971).
39. Squires, E. J., Complex Angular Momenta and Particle Physics, (W. A. Benjamin Inc., N. Y., 1963) pg. 4.

VITA

William Guy Rich was born in Tar Heel, North Carolina, on February 12, 1939. In June, 1957, he was graduated from Laurinburg High School, Laurinburg, North Carolina, and in September of the same year he entered Catawba College, Salisbury, North Carolina. In June, 1961, he received a Bachelor of Arts Degree with majors in mathematics and physics. In September, 1961, he began graduate study at Wake Forest College and was graduated in August, 1963, with a Master of Arts Degree with a major in physics. From September, 1963, to June, 1966, he was Assistant Professor of Physics at Elon College, Elon College, North Carolina. In September, 1966, he entered the Graduate School of the College of William and Mary. His undergraduate and graduate studies have been supported by the Adrain L. Shuford Scholarship, graduate fellowships, teaching assistantship, NASA Traineeship, and research assistantships. During the summers of 1964 and 1965 he was a participant in the NSF Summer Institute for College Teachers of Science.

William Guy Rich is married to the former Linda Burgess.